ASSESSING THE ROLE OF BIOMECHANICAL FLUID–STRUCTURE INTERACTIONS IN CEREBRAL ANEURYSM PROGRESSION VIA PATIENT-SPECIFIC COMPUTATIONAL MODELS

by

Tanmay Chandrashekhar Shidhore

A Dissertation

Submitted to the Faculty of Purdue University

In Partial Fulfillment of the Requirements for the degree of

Doctor of Philosophy

School of Mechanical Engineering

West Lafayette, Indiana

August 2022

THE PURDUE UNIVERSITY GRADUATE SCHOOL
STATEMENT OF COMMITTEE APPROVAL

Dr. Ivan C. Christov, Co-chair

School of Mechanical Engineering

Dr. Vitaliy L. Rayz, Co-chair

Weldon School of Biomedical Engineering

Dr. Craig J. Goergen

Weldon School of Biomedical Engineering

Dr. Carlo Scalo

School of Mechanical Engineering

Dr. Ganesh Subbarayan-Shastri

School of Mechanical Engineering

Approved by:

Dr. Nicole L. Key

To my beloved wife, Atmaja.

ACKNOWLEDGMENTS

I would first like to express my sincere gratitude to both of my advisors, Dr. Ivan C. Christov and Dr. Vitaliy L. Rayz for their constant support of my doctoral research, for their patience and motivation. Their guidance during my research and at the time of writing my thesis has been immensely invaluable. More importantly, they have helped me grow not only a researcher but also as an individual.

I would like to thank my committee members Dr. Craig Goergen, Dr. Ganesh Subbarayan-Shastri and Dr. Carlo Scalo for their insightful suggestions and hard questions.

It has been a pleasure to work with wonderful lab-mates at the TMNT and CFM labs. To my colleagues, Sean Rothenberger, Joseph Muskat, Tyler Diorio, Wonseok Heo, Dr. Kimberly Stevens-Boster, Xiaojia Wang, Zongxin Yu, Dr. Daihui Lu, Dr. Federico Municchi and Dr. Vishal Anand, thank you for all the wonderful and stimulating discussions. I would also like to express my gratitude to Dr. Aaron Cohen-Gadol at the Indiana University School of Medicine and Dr. Hannah Cebull.

I would also like to acknowledge the Kati Lorge Chair of Research of the Brain Aneurysm Foundation for their support of the work done in this thesis, in particular Specific Aim 3. Chapter 3 of this work is under review as a paper in the *Engineering with Computers*, and I wish to thank the special issue's associate editor, Prof. Adrian Buganza-Tepole (Purdue University, West Lafayette), for the opportunity to contribute.

I would further like to acknowledge the resources of the Extreme Science and Engineering Discovery Environment (XSEDE) and the Texas Advanced Computing Center (TACC), supported by National Science Foundation under grant number ACI-1548562 (providing compute time for my work under project MCH200007), as well as the community clusters at the Rosen Center for Advanced Computing (RCAC) at Purdue University.

Finally, I would like to express my profound gratitude to my wife, Atmaja, my parents, family and friends. They have been a pillar of support through my PhD journey and this work would not have been possible without their love and encouragement.

TABLE OF CONTENTS

LIST OF TABLES

LIST OF FIGURES

ABSTRACT

Three key challenges in developing advanced image-based computational models of cerebral aneurysms are: (i) disentangling the effect of biomechanics and confounding clinical risk factors on aneurysmal progression, (ii) accounting for arterial wall mechanics, and (iii) incorporating the effect of surrounding tissue support on vessel motion and deformation. This thesis addresses these knowledge gaps by developing fluid-structure interaction (FSI) models of subject-specific geometries of cerebral aneurysms to elucidate the effect of coupled hemodynamics and biomechanics. A consistent methodology for obtaining physiologically realistic computational FSI models from standard-of-care imaging data is developed. In this process, a novel technique to estimate heterogeneous arterial wall thickness in the absence of subject-specific arterial wall imaging data is proposed. To address a limitation in the mesh generation workflow of the state-of-the-art cardiovascular flow modeling tool SimVascular, generation of meshes with boundary-layer mesh refinement near the blood-vessel wall interface is proposed for computational geometries with nonuniform wall thickness. Computational murine models of thoracic aortic aneurysms were developed using the proposed methodology. These models were used to inform external tissue support boundary conditions for human cerebral aneurysm subjects via a scaling analysis. Then, the methodology was applied to subjects with multiple unruptured cerebral aneurysms. A comparative computational FSI analysis of aneurysmal biomechanics was performed for each subject-specific pair of computational models for the stable and growing aneurysms, which act as self-controls for confounding clinical risk factors. A higher percentage of area exposed to low shear and high median-peak-systolic arterial wall deformation, each by factors of 1.5 to 2, was observed in growing aneurysms, compared to stable ones. Furthermore, a novel metric – the oscillatory stress index (OStI) – was defined and proposed to indicate locations of oscillating arterial wall stresses. Growing aneurysms demonstrated significant areas with a combination of low wall shear and low OStI, which were hypothesized to be associated with regions of collagen degradation and remodeling. On the other hand, such regions were either absent (or were a small percentage of the total aneurysmal area) in the stable cases. This thesis, therefore,

provides a groundwork for future studies, with larger patient cohorts, which will evaluate the role of these biomechanical parameters in cerebral aneurysm growth.

1. INTRODUCTION

Cerebral or intracranial aneurysms are dilations in the walls of cerebral arteries, most commonly occurring in or near the Circle of Willis. Cerebral aneurysms are estimated to occur in 5-8% of the population [1]. Aneurysm rupture results in subarachnoid hemorrhage and accounts for 3-5% of strokes with a 50% mortality rate [2]. However, risk of rupture of an aneurysm is poorly understood and clinicians are often faced with difficult decisions regarding invasive treatments, which can involve potential morbidity and mortality risks. The overarching goal of this thesis is to improve understanding of biomechanical factors affecting cerebral aneurysm growth and rupture through realistic subject-specific computational models, which can be eventually translated to risk stratification of cerebral aneurysms. Specifically, by using standard-of-care medical imaging data to develop high-resolution computational models, new understanding of the interaction of hemodynamics and biomechanics in aneurysms can be established. To this end, the following specific aims are proposed, each of which is addressed in a separate chapter.

1.1 Specific Aim 1 (SA1): Develop a Computational Fluid–Structure Interaction (FSI) Framework

A new computational strategy to analyze FSIs in cerebral aneurysms is developed, using the open-source cardiovascular flow modeling framework SimVascular [3], [4]. Key steps developed as part of this novel process are:

1. Extracting the flow domain from 4DUS (four-dimensional ultrasound) measurements or CT (computed tomography), MRI (magnetic resonance imaging), X-ray angiography data.

2. Estimating nonuniform thickness of the arterial wall, in the absence of subject-specific imaging data, by accounting for local wall thickening/thinning effect of wall shear stress on the diseased region.

3. Generating conformal fluid and structural meshes with boundary layer mesh refinement in the flow domain using a novel workflow to overcome the limitations of SimVascular's current meshing methodology.

4. Determining arterial pre-stress for the geometrical configuration segmented from imaging data.

5. Modeling the effect of the surrounding tissue support through calibrated viscoelastic external tissue support (spring-dashpot) boundary conditions that constrain displacements.

Outcome: Achieving this specific aim yielded a consistent modeling methodology for performing the physiologically realistic subject/animal specific FSI simulations that are part of the subsequent specific aims. Important gaps in the SimVascular's FSI modeling workflow were addressed, specifically with respect to obtaining vessel wall geometries with user-defined wall thickness and incorporating boundary-layer mesh refinement near the fluid-solid interface in geometries with nonuniform wall thickness. This outcome enabled accurate estimation of wall shear stress.

1.2 Specific Aim 2 (SA2): Optimize External Tissue Support Parameter Characterization of AngII Infused Mouse Models Of Thoracic Aortic Aneurysms

Four-dimensional ultrasound (4DUS) measurements of four mice at baseline and 28 days following AngII infusion (obtained from collaborators at Cardiovascular Imaging Research Laboratory (CVIRL) at Purdue University) were used to develop a computational FSI model of the motion of ascending aorta in an idealized healthy and diseased mouse, using the methodology developed under SA1 (see Section 1.1). External tissue support parameters were then calibrated using these FSI simulations, such that wall displacement data obtained from simulations matched *in vivo* displacements obtained from 4DUS imaging.

Outcome: A novel methodology of obtaining tissue support parameters for murine models of thoracic aortic aneurysms (TAAs) using *in-vivo* four-dimensional ultrasound (4DUS) data was developed. Calibrated values of tissue support parameters were obtained for idealized

healthy and diseased animal models for use in future studies. Furthermore, tissue support parameter values from these animal models were used to inform corresponding values for human subjects, in the subsequent specific aim, using appropriately developed scaling laws.

1.3 Specific Aim 3 (SA3): Comparative Biomechanical Analysis of Subjects With Multiple Cerebral Aneurysms.

Retrospective longitudinal imaging data on two subjects (each with multiple unruptured cerebral aneurysms) obtained from clinical collaborators at Indiana University School of Medicine (IUSM) was used. In each subject, growth was observed in one of the aneurysms while the other one remains stable between baseline and follow-up imaging. Using the methodology from SA1 (see Section 1.1) and appropriately scaled tissue support parameters from SA2 (see Section 1.2), a computational FSI model was generated for each of the subject-specific geometries. Biomechanical parameters, such as wall shear stress, oscillatory shear index, wall deformation, and the orientation of principal arterial wall stress were compared between the two aneurysms, which can act as self-controls for clinical risk factors affecting aneurysm progression.

Outcome: Comparison of biomechanical factors for stable and growing aneurysms in the same subject revealed the influence of the local flow and wall mechanics on aneurysm growth. Specifically, quantitative differences were observed in the proportion of area exposed to low wall shear stress, the magnitude of peak systolic wall deformation, and proportion of combined regions of low shear and significant oscillating arterial wall stresses.

2. SPECIFIC AIM 1: COMPUTATIONAL FSI FRAMEWORK

This chapter describes the research methodology used to achieve specific aim 1, which is a prerequisite for achieving the remaining specific aims introduced in Chapter 1. Figure 2.1 shows a schematic of the steps implemented to obtain physiologically realistic FSI models of cerebral aneurysms from subject-specific imaging data. The details of each step are presented below.

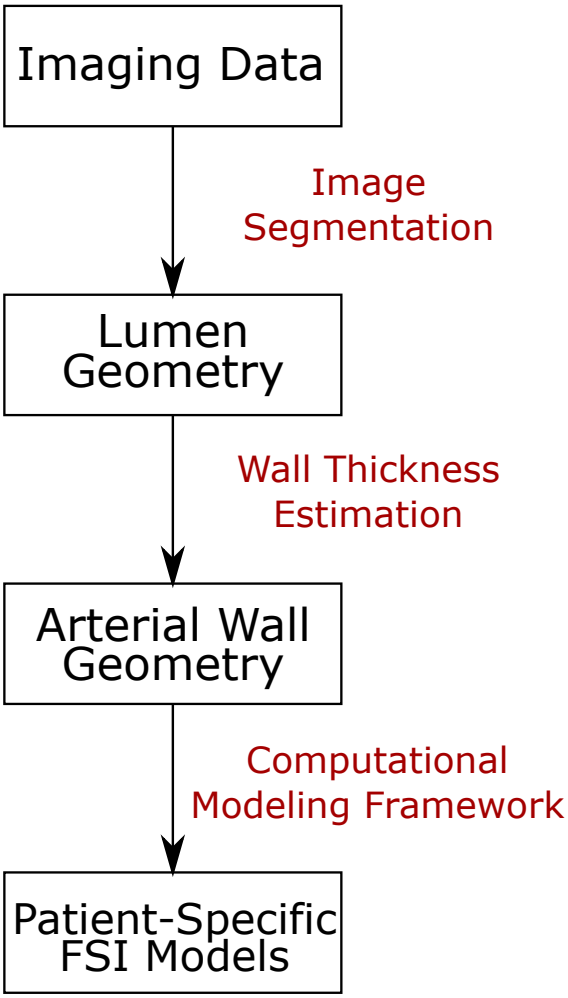

Figure 2.1. Schematic of the computational model development workflow: From medical imaging data to FSI simulations.

2.1 Image Segmentation

Subject or animal data is available in the form of MR, CT, X-ray angiography and/or 4D US images. As an example of each, Figure 2.2 shows an image slice from CT, MR images of different human subjects with a cerebral aneurysm and 4D US image slice of a healthy mouse aorta. The first step in creating a computational geometry is extracting the region of interest (typically the aneurysm and portions of upstream and downstream vessels) from medical imaging data using 3D image segmentation techniques. In the present analysis, the open-source 3D medical image segmentation tool ITK-SNAP [5] is used. ITK-SNAP allows segmentation using manual methods as well as the automatic active contour (snakes) model implemented using a level set method for extracting volume of interest. Subsequently, the bounding surface of the extracted volume can be exported in the stereolithographic (.stl) format. The STL model is then manually smoothed using the commercial computer-aided design (CAD) software Geomagic® Design X to eliminate any segmentation artifacts such as sharp edges and bumps and the final 3D geometric model of the flow domain of the aneurysm and its proximal and distal arteries is generated.

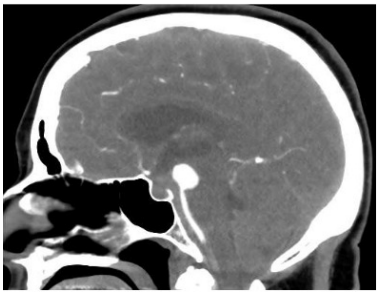

(a) CT image slice of an aneurysm of the basilar artery (obtained from IUSM)

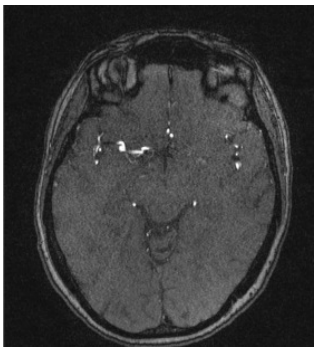

(b) MR image slice of an aneurysm of the right middle cerebral artery (obtained from IUSM)

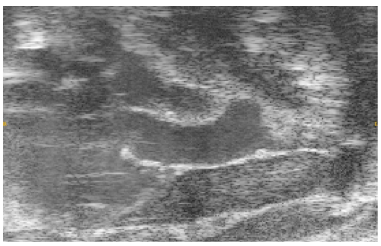

(c) 4D US image slice of a portion of the murine ascending aorta (obtained from CVIR Lab)

Figure 2.2. Examples of clinical imaging modalities and the types of data they generate.

2.2 Estimating Arterial Wall Thickness

For any FSI analysis, information on the wall thickness, either in the form of ex-vivo histology data from resected aneurysm samples or image data is essential for generating subject-specific geometries of the arterial wall. However, as seen from Figure 2.2 in-vivo imaging data may not necessarily possess information on the vessel wall and obtaining histology samples may not be feasible. Therefore, a methodology to obtain physiologically realistic estimates of the vessel wall thickness from angiographic data of the lumen (inner arterial wall) is essential. Most prior studies have not accounted for FSI or assumed a uniform wall thickness over the region of interest, based on population averaged estimates [6], [7], specifically due to the lack of such data. However, the assumption of constant wall thickness does not account for the nonuniformity wall thickness due to natural tapering of arterial vessels, which is found to be of importance while performing FSI simulations [8]. Some studies (e.g., [9] and the references therein) estimated a nonuniform wall thickness for their subject-specific FSI models by solving the Laplace equation on the surface of the lumen. Empirical thickness value estimates, corresponding to 10% of the average diameter at the inlet and outlet sections were used as boundary conditions. However, these studies did not account for the effect of hemodynamics on vessel wall thickness, especially over the diseased region. As shown in [7], [10], regions of abnormally elevated or reduced wall shear stresses in aneurysms have demonstrated differences in local wall thicknesses. Regions of low WSS have a tendency to produce stagnation zones, which can cause atherosclerotic deposition whereas high WSS may result in activation of inflammatory pathways leading to compromised strength of smooth muscle cells (SMC), SMC degeneration and loss [11].

In the subsequent specific aims, a methodology to estimate the heterogenous vessel wall thickness has been implemented for each analysis. This methodology is implemented using the SimVascular framework, an in-house code developed in python, the open-source visualization tool Paraview [12], the open source mesh processing software MeshLab [13] and the commercial computer-aided design (CAD) software Geomagic® Design X. The end result is a solid geometry of the arterial vessel wall with nonuniform vessel wall thickness, accounting for the effect of hemodynamic forces on vessel wall thickness. Exact details on the imple-

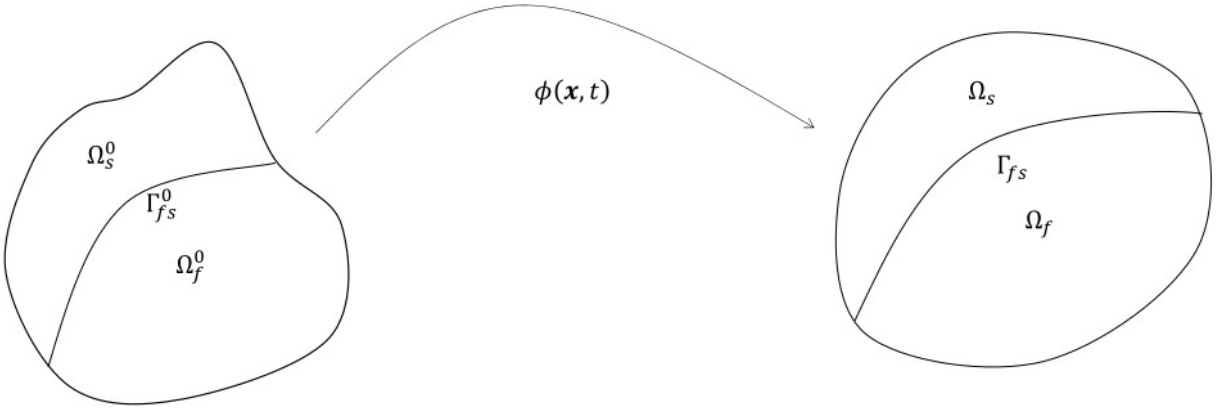

Figure 2.3. Abstract schematic showing the reference and current configurations of the deformable body under the mapping $\phi(\mathbf{x}, t)$, along with the notation used in the main text.

mentation of this methodology vary based on the computational model (human or animal) being considered and are therefore deferred to subsequent chapters in the thesis. It is emphasized that this approximation is not the actual wall thickness in the subject or animal. This methodology enables the estimation of a realistic nonuniform wall thickness based on local hemodynamic characteristics, that lies within range of literature-reported values, in the absence of any subject-specific data.

2.3 Computational Modeling Framework

The open-source cardiovascular modeling tool SimVascular [3], [4], in particular the FSI solver, svFSI [14], is used to perform the rigid-wall pulsatile flow simulations for estimating wall thickness and the FSI simulations. The key mathematical details of the framework are presented below. Further details on numerical schemes and implementation may be found in [15]–[17].

Consider a representative abstract configuration for a generic FSI problem (as shown in Figure 2.3). Here, Ω_f^0 and Ω_s^0 are the reference fluid and solid configurations, with the fluid-solid interface Γ_{fs}^0. They are related to the current fluid, solid configurations and fluid-solid interface Ω_f, Ω_s and Γ_{fs} respectively through an ALE mapping $\phi(\mathbf{x}, t)$.

2.3.1 Solid Mechanics Problem

A Lagrangian description is used to formulate the structural problem over the reference solid domain Ω_s^0 and its weak form may be written as:

Find $\mathbf{u} \in \mathcal{V}^s$ such that $\forall\ \mathbf{W} \in \mathcal{W}^s$,

$$\int_{\Omega_s^0} \left[\rho_s \mathbf{W} \cdot \ddot{\mathbf{u}} + \nabla_{\mathbf{X}} \mathbf{W} : \mathbf{F}\mathbf{S}\right] d\Omega_s^0 - \int_{\Gamma_{s,h}^0} \mathbf{W} \cdot \mathbf{h}\, d\Gamma_s^0 - \int_{\Omega_s^0} \rho_s \mathbf{W} \cdot \mathbf{f}\, d\Omega_s^0 = 0. \tag{2.1}$$

Here, ρ_s, $\ddot{\mathbf{u}}$, $\mathbf{f}$, $\mathbf{F}$, $\mathbf{S}$, $\mathbf{W}$ are the solid density, acceleration, external body force vector, deformation gradient defined between the reference and current configurations, second Piola-Kirchhoff stress tensor and test function respectively. Here, $\nabla_{\mathbf{X}}$ is the spatial derivative with respect to the material (reference configuration) coordinates and $\Gamma_{s,h}^0$ is the region of the solid boundary where natural (Neumann) boundary conditions $\mathbf{h}$ are prescribed. The function spaces are defined as:

$$\mathcal{V}^s = \left\{\mathbf{u} \,|\, \mathbf{u}(\mathbf{x}, t) \in (H^1)^n \times [0, T],\ \mathbf{u} = \bar{\mathbf{u}} \text{ on } \Gamma_{s,g}^0\right\}, \tag{2.2a}$$

$$\mathcal{W}^s = \left\{\mathbf{W} \,|\, \mathbf{W}(\mathbf{x}, t) \in (H^1)^n \times [0, T],\ \mathbf{W} = \mathbf{0} \text{ on } \Gamma_{s,g}^0\right\}, \tag{2.2b}$$

where n is the dimension of the computational domain, $\bar{\mathbf{u}}$ is the imposed Dirichlet boundary condition, and $\Gamma_{s,g}^0$ is the part of the boundary on which Dirichlet boundary conditions are imposed. The second Piola-Kirchhoff stress tensor $\mathbf{S}$ in Equation (2.1) is determined from a hyperelastic constitutive relation proposed in [18] via the strain energy density function:

$$\psi(\mathbf{C}, J) = \frac{1}{2}\mu_s \left(J^{-2/3} \operatorname{tr} \mathbf{C} - 3\right) + \frac{1}{2}\kappa \left[\frac{1}{2}(J^2 - 1) - \ln J\right], \tag{2.3a}$$

$$\mathbf{S} = 2\frac{\partial \psi}{\partial \mathbf{C}} = \mu_s J^{-2/3} \left(\mathbf{I} - \frac{1}{3}(\operatorname{tr} \mathbf{C})\mathbf{C}^{-1}\right) + \frac{1}{2}\kappa \left(J^2 - 1\right) \mathbf{C}^{-1}. \tag{2.3b}$$

Here, ψ is the strain-energy density function, $J = \det \mathbf{F}$ is the Jacobian, and $\mathbf{C} = \mathbf{F}^\top \mathbf{F}$ is the right Cauchy-Green deformation tensor. The material parameters μ_s and κ are the shear

and bulk moduli of the solid, respectively, which can be expressed in terms of the Young's modulus of elasticity E and the Poisson ratio ν as:

$$\mu_s = \frac{E}{2(1+\nu)}, \tag{2.4a}$$

$$\kappa = \frac{E}{3(1-2\nu)}. \tag{2.4b}$$

In the subsequent chapters, the arterial wall has been modeled as a nearly incompressible, isotropic hyperelastic material, by choosing a constant value of E and setting $\nu = 0.49$ [19].

2.3.2 Mesh Motion Problem

In interface-tracking formulations like ALE, the problem of fluid mesh motion needs to be considered in addition to the flow and structural dynamics equations. The automatic mesh motion methodology proposed in [20] is implemented in svFSI. The mesh motion problem during a particular time step is essentially treated as an elastic boundary value problem to produce smooth evolution of the fluid mesh. An assumption is made that the configuration at the beginning of the current time step (end of the previous time step) can be regarded as a "nearby" configuration to the configuration at the end of the current time step, enabling the use of infinitesimal strain theory. The weak formulation (in the absence of any external force and tractions) is

$$\int_{\Omega_f} \Big[\boldsymbol{\epsilon}(\mathbf{w}) : \boldsymbol{\sigma}(\mathbf{u})\Big]\, d\Omega_f = 0. \tag{2.5}$$

Here, $\mathbf{u}$ and $\mathbf{w}$ are the trial displacement and test functions, respectively. Meanwhile, $\boldsymbol{\sigma}(\mathbf{u})$ and $\boldsymbol{\epsilon}(\mathbf{w})$ are the "stress" tensor and the elastic strain measure of the trial and test functions, respectively, defined as

$$\boldsymbol{\sigma}(\mathbf{u}) = \lambda\, \mathrm{tr}(\boldsymbol{\epsilon}(\mathbf{u}))\mathbf{I} + 2\mu\boldsymbol{\epsilon}(\mathbf{u}), \tag{2.6}$$

$$\boldsymbol{\epsilon}(\mathbf{w}) = \frac{1}{2}\Big[\nabla\mathbf{w} + (\nabla\mathbf{w})^T\Big], \tag{2.7}$$

where $\mathrm{tr}(\,\cdot\,)$ is the trace of a tensor, $\mathbf{I}$ is the identity, and λ_m and μ_m are the Lamé elastic constants of the fictitious "material" used to represent the mesh. The function spaces for the trial and test functions are:

$$\mathcal{V}^m = \Big\{ \mathbf{u} \,|\, \mathbf{u} \in (H^1)^n,\ \mathbf{u} = \bar{\mathbf{g}} \text{ on } \Gamma_{f,g} \Big\}, \tag{2.8a}$$

$$\mathcal{W}^f = \Big\{ \mathbf{w} \,|\, \mathbf{w} \in (H^1)^n,\ \mathbf{w} = \mathbf{0} \text{ on } \Gamma_{f,g} \Big\}, \tag{2.8b}$$

where $\Gamma_{f,g}$ is the part of the boundary where Dirichlet boundary conditions are imposed and $\bar{\mathbf{g}}$ is the Dirichlet boundary value.

Equation (2.5) can be solved on the fluid domain by imposing the displacement of the fluid-solid interface (obtained from the structural elastodynamics equations) and the motion of any other boundary that is prescribed independently, as a Dirichlet boundary condition. As mentioned in Johnson *et al.* [20], in the absence of external forces and tractions, the problem may be reduced to specifying a single parameter $\lambda_\mathrm{m}/\mu_\mathrm{m} = 2\nu_\mathrm{m}/(1-2\nu_\mathrm{m})$, where ν_m is the Poisson ratio of the fictitious "material" used to represent the mesh. In practice, the value $\nu_\mathrm{m} = 0.3$ is used [15].

2.3.3 Fluid Flow Problem

The fluid flow problem in an ALE formulation, as implemented in svFSI is described in this subsection. For a Newtonian fluid and incompressible flow, the Galerkin weak form of the Navier-Stokes equation over the flow domain Ω_f can be written. The variational problem to be solved is:
Find $\mathbf{v} \in \mathcal{S}^f$ and $p \in \mathcal{P}^f$, such that $\forall\ \mathbf{w} \in \mathcal{W}^f$ and $q \in \mathcal{Q}^f$:

$$\int_{\Omega_f} \Big[\rho_f \mathbf{w} \cdot (\dot{\mathbf{v}} + (\mathbf{v} - \hat{\mathbf{v}}) \cdot \nabla_{\mathbf{x}} \mathbf{v}) + \nabla \mathbf{w} : (-p\mathbf{I} + 2\mu_f \nabla^s_{\mathbf{x}} \mathbf{v}) \Big]\, d\Omega_f \\ - \int_{\Gamma_{f,h}} \mathbf{w} \cdot \mathbf{h}\, d\Gamma_f + \int_{\Omega_f} q \nabla \cdot \mathbf{v}\, d\Omega_f - \int_{\Omega_f} \rho_f \mathbf{w} \cdot \mathbf{f}\, d\Omega_f = 0. \tag{2.9}$$

Here, ρ_f, $\hat{\mathbf{v}}$, $\dot{\mathbf{v}}$, p, $\mathbf{f}$, μ_f, $\mathbf{w}$, q are the fluid density, grid velocity of the fluid domain, acceleration, pressure, body force, viscosity, and the velocity and pressure test functions, respectively.

$\nabla^s_{\mathbf{x}}\mathbf{v}$ is the symmetric part of the velocity gradient. $\Gamma_{f,h}$ is the part of the boundary where the natural (Neumann) boundary conditions $\mathbf{h}$ are prescribed. The function spaces are defined as:

$$\mathcal{S}^f = \Big\{\mathbf{v} \,|\, \mathbf{v}(\mathbf{x},t) \in (H^1)^n \times [0,T],\, \mathbf{v} = \bar{\mathbf{v}} \text{ on } \Gamma_{f,g}\Big\}, \tag{2.10a}$$

$$\mathcal{W}^f = \Big\{\mathbf{w} \,|\, \mathbf{w}(\mathbf{x},t) \in (H^1)^n \times [0,T],\, \mathbf{w} = \mathbf{0} \text{ on } \Gamma_{f,g}\Big\}, \tag{2.10b}$$

$$\mathcal{P}^f = \mathcal{Q}^f = \Big\{q \,|\, q(\mathbf{x}) \in L^2\Big\}, \tag{2.10c}$$

where n is the dimension of the computational domain, $\bar{\mathbf{v}}$ is the imposed Dirichlet boundary, and $\Gamma_{f,g}$ is the part of the boundary where Dirichlet boundary conditions are imposed. The use of equal order interpolation functions for pressure and velocity results in instabilities in advection-dominated flows, and this limitation arises due to inability to satisfy the Ladyzhenskaya-Babuška-Brezzi condition [21]. The RBVMS method (residual-based variational multiscale method) [22] is therefore used to overcome this limitation.

The RBVMS adds stabilization terms to the Galerkin weak form (2.9). The infinite dimensional function spaces $\mathcal{S}^f, \mathcal{P}^f, \mathcal{W}^f$ and $\mathcal{Q}^f$ are decomposed into a finite dimensional and infinite dimensional function space representing the coarse scales resolved by the finite element discretization and the subgrid scales respectively as:

$$\mathcal{S}^f = \mathcal{S}^f_h \bigoplus \mathcal{S}^f_s, \tag{2.11a}$$

$$\mathcal{P}^f = \mathcal{P}^f_h \bigoplus \mathcal{P}^f_s, \tag{2.11b}$$

$$\mathcal{W}^f = \mathcal{W}^f_h \bigoplus \mathcal{W}^f_s, \tag{2.11c}$$

$$\mathcal{Q}^f = \mathcal{Q}^f_h \bigoplus \mathcal{Q}^f_s. \tag{2.11d}$$

The subscripts h and s represent the coarse grid and subgrid spaces respectively. Therefore, each element of these respective sets may be written as:

$$\mathbf{v} = \mathbf{v}_h + \mathbf{v}_s, \tag{2.12a}$$

$$p = p_h + p_s, \tag{2.12b}$$

$$\mathbf{w} = \mathbf{w}_h + \mathbf{w}_s, \tag{2.12c}$$

$$q = q_h + q_s. \tag{2.12d}$$

It should be noted that the subgrid functions, though nonzero within an element, vanish on the element boundaries by definition [23]. Equations (2.12d) is substituted in Equation (2.9), to give:

$$\begin{aligned}\int_{\Omega_f} \Big[\rho_f(\mathbf{w}_h + \mathbf{w}_s) \cdot (\dot{\mathbf{v}}_h + \dot{\mathbf{v}}_s + ((\mathbf{v}_h - \hat{\mathbf{v}}_h) - (\mathbf{v}_s - \hat{\mathbf{v}}_s)) \cdot \nabla_{\mathbf{x}}(\mathbf{v}_h + \mathbf{v}_s)) + \\ \nabla(\mathbf{w}_h + \mathbf{w}_s) : (-(p_h + p_s)\mathbf{I} + 2\mu_f \nabla^s_{\mathbf{x}}(\mathbf{v}_h + \mathbf{v}_s))\Big] \, d\Omega_f \\ - \int_{\Gamma_{f,h}} (\mathbf{w}_h + \mathbf{w}_s) \cdot \mathbf{h} \, d\Gamma_f + \int_{\Omega_f} q \nabla \cdot (\mathbf{v}_h + \mathbf{v}_s) \, d\Omega_f - \int_{\Omega_f} \rho_f (\mathbf{w}_h + \mathbf{w}_s) \cdot \mathbf{f} \, d\Omega_f = 0.\end{aligned} \tag{2.13}$$

The function spaces for the coarse and fine scales are linearly independent [23]. Hence, Equation (2.13) can be divided into two separate problems involving the coarse scale $(q_h, \mathbf{w}_h)$ and fine scale $(q_s, \mathbf{w}_s)$ test function pairs. Following the work of Bazilevs *et al.* [22], the fine scale trial functions are modeled as:

$$\mathbf{v}_s = -\tau \left\{ \left[\frac{\partial \mathbf{v}_h}{\partial t} + \mathbf{v}_h \cdot \nabla \mathbf{v}_h - \mathbf{f}_h \right] - p_h \mathbf{I} + 2\mu_f \nabla^s_{\mathbf{x}} \mathbf{v}_h \right\} = -\tau \mathbf{r}_{\text{mom}}(\mathbf{v}_h, p_h), \tag{2.14}$$

$$p_s = -\rho_f \nu_{\text{IC}} \nabla \cdot \mathbf{v}_h = -\rho_f \nu_{\text{IC}} r_{\text{con}}(\mathbf{v}_h). \tag{2.15}$$

Here, r_{con} and $\mathbf{r}_{\text{mom}}(\mathbf{v}_h, p_h)$ are the residuals of the continuity and momentum equation respectively. The stabilization parameters τ and ν_{IC} are defined as:

$$\tau = \left[\frac{4}{\Delta t^2} + \mathbf{v}_h \cdot \mathbf{G} \mathbf{v}_h + C_I \nu_f^2 \, \mathbf{G} : \mathbf{G} \right]^{-1/2}, \tag{2.16}$$

$$\nu_{\text{IC}} = \frac{1}{\tau \, \text{tr} \, \mathbf{G}}, \tag{2.17}$$

where $\nu_f = \mu_f / \rho_f$ is the kinematic viscosity of the fluid, C_I is a constant dependent on the topology of the finite elements, and the order of the basis function polynomials, $\mathbf{G}$ is the metric tensor of the element isoparametric map, i.e. $\mathbf{G}_{ij} = \sum_{k=1}^{n} \frac{\partial \xi_k}{\partial x_i} \frac{\partial \xi_k}{\partial x_j}$ with n being the number of spatial dimensions of the problem. Substituting for the fine scale functions, using

the fact that $\partial \mathbf{v}_s/\partial t = \mathbf{0}$ and integration by parts to switch derivatives from $\mathbf{v}$ to $\mathbf{w}$, the following can be obtained:

$$\begin{aligned}
\int_{\Omega_f} \Big[\rho_f \mathbf{w}_h \cdot (\dot{\mathbf{v}}_h + (\mathbf{v}_h - \hat{\mathbf{v}}_h) \cdot \nabla_{\mathbf{x}} \mathbf{v}_h) + \nabla \mathbf{w} : (-p_h \mathbf{I} + 2\mu_f \nabla^s_{\mathbf{x}} \mathbf{v}_h)\Big]\, d\Omega_f \\
- \int_{\Gamma_{f,h}} \mathbf{w}_h \cdot \mathbf{h}_h \, d\Gamma_f + \int_{\Omega_f} q_h \nabla \cdot \mathbf{v}_h \, d\Omega_f - \int_{\Omega_f} \rho_f \mathbf{w}_h \cdot \mathbf{f}_h \, d\Omega_f \\
+ \sum_{n=1}^{n_{\text{el}}} \int_{\Omega_{f,e}} \tau \Big[(\mathbf{v}_h - \hat{\mathbf{v}}_h) \cdot \nabla_{\mathbf{x}} \mathbf{w}_h + \frac{1}{\rho_f} \nabla q_h \cdot \mathbf{r}_{\text{mom}}(\mathbf{v}_h, p_h) d\Omega_f \\
+ \sum_{n=1}^{n_{\text{el}}} \int_{\Omega_{f,e}} \rho_f \nu_{\text{IC}} \nabla_{\mathbf{x}} \mathbf{w}_h \cdot \mathbf{w}_h r_{con}(\mathbf{v}_h) d\Omega_f \\
- \sum_{n=1}^{n_{\text{el}}} \int_{\Omega_{f,e}} \tau \mathbf{w}_h \cdot \Big(\mathbf{r}_{\text{mom}}(\mathbf{v}_h, p_h) \cdot \nabla_{\mathbf{x}} \mathbf{v}_h\Big) d\Omega_f \Big] \\
- \sum_{n=1}^{n_{\text{el}}} \int_{\Omega_{f,e}} \frac{1}{\rho_f} \nabla_{\mathbf{x}} \mathbf{w}_h : \Big(\tau \mathbf{r}_{\text{mom}}(\mathbf{v}_h, p_h)\Big) \otimes \Big(\tau \mathbf{r}_{\text{mom}}(\mathbf{v}_h, p_h)\Big) d\Omega_f = 0. \quad (2.18)
\end{aligned}$$

Here, n_{el} represents the number of elements in the domain. For rigid wall problems, the corresponding formulation is obtained by replacing $\mathbf{v} - \hat{\mathbf{v}}$ by $\mathbf{v}$, i.e., the grid velocity is set to $\mathbf{0}$.

2.3.4 Time Stepping Scheme

The svFSI solver implements the generalized-α algorithm, as proposed by Chung and Hulbert [24]. The mathematical details for the method are presented in this subsection. Details on implementation within svFSI and exact definitions of the element-wise residuals and tangent stiffness matrix terms can be found in [15]. For integration from time step t_n to t_{n+1}, the algorithm works as a multi-stage predictor-corrector. For the fluid equation, the initial value of the nodal velocity, acceleration and pressure at time t_{n+1} at some node a is calculated as:

$$\dot{\mathbf{v}}_{a,n+1} = \frac{\gamma - 1}{\gamma} \dot{\mathbf{v}}_{a,n}, \quad (2.19a)$$

$$\mathbf{v}_{a,n+1} = \mathbf{v}_{a,n}, \quad (2.19b)$$

$$p_{a,n+1} = p_{a,n}. \quad (2.19c)$$

Here, $\gamma = 0.5 + \alpha_m - \alpha_f$, with the values of α_m and α_f being chosen as:

$$\alpha_f = \frac{3 - \rho_\infty}{2 + 2\rho_\infty}, \tag{2.20a}$$

$$\alpha_m = \frac{1}{1 + \rho_\infty}, \tag{2.20b}$$

where $\rho_\infty = 0.2$ [25]. In the next step, acceleration and velocity are calculated at an intermediate time point $n + \alpha_m$ and $n + \alpha_f$ respectively:

$$\dot{\mathbf{v}}_{a,n+\alpha_m} = (1 - \alpha_m)\dot{\mathbf{v}}_{a,n} + \alpha_m \dot{\mathbf{v}}_{a,n+1}, \tag{2.21a}$$

$$\mathbf{v}_{a,n+\alpha_f} = (1 - \alpha_f)\mathbf{v}_{a,n} + \alpha_f \mathbf{v}_{a,n+1}. \tag{2.21b}$$

Subsequently, Newton-Rahpson iterations are performed until the momentum and continuity residuals drop below a pre-specified tolerance value:

$$\mathbf{K}\Delta\mathbf{v} + \mathbf{G}\Delta p = -\mathbf{R}_{\text{mom}}\Big(\dot{\mathbf{v}}_{n+\alpha_m}, \mathbf{v}_{n+\alpha_f}, p_{n+1}\Big), \tag{2.22a}$$

$$\mathbf{D}\Delta\mathbf{v} + \mathbf{L}\Delta p = -\mathbf{R}_{\text{con}}\Big(\mathbf{v}_{n+\alpha_f}, p_{n+1}\Big), \tag{2.22b}$$

where $\mathbf{R}_{\text{mom}}\Big(\dot{\mathbf{v}}_{n+\alpha_m}, \mathbf{v}_{n+\alpha_f}, p_{n+1}\Big)$ and $R_{\text{con}}\Big(\mathbf{v}_{n+\alpha_f}, p_{n+1}\Big)$ are the residuals of the momentum and continuity equation (see Equation (2.15)) for an individual element. Meanwhile, $\Delta\mathbf{v}$ and Δp are the increments in the nodal velocity and pressure, and the tangent stiffness matrices for nodes a and b, defined as:

$$\mathbf{K}_{ab} = \frac{\partial \mathbf{R}_{a,\text{mom}}}{\partial \Delta \mathbf{v}_b}, \tag{2.23a}$$

$$\mathbf{G}_{ab} = \frac{\partial \mathbf{R}_{a,mom}}{\partial \Delta p_b}, \tag{2.23b}$$

$$\mathbf{D}_{ab} = \frac{\partial \mathbf{R}_{a,\text{con}}}{\partial \Delta \mathbf{v}_b}, \tag{2.23c}$$

$$\mathbf{L}_{ab} = \frac{\partial \mathbf{R}_{a,\text{con}}}{\partial \Delta p_b}. \tag{2.23d}$$

Finally, the nodal acceleration, velocity and pressure are subsequently updated as:

$$\dot{\mathbf{v}}_{a,n+\alpha_m} \mathrel{+}= \Delta\mathbf{v}_a, \tag{2.24a}$$

$$\mathbf{v}_{a,n+1} \mathrel{+}= \Gamma\Delta t\Delta\mathbf{v}_a, \tag{2.24b}$$

$$p_{a,n+1} \mathrel{+}= \alpha_f\gamma\Delta t\Delta p_a. \tag{2.24c}$$

For the structural equation, a similar methodology is adopted. The displacement $\mathbf{u}$, the velocity and acceleration $\dot{\mathbf{u}}$ and $\ddot{\mathbf{u}}$ at a node a at time step $n+1$ are initially calculated as:

$$\mathbf{u}_{a,n+1} = \mathbf{u}_{a,n} + \dot{\mathbf{u}}_{a,n+1}\Delta t + \frac{0.5\gamma-\beta}{\gamma-1}\ddot{\mathbf{u}}_{a,n+1}\Delta t^2, \tag{2.25a}$$

$$\dot{\mathbf{u}}_{a,n+1} = \dot{\mathbf{u}}_{a,n}, \tag{2.25b}$$

$$\ddot{\mathbf{u}}_{a,n+1} = \ddot{\mathbf{u}}_{a,n}. \tag{2.25c}$$

Here, $\beta = \gamma^2$, and all the other parameters are as previously defined for the fluid equation. The intermediate displacement at $n+\alpha_f$ is calculated as:

$$\mathbf{u}_{a,n+\alpha_f} = (1-\alpha_f)\mathbf{u}_{a,n} + \alpha_f\mathbf{u}_{a,n+1}. \tag{2.26}$$

Next, Newton-Raphson iterations are conducted:

$$\mathbf{K}_s\Delta\mathbf{u} = -\mathbf{R}_a\Big(\dot{\mathbf{u}}_{n+\alpha_m}, \mathbf{u}_{n+\alpha_f}\Big), \tag{2.27}$$

where $R_a\Big(\dot{\mathbf{u}}_{n+\alpha_m}, \mathbf{u}_{n+\alpha_f}\Big)$ is the residual of the structural (or mesh motion) equations at the given node a. The elements of the tangent matrix $\mathbf{K}_s$ are defined as:

$$(\mathbf{K}_s)_{ab} = \frac{\partial\mathbf{R}_a}{\partial\Delta\mathbf{u}_b}. \tag{2.28}$$

Finally, the updated displacement at t_{n+1} is calculated as:

$$\mathbf{u}_{a,n+1} \mathrel{+}= \beta\Delta t^2\Delta\mathbf{u}_a. \tag{2.29}$$

2.3.5 Flow and Structural Boundary Conditions

Cardiovascular flow and FSI problems typically involve domains with multiple inlets and outlets, depending on the region of vasculature being considered. These problems are also periodic in time, with the time period being equal to the length of a single cardiac cycle (i.e., inverse of the cardiac pulse frequency). For the flow inlets, a periodic pulsatile flow profile, approximated as a Fourier series, is imposed to model the incoming blood flow. Flow rate data is typically obtained either from subject-specific in-vivo measurement (e.g., phase-contrast MRI (PC-MRI), pulsed-wave Doppler (PWD) or 4D flow MRI data) or imposed using population-averaged flow measurements. In order to determine the spatial velocity profile at the inlet, the Womersley number,

$$\mathrm{Wo} = R\sqrt{\frac{2\pi f \rho_f}{\mu_f}}, \tag{2.30}$$

is calculated. Here, R is the inlet vessel radius, f is the cardiac frequency (beats per second), while μ_f and ρ_f are the dynamic viscosity and density of blood, respectively. Spatial velocity profiles corresponding to Womersley number values between 2 and 4 are found to be approximately close to the parabolic (Poiseuille) flow profile.

At the outlets, a time-varying pressure is imposed weakly by using 0D lumped parameter network (LPN) models to mimic the response of the vasculature downstream of the region of interest. The one element (resistance-only) or three element (resistance–capacitance–resistance, or RCR) Windkessel models are the most common choices. More details may be found in [26]. Their electrical analogues are shown in Figure 2.4. In the one element Windkessel model, the outflow pressure $P(t)$ at a given outlet face is specified as:

$$P(t) = P_0 + RQ(t), \tag{2.31}$$

where P_0 is the distal pressure, $Q(t)$ is the time-dependent flow rate through that branch and R is the vascular flow resistance. On the other hand, the three element Windkessel model, which is the model of choice in subsequent specific aims, additionally considers a capacitor

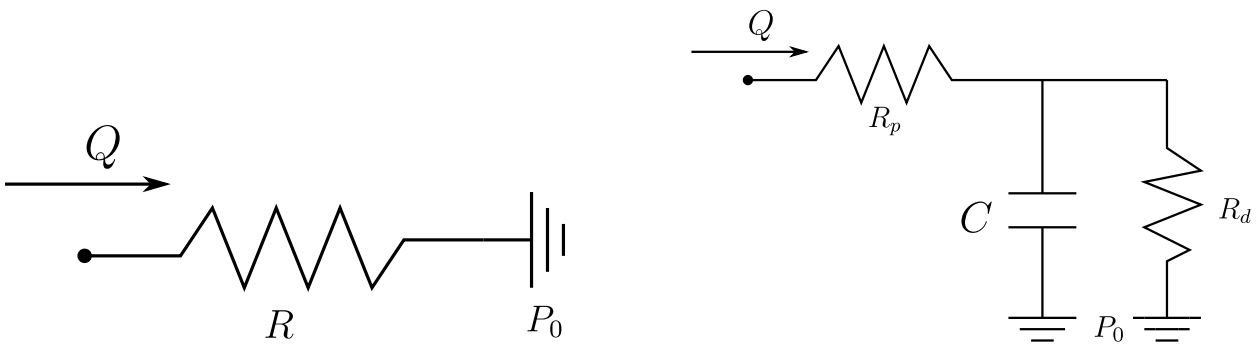

(a) one-element resistance-only model (b) three-element RCR model

Figure 2.4. Electrical analogues of Windkessel models.

element C to model the compliance of the downstream vessels. The flow resistance is also split into the proximal and distal resistance, accounting for the respective (proximal and distal) downstream vessels. Since smaller vessels (arterioles and capillaries) offer larger resistance as compared to proximal mid-sized vessels, the distal resistance R_d value is typically much higher than the proximal resistance R_p, with the ratio R_d/R_p being assumed to be high in most cases. Depending on the specific nature of the computational problem and the available data, there are several ways to estimate these Windkessel parameter values. The subsequent specific aims contain detailed explanation of these methods.

Before discussing the structural boundary conditions, a distinction is made on a broad level on the types of boundaries encountered in cardiovascular FSI simulations. Artificial boundaries are boundaries that arise due to truncation of the computational geometry to isolate the vascular region of interest. The end caps of the solid domain above the inlet and outlet faces are artificial boundaries. Natural boundaries are regions of natural contact between the blood vessel and adjacent bone/tissue. The outer vessel wall, as well as the fluid-solid interface are natural boundaries where the vessel wall is in contact with surrounding tissue/structures and the blood respectively. At the fluid-solid interface, a kinematic and dynamic matching condition is imposed i.e.,

$$\mathbf{v}_{\text{fluid}} = \frac{\partial}{\partial t}\mathbf{u}_{\text{solid}}, \tag{2.32a}$$

$$\boldsymbol{\sigma}_{\text{fluid}} \cdot \mathbf{n}_{\text{fluid}} = -\boldsymbol{\sigma}_{\text{solid}} \cdot \mathbf{n}_{\text{solid}}. \tag{2.32b}$$

For the outer wall, most studies in the past have used a zero traction boundary condition. However, arterial vessels are constrained within biological tissue/fluid and imposing a homogeneous Neumann condition would result in artificial motion patterns of the vessel wall.

Moireau *et al.* [27] and Bäumler *et al.* [28] addressed this problem in their respective studies of the human aorta by imposing a spring-dashpot traction boundary condition on the outer wall:

$$\boldsymbol{\sigma} \cdot \mathbf{n} = -k_s \mathbf{u} - c_s \dot{\mathbf{u}} - p_0. \tag{2.33}$$

This approach models contact at the outer wall akin to support from a Kelvin-Voigt viscoelastic material, characterized by three phenomenological parameters – an elastic spring constant k_s, a viscous damping co-efficient c_s and a constant pressure value p_0, which can be representative of the intracranial/intrathoracic pressure. As explained by Moireau *et al.* [27], these phenomenological values are calibrated by matching wall deformation data from simulations and corresponding data obtained from imaging.

A key feature of this model is that different values can be specified for these phenomenological constants on different regions of the outer wall, depending on the type of contact. In FSI analyses performed in subsequent specific aims, the outer wall is modeled using the viscoelastic tissue support model to account for the effect of surrounding structures. Moreover, modeling studies of healthy and diseased murine aortae reported in Chapter 3 are used inform the choice of tissue support parameters used in Chapter 4.

For the artificial boundary at the end caps, a variety of boundary conditions have been used in previous cardiovascular FSI studies, depending on modeling problem and region of vasculature being considered. Bazilevs *et al.* [29] and others (see references in [9]) used a directional Dirichlet boundary condition (referred to as zero normal displacement boundary condition hereafter) for modeling cerebral aneurysms, where only in-plane deformations were allowed for the artificial boundaries. Most other studies have used a homogeneous Dirichlet boundary condition. This boundary condition is typically used when the pulsatility of vessels is low. Moireau *et al.* [27] proposed relaxing the strong Dirichlet boundary condition by imposing the same spring-dashpot boundary condition, as stated in Equation (2.33), to prevent spurious reflections and vibrations close to the fixed ends. However, their study also

suggests that this effect is less significant as compared to the inaccuracies due to incorrect modeling the outer wall. Furthermore, application of spring-dashpot boundary conditions at the artificial boundaries requires calibration of phenomenological constants, which may not be possible due to lack of relevant wall motion data for cerebral aneurysm cases. Therefore, in FSI simulations in Chapters 3 and 4, with the exception of the inlet face for the analysis in Chapter 3, a Dirichlet condition is imposed on the artificial boundaries. Discussion of any additional details is deferred to the pertinent chapters.

2.3.6 Estimating Arterial Pre-Stress

As pointed out by several FSI studies in the past [30]–[33], the vascular geometry obtained from imaging data is not stress free. Depending on the time point in the cardiac cycle when the images are acquired, the arterial wall will have residual stresses as a result of the blood pressure due to incoming flow. Therefore, appropriate initialization of this residual stress state of the geometry is necessary to obtain accurate vessel wall deformations. Hsu and Bazilevs [34] proposed a methodology to account for the residual stress by estimating a "pre-stress" tensor for the arterial wall geometry. Accordingly the second Piola-Kirchhoff stress tensor $\mathbf{S}$ in Equation (2.1) is modified by including an additional pre-stress tensor $\mathbf{S}_0$, as:

$$\int_{\Omega_s^0} \left[\rho_s \mathbf{W} \cdot (\ddot{\mathbf{u}} - \mathbf{f}) + \nabla_{\mathbf{X}} \mathbf{W} : \mathbf{F}(\mathbf{S} + \mathbf{S}_0)\right] d\Omega_s^0 - \int_{\Gamma_{Ih}^0} \mathbf{W} \cdot \mathbf{h}\, d\Gamma^0 - \int_{\Gamma_{Eh}^0} \mathbf{W} \cdot \mathbf{h}\, d\Gamma^0 = 0. \quad (2.34)$$

Here, $\Gamma_{s,h}^0 = \Gamma_{Ih}^0 \cup \Gamma_{Eh}^0$ where Γ_{Ih}^0 is the fluid-solid interface, and Γ_{Eh}^0 is the rest of the boundary with natural boundary conditions.

By definition, the pre-stress tensor $\mathbf{S}_0$ is the residual stress that is in equilibrium with incoming blood flow's tractions (at the time point in the cardiac cycle at which image data is acquired) for zero displacement i.e.,

$$\int_{\Omega_s^0} \left[\nabla_{\mathbf{X}} \mathbf{W} : \mathbf{S}_0 - \rho_s \mathbf{W} \cdot \mathbf{f}\right] d\Omega_s^0 - \int_{\Gamma_{Ih}^0} \mathbf{W} \cdot \mathbf{h}_{\text{FSinterface}}\, d\Gamma^0 - \int_{\Gamma_{Eh}^0} \mathbf{W} \cdot \mathbf{h}\, d\Gamma^0 = 0. \quad (2.35)$$

Here, the traction $h_{\text{FSinterface}}$ on the fluid-solid interface may be obtained from separate rigid-wall simulation data (steady or pulsatile) extracted at the same flow conditions as those during image acquisition. Equation (2.35) is a scalar equation for a tensor unknown, $\mathbf{S}_0$, thus has, in principle, an infinite number of solutions. Hsu and Bazilevs [34] proposed an algorithm to compute a particular solution, which has been implemented in svFSI. The same will be used to estimate pre-stress in the initial subject/animal-specific geometries in the subsequent specific aims. A flowchart of the algorithm is presented in Figure 2.5.

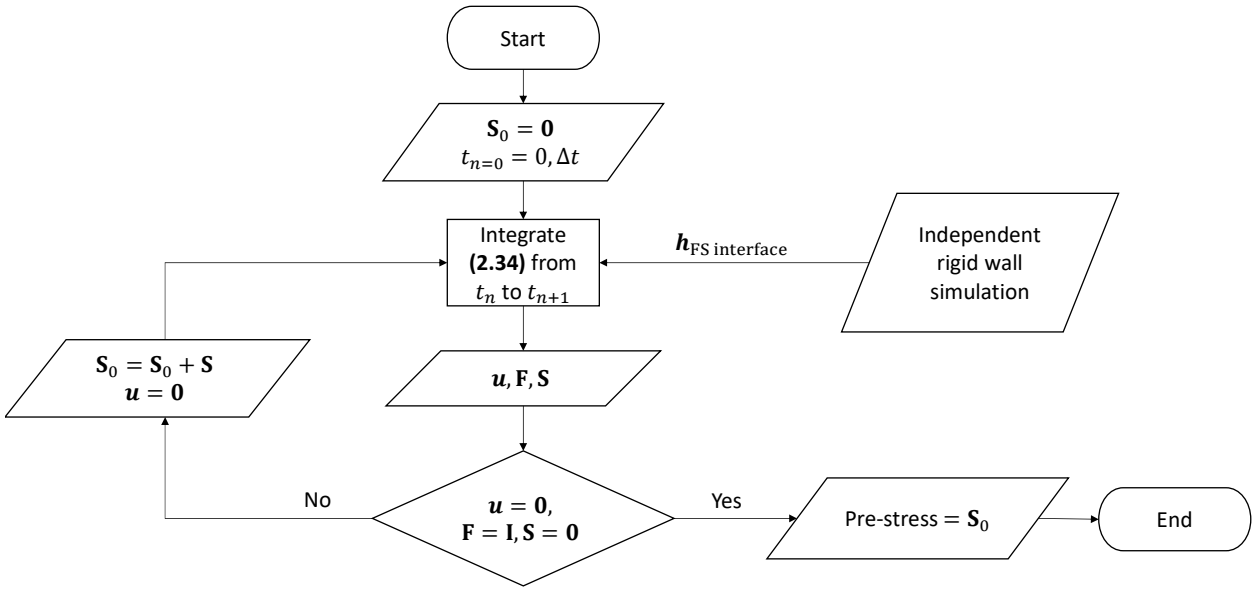

Figure 2.5. Algorithm to obtain a particular solution for the pre-stress $\mathbf{S}_0$. A rigid wall flow simulation is first performed independently to provide the traction $h_{\text{FSinterface}}$ at the fluid-solid interface.

Initial Conditions

Due to their periodic nature, cardiovascular simulations are typically run for several cardiac cycles to ensure that the initial transients associated with "flow start-up" are eliminated. However, appropriate initial conditions are key in achieving this desired periodic solution in the least number of cardiac cycles. In the present case, a distinction is made between the flow simulations (required in generating arterial wall thickness or pre-stress tractions) and FSI simulations.

Based on investigations from a previous study involving flow-only CFD simulations of arterioveneous malformations (AVMs) [35], periodic behaviour is found to be achieved within two cardiac cycles with zero pressure and velocity initialization. Accordingly, flow simulations in subsequent studies have been initialized with zero flow and pressure and run for at least two cardiac cycles.

While specifying the initial conditions for FSI simulations, the flow rate at the time point corresponding to acquisition of image data is chosen as the starting point, $Q(t = 0)$, of the cardiac cycle. This ensures consistency with the pre-stress calculations from Section 2.3.6 and enables the prescription of zero displacement and pre-stress tensor as initial deformation and stress state of the solid domain respectively. The flow domain solution (velocity and pressure) is initialized using data from the same numerical simulation used to generate $h_{\text{FSinterface}}$ (see Section 2.5). FSI simulations are additionally run for multiple cardiac cycles (at least two) and checked for periodicity of the solution, before being considered as valid numerical results.

2.4 Generating Conformal Meshes for ALE FSI

The svFSI solver requires flow and structural domain meshes that are conformal at the fluid-solid interface. With the standard mesh generation workflow available within the SimVascular platform using the TetGen meshing tool [36], it is impossible to generate conformal meshes with boundary layer mesh refinement in the fluid domain for arterial vessel walls with nonuniform wall thickness. Additionally, svFSI lacks capability of accepting meshes in formats other than the standard VTK format. A novel mesh generation workflow was

developed to overcome the meshing limitations of the SimVascular platform and allow for importing meshes created using the commercial CAE tool ANSYS® Workbench for running svFSI simulations. The details are presented in this subsection.

The first step in the process involves generating conformal tetrahedral meshes for the flow and structural domain using the meshing tool of choice. In this specific case, the ANSYS® meshing tool within the ANSYS® Workbench environment was used and each mesh (fluid and solid) was separately exported in the ANSYS® Fluent-compatible (`.msh`) format. These meshes are converted to `.vtu` volumetric mesh using the open-source mesh conversion tool FEconv [37]. Subsequently, mesh attribute cleanup, geometric scaling (depending on the problem requirements) and node and element renumbering is performed in Paraview. This step is essential to produce meshes that the mesh parser in svFSI can read without errors. The end result is a renumbered `.vtu` volumetric tetrahedral mesh and `.vtp` surface mesh of the external bounding surface. A custom python [38] script developed in-house is then executed within the SimVascular python shell to extract the individual boundary faces (on which boundary conditions are to be imposed) from the combined `.vtp` file generated above. The python script used to extract the boundary faces is provided in Appendix B.

3. SPECIFIC AIM 2: EXTERNAL TISSUE SUPPORT PARAMETER CHARACTERIZATION FOR AngII INFUSED MOUSE MODELS OF THORACIC AORTIC ANEURYSMS

The material presented in this chapter is under review for publication in *Engineering with Computers* under the title "Estimating external tissue support parameters with fluid-structure interaction models from 4D ultrasound of murine thoracic aortae"

Authors: Tanmay C. Shidhore[†], Hannah L. Cebull[†], Megan C. Madden, Ivan C. Christov, Vitaliy L. Rayz and Craig J. Goergen

Tanmay C. Shidhore performed the image segmentations, geometry pre-processing, setting up and running fluid-structure interaction simulations and data post processing. Hannah L. Cebull acquired the 4D US, PWD and histological data and performed data post-processing. Megan C. Madden performed image segmentation, setting up and running fluid-structure interaction simulations. All authors contributed to writing and reviewing the manuscript. [†]These authors contributed equally to this work.

3.1 Background

The thoracic aorta is a highly pulsatile elastic artery in the body [39], [40]. While computational fluid dynamics (CFD) simulations provide an effective technique for quantifying blood flow patterns and estimating hemodynamic parameters, these models lack important biomechanical information on the arterial wall. Furthermore, previous studies have shown that wall shear stress (WSS), an important hemodynamic metric affecting endothelial cell response, is over-estimated in CFD simulations where the wall is assumed to be rigid [41], [42]. Therefore, fluid-structure interaction (FSI) modeling is needed to accurately capture the mechanics of the aortic wall and the effect of feedback between hemodynamic and tissue mechanical forces on hemodynamic quantities of interest. There remains a critical need for improving computational modeling of the thoracic aorta, as thoracic aortic aneurysms

(TAAs) affect 10 out of 100,000 people [43]. Current intervention methods often focus on the volume and diameter of TAAs, neglecting geometry, vessel motion, and effect of blood flow. Importantly, the biomechanics of wall deformation captured through FSI modeling allows for improved understanding of aneurysmal growth and progression by providing better estimates of WSS and other hemodynamic parameters [44], [45]. Therefore, improved biomechanical prediction capabilities through FSI modeling is crucial, as dissections have been reported in patients with vessel diameters below the typical intervention threshold of 5 to 6 cm [46], [47].

There are many contributing factors to the complexity of TAAs on both micro- and macroscopic scales [48]. On a cellular level, changing levels of elastin, collagen, and inflammatory cells influence the biomechanics of the vessel [49], [50]. Further, the heart, spine, and other external tissues affect the vessel movement on a macroscopic level [27], [51], and the geometry of the vessel itself (with the aortic valve, arch, and branching vessels) results in complex flow patterns, even in non-diseased cases [52]. Heterogeneous biomechanics of the thoracic aorta should be accounted for through a robust computational methodology that considers all these influencing factors to improve understanding of the role of biomechanical forces in TAAs, potentially improving non-invasive diagnoses.

The angiotensin II (AngII)-infused mouse model is a popular murine model to study disease progression of both thoracic and abdominal aortic aneurysms [53]. Animals develop hypertension, causing expansion and stiffening within the thoracic aorta and occasionally dissection in the suprarenal abdominal aorta [54]. Recently, there has been increased interest in computational modeling of small animals because of the ability to collect image data both pre- and post-aneurysm formation, with a view towards augmenting experimental measurements with high-resolution computational data [55]. From the perspective of developing high fidelity computational models, the modeling strategy of using tissue support boundary conditions is highly suitable as such models can be easily customized to simulate a variety of experimental conditions *in-silico* without having to redo animal experiments. However, for the purposes of conducting such FSI simulation studies of murine models, there are limited reports in the literature on suitable boundary conditions on the outer vessel wall that account for the effect of the surrounding complex biological environment. Specifically, there

are no reported studies on characterizing the phenomenological tissue support parameters (see Equation (2.33)) for murine models of TAAs. In this study, this gap in knowledge is addressed by performing a longitudinal computational FSI analysis of murine aortas and calibrating the tissue support parameters via comparison to experimental four-dimensional ultrasound (4DUS) data.

3.2 Methods

3.2.1 Animals and Aortic Expansion

Under the approval of the Purdue Animal Care and Use Committee, male wildtype C57BL/6J mice (23.5 g $\pm$ 1.3; 32 weeks old; $n = 5$) from The Jackson Laboratory (Bar Harbor, ME) were infused with AngII (MW: 1046.19; Bachem, Torrance, CA) for 28 days via subcutaneous implantation of mini-osmotic pumps in the dorsum of each mouse (ALZET Model 2004; DURECT Corporation, Cupertino, CA) [56]. The pumps systemically delivered AngII dissolved in saline solution (0.9% sodium chloride) at a rate of 1000 ng/kg/min. One of the five mice died before the end of the study due to aortic rupture. The remaining four mice were euthanized 28 days post-implantation with overdose of carbon dioxide.

3.2.2 Image Acquisition, Blood Pressure, and Histology

High-resolution ultrasound images (Vevo2100 Imaging System; FUJIFILM VisualSonics Inc., Toronto, Ontario, Canada) were acquired at baseline and 28 days post angII infusion for each mouse (referred to hereafter as "Day 0" and "Day 28" time points respectively). A depilatory cream was applied before imaging to remove hair from the region of interest to minimize image artifacts. To obtain inlet velocities, pulsed-wave Doppler (PWD) waveforms were collected. A custom MATLAB code was then used to quantify the PWD data for the inlet flow boundary conditions [57]. In order to visualize vessel geometry and wall deformation, 4DUS from individual electrocardiogram-gated kilohertz visualization (EKV) cine images was collected. To acquire the 4DUS scans, an automated technique that collected an EKV every 60 µm using a 40 MHz center frequency linear array transducer (MS550D FUJIFILM VisualSonics Inc.; axial resolution = 40 µm; lateral resolution = 90 µm) in a

long axis view was used until the majority of the thoracic aorta and branches off of the arch were captured [58].

At the Day 0 and Day 28 time points, diastolic and systolic blood pressure data from conscious mice using a tail cuff system (CODA 2 Channel Standard, Kent Scientific, Torrington, CT) was also collected. The mice were acclimated to the cone restraints and tail cuffs prior to collection. Following the final imaging and blood pressure measurements, the vessels were excised and fixed for a histological analysis using Movat's Pentachrome stain. Histological slices were used to obtain average thickness values incorporated in Day 28 wall properties (see image in Figures 3.1b and 3.2a).

3.2.3 Computational Geometries

The fluid and solid geometries were obtained as explained below.

Fluid Domain Geometry

Ultrasound images of flow domain at diastole for one of the mice were segmented to be used as a representative model. The specific animal case was chosen such that it matched the mean expansion of all four mice in the ascending aorta region (70%). The geometry included the ascending aorta and portions of the brachiocephalic trunk, left common carotid artery, left subclavian artery, and the descending aorta via 4DUS imaging data acquired at days 0 and 28 as described in Section 3.2.2. Segmentations were performed at end diastole, as well as peak systole to be used for maximum *in vivo* deformation measurements. As the descending aorta was not entirely visible in the image data, the segmentations were artificially extended. Subsequent smoothing and cleanup of the geometry was performed in the commercial computer-aided design (CAD) tool Geomagic® Design X to eliminate sharp edges, bumps, and other initial segmentation artifacts.

Solid Domain Geometry

For the blood flow domain extracted and discussed in the previous subsection, the nonuniform arterial wall thickness (the solid computational domain) was estimated by solving the

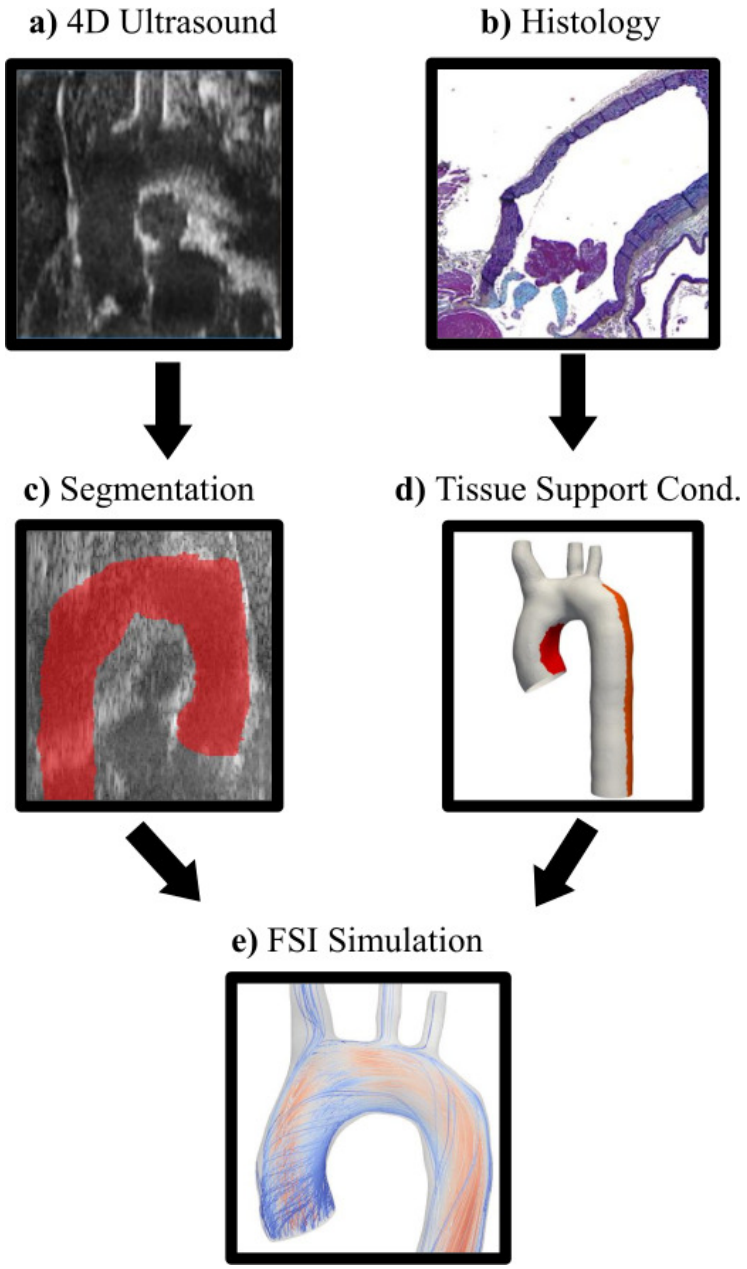

Figure 3.1. Proposed modeling pipeline for calibrating tissue support parameters for FSI simulations. Panels a – e highlight the general steps in this study beginning with a) acquiring 4DUS data and b) collecting histological data. Segmentations of the lumen c) can be extracted to generate the geometry of the flow domain. Meanwhile, histological data provides us geometry of the outer wall (for Day 28) which may then be used to prescribe heterogeneous tissue support parameters (red/white), as in d). This is assembled into a physiologically realistic FSI model e).

Laplace equation over the luminal surface as originally proposed by Bazilevs *et al.* [59]. Specifically, the thickness $t(\mathbf{x})$ at location $\mathbf{x}$ along the luminal surface (inner wall $\partial\Omega_{\text{inner}}$) was found as the solution to:

$$\nabla^2 t(\mathbf{x}) = 0 \quad \text{on} \quad \partial\Omega_{\text{inner}}. \tag{3.1}$$

The domain for the Laplace equation is the inner wall $\partial\Omega_{\text{inner}}$, and boundary conditions are prescribed on the sets of curves at the inlets and outlets of the computational geometry.

The thickness values prescribed at the inlet and outlets as boundary conditions are given in Table 3.1. For the Day 0 time point, thickness values corresponding to 10% of the average vessel inlet/outlet diameter were prescribed, following Hsu and Bazilevs [34]. For the Day 28 time point, *ex vivo* histology measurements from all four mice at the respective inflow and outflow branches were obtained and the averaged vessel wall thickness values from these measurements was prescribed. An example of the geometries for the flow domain and the solid domain is shown in Figure 3.2b.

3.2.4 Mesh Generation

Tetrahedral meshes were created for the fluid and solid domains, enforcing node conformity at the fluid-solid interface. To ensure that the shear stress was computed accurately at the fluid-solid interface, local mesh refinement was incorporated in the fluid mesh up to a constant thickness of 0.06 mm from the fluid-solid interface. A grid independence analysis was performed on the Day 0 geometry to ensure that the computational results were inde-

Table 3.1. Wall thickness values prescribed at the inlet and outlet locations for each time point.

Time Point	ATA	DTA	BCA	LCCA	LSA
Day 0 (mm)	0.14	0.12	0.05	0.04	0.03
Day 28 (mm)	0.15	0.13	0.09	0.07	0.06

ATA = ascending thoracic aorta, DTA = descending thoracic aorta, BCA = brachiocephalic artery, LCCA = left common carotid artery, LSA = left subclavian artery

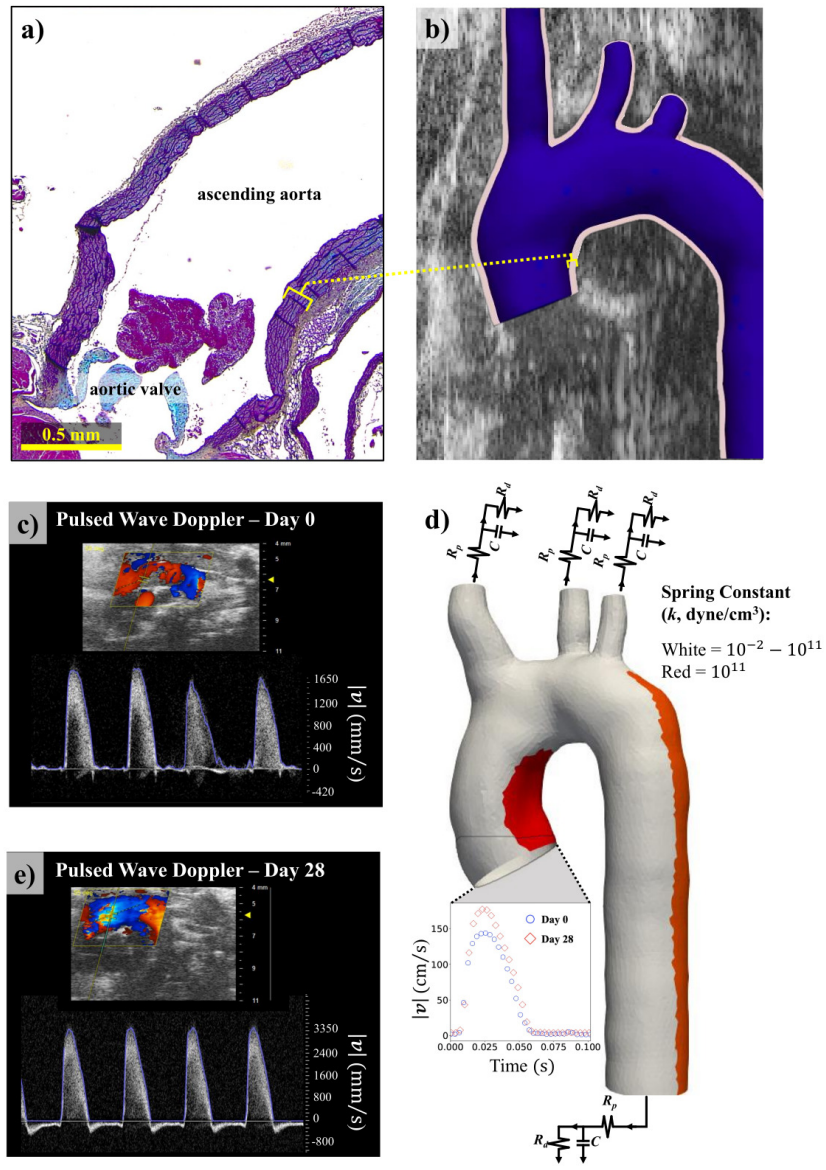

Figure 3.2. Previous literature [34] and histology a) were used to determine vessel wall thickness at days 0 and 28 respectively. b) shows the solid (transparent red) and fluid (blue) segmented domains of the Day 28 model over a static slice of the corresponding 4D ultrasound image. c) and e) show the pulsed-wave Doppler at Day 0 and Day 28 that was used to inform the inlet boundary condition in panel d). The Windkessel RCR model used at the outlets, along with heterogeneous (red and white regions) external tissue support (applied to simulate *in vivo* conditions) on the Day 0 outer wall geometry, are shown in d).

pendent of the core and near-wall mesh refinement resolutions (see Section 3.2.5 for further details).

3.2.5 Grid Independence

In order to ensure that computational quantities reported, such as pressure, velocity and wall shear stress, were independent of the grid resolution of the fluid domain's mesh, a grid sensitivity analysis was performed. The pertinent details for each mesh are shown in Table 3.2. A two-step approach was used to establish grid independence. First, a core mesh resolution was determined such that pressure and velocity were independent of the core mesh resolution. Second, varying degrees of mesh refinement close to the fluid-solid interface were implemented on top of the chosen core mesh resolution from the previous step, to ensure that the computed wall shear stress was independent of the near-wall mesh refinement resolution. In Figure 3.3c, d, e and f, the area-averaged and point-wise pressure and velocity magnitude at the inlet plane, as well as at an arbitrary point located in the interior of the ascending region of the aorta (see Figure 3.3a) are plotted over a single cardiac cycle.

Based on the plots in Figure 3.3c, d, e, and f, it was observed that the pressure and velocity magnitude values computed on both the coarse and medium grid (i.e. with $\Delta x = 0.015$ cm and $\Delta x = 0.01$ cm) were within a 5% margin of the values computed on the fine grid. However, in Figure 3.3d, the velocity magnitude for the coarse grid ($\Delta x = 0.015$ cm) was beyond this tolerance margin. Therefore, $\Delta x = 0.01$ cm was determined to be the core mesh resolution of choice.

Next, Figure 3.4 shows the x, y, and z components of the WSS (wall shear stress) computed at a point on the surface of the ascending aorta. Here, the core mesh resolution was identical in all cases ($\Delta x = 0.01$ cm). However, close to the fluid-solid interface, different number of layers of mesh refinement (0, 3, 4, and 5) were considered (see Figure 3.4a) From Figures 3.4b, c and d, non-trivial difference ($> 5\%$) between the surface shear stress values computed on meshes with and without mesh refinement was observed. Furthermore, meshes with different levels of mesh refinement ($N_{\text{BL}} = 3, 4$, and 5) yield shear stress values within the above tolerance limit with minor differences in the computation time. Therefore, a mesh

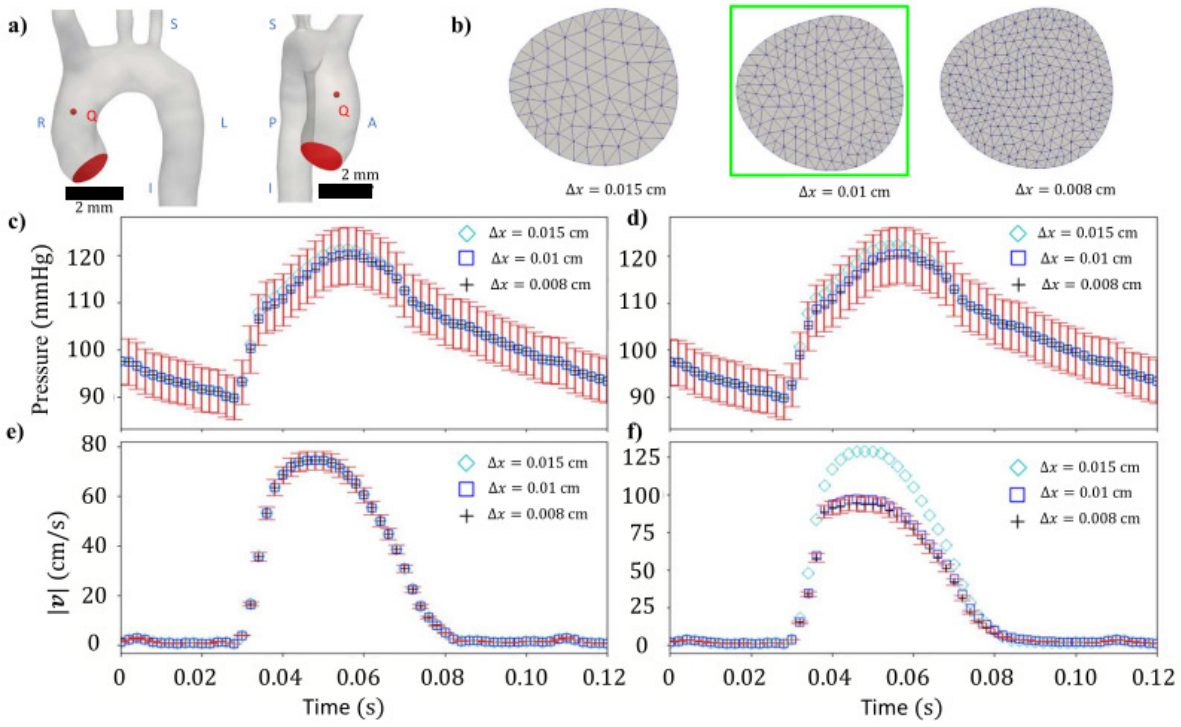

Figure 3.3. Pressure and velocity data over a cardiac cycle at the inlet plane (panels c and e) and at a point (panels d and f) in the interior of the ascending aorta (shown in a) for different mesh resolutions (shown in b). The error bars of each plot point show a deviation of 5% from the corresponding value on the finest mesh ($\Delta x = 0.008$ cm). Abbreviations used – $|\mathbf{v}|$: Velocity magnitude, R: Right, L: Left, A: Anterior, P: Posterior. Based on the above plots, $\Delta x = 0.01$ cm was chosen as the optimal core mesh resolution.

refinement level of $N_{\text{BL}} = 4$ was chosen balancing the need for increased resolution with the corresponding computational cost.

A constant time step of $\Delta t = 10^{-5}$ s was used for all cases. Table 3.2 reports an estimate of the maximum cell-based Courant number computed for each of the meshes used, over a single cardiac cycle. The Courant number was computed as:

$$\text{CFL} = \frac{|\mathbf{v}|\Delta t}{\Delta x}, \tag{3.2}$$

where $|\mathbf{v}|$ is the velocity magnitude at the cell center, Δt is the time step size, and Δx is a length scale computed for each cell as $\Delta x = \mathcal{V}^{1/3}$, where $\mathcal{V}$ is the cell volume.

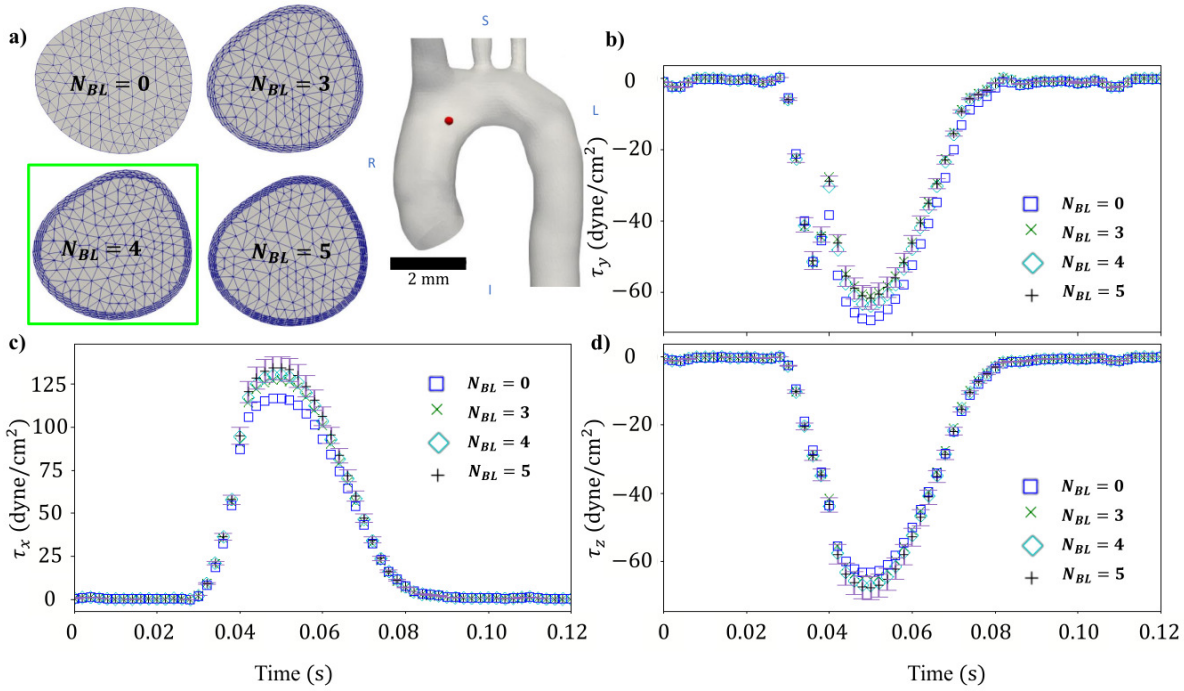

Figure 3.4. Components (b,c,d) of the WSS over a cardiac cycle at a point on the interior surface of the ascending aorta (shown by a dot in the model geometry in a), for different number of boundary layers each. N_{BL} represents the number of layers of boundary layer elements. Here, $N_{\mathrm{BL}} = 0$ represents a mesh without boundary layer refinement. The error bars on each plot point show a deviation of 5% from the corresponding value on the mesh with the largest number of boundary layer refinements (i.e. $N_{\mathrm{BL}} = 5$). Based on the above plots, the boundary layer mesh resolution corresponding to $N_{\mathrm{BL}} = 4$ was chosen as for the FSI simulations. Abbreviations used – R: Right, L: Left, S: Superior, I: Inferior.

It was observed that, for cases for which the maximum CFL > 1, only a few cells (< 5) outside the region of interest (viz. the ascending aorta) exceeded the threshold. This observation, together with the fact that the time integration scheme implemented in svFSI is an implicit scheme [24], allowed for using the same time step size of $\Delta t = 10^{-5}$ s for the subsequent FSI simulations as well.

Table 3.2. Mesh details for grid optimization.

Δx_{core} (cm)	N_{BL}	N_{elements}	N_{nodes}	Max. CFL
0.01	0	169,749	32,750	0.4
	3	189,832	36,375	1.04
	4	190,015	36,401	1.05
	5	191,098	36,744	1.01
0.15		53,032	11,078	0.28
0.08		326,791	61,263	0.49

3.3 Solver Details and Boundary Conditions

Three-dimensional numerical simulations were performed using the svFSI solver, as described in Section 2.3.

3.3.1 Flow Domain

Blood was modeled as a Newtonian fluid with constant density ρ_f and viscosity μ_f, the values of which were obtained from literature data [60] (see Table 3.3). These values were assumed to be the same for both the Day 0 and 28 time points.

3.3.2 Structural Domain

As mentioned in Section 2.3.1, the arterial wall was modelled as nearly incompressible hyperelastic material with material properties E and $\nu = 0.49$. Different values were assumed for E at the Day 0 and 28 time points to account for arterial stiffening due to AngII infusion. The Young's moduli for the Day 0 and 28 time points were estimated using circumferential stress-stretch data for wildtype C57BL/6J and AngII-infused apolipoprotein $\text{E}^{-/-}$ mice, respectively, as reported by Bellini *et al.* [61]. For a biaxial state of stress of an incompressible neo-Hookean material, the theoretical relationship between circumferential stress $\sigma_{\theta\theta}$ and circumferential stretch ratio $\lambda_{\theta\theta}$ is:

$$\sigma_{\theta\theta} = -p + \frac{E}{3}\lambda_{\theta\theta}^2, \tag{3.3}$$

Table 3.3. Values of the fluid and solid material properties used for simulations.

Property	Day 0	Day 28
Blood density ρ_f	1.06 g/cm^3	1.06 g/cm^3
Blood viscosity μ_f	4 cP	4 cP
Arterial wall density ρ_s	1.0 g/cm^3	1.0 g/cm^3
Arterial wall Young's Modulus E	3.11×10^6 dyne/cm^2	3.30×10^6 dyne/cm^2
Arterial wall Poisson ratio ν	0.499	0.499

where p is the Lagrange multiplier that enforces the incompressibility constraint. Therefore, using the biaxial stress-stretch data reported in [61], the Young's modulus was estimated to be three times the slope of the best fit line to $\sigma_{\theta\theta}$ versus $\lambda_{\theta\theta}$ (see Figure 3.5). The values are reported in Table 3.3.

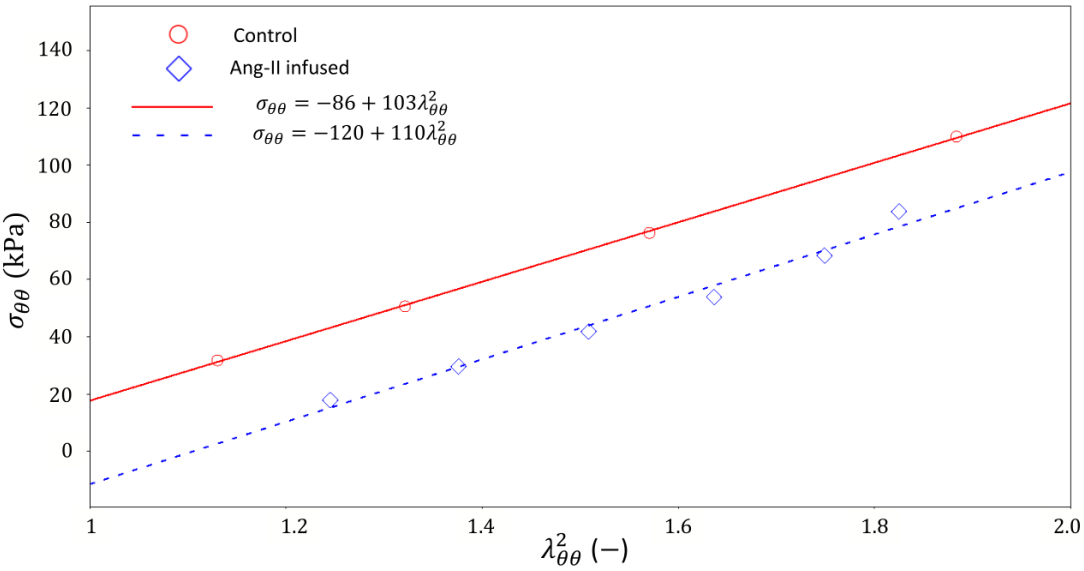

Figure 3.5. Experimental circumferential stress vs. stretch-squared data from Bellini *et al.* [61] along with best fit line(s) and corresponding best fit equation(s). The Young's modulus (in kPa) was estimated to be three times the fitted slope.

3.3.3 Arterial Pre-Stress

Arterial pre-stress was computed as described in Section 2.3.6. In this study, since 4D US images at diastole were used for obtaining the computational geometry, the flow traction data at diastole, obtained from a separate pulsatile rigid-walled flow simulations was used to compute the pre-stress tensor $\mathbf{S}_0$ (see Equation (2.35)) for both the Day 0 and Day 28 geometries.

3.3.4 Fluid Domain Boundary Conditions

The Womersly number values,calculated using Equation (2.30), for Day 0 and Day 28 time points were found to be 2.7 and 2.9, respectively. Since both values were close to Wo = 2, a parabolic flow profile was implemented over the cross-section.

The temporal area-averaged inlet velocity profiles over a single cardiac cycle were acquired at Days 0 and 28 time points for each mouse using PWD measurements. Based on these measurements, an averaged temporal inlet velocity was estimated for the representative Day 0 and Day 28 cases by averaging the velocity values over all four mice. Figure 3.2d shows the temporal velocity profile used in simulations at both time points. This velocity profile was multiplied by the cross-sectional area at the inlet to obtain the inlet flow rate profile, which was imposed as a parabolic, periodic inlet flow rate boundary condition.

To account for the effect of the downstream vasculature, a three-element Windkessel RCR boundary condition was imposed at each of the outlets [62], as shown in Figure 2.4. Initial estimates of the total arterial resistance R^0_{total} and capacitance C^0_{total} were obtained as:

$$R^0_{\text{total}} = \frac{\tilde{P} - P_0}{\tilde{Q}}, \tag{3.4a}$$

$$C^0_{\text{total}} = \frac{Q_s - Q_d}{P_s - P_d}\Delta t. \tag{3.4b}$$

Here, $\tilde{P}$ and $\tilde{Q}$ are the time-averaged pressure and flow rate, respectively, over a single cardiac cycle. Meanwhile, P_s, Q_s and P_d, Q_d are the systolic and diastolic pressures and flow

rates, respectively. Finally, P_0 is the distal pressure, and Δt is the time difference between Q_s and Q_d.

Subsequently, as outlined in [63], the distal pressure, total resistance, and capacitance were tuned in an iterative fashion such that both peak systolic, P_s, and pulse, $P_s - P_d$, pressures matched the corresponding tail cuff measurement values within an error margin of 10%. Rigid-wall pulsatile flow simulations were run for six cardiac cycles, and the results from the fourth cardiac cycle were used in the fine-tuning process. The resistance across each individual outlet were distributed using Murray's law ($m = 3$) [64]:

$$R_{\text{out},\ell} = \frac{\sum_{k=1}^{p} \sqrt{A_k^m}}{\sqrt{A_\ell^m}} \cdot R_{\text{total}}. \tag{3.5}$$

Here, R_{total} is the net downstream resistance, A_ℓ is the cross-sectional area of the ℓ^{th} outlet, and p is total the number of outlets. The capacitance of each individual outlet branch is calculated as proposed in [63]:

$$C_{\text{out},\ell} = \frac{R_\ell}{R_{\text{total}}} \cdot C_{\text{total}}. \tag{3.6}$$

For each outlet branch, the ratio of the distal to proximal resistance was assumed to be 1:9 [28]. Tables 3.4 and 3.5 list the animal-averaged systolic and diastolic pressures obtained from tail cuff measurements, along with the values obtained via this fine tuning process for the proximal resistance R_p, the distal resistance R_d, and the capacitance C at each outlet for the Day 0 and Day 28 time points, respectively. It should be emphasized that the RCR parameter values reported in Tables 3.4 and 3.5 are not physiologically realistic but simply to ensure that inlet diastolic and pulse pressures are within a 10% margin of corresponding values from cuff measurements.

3.3.5 Structural Boundary Conditions

On the natural boundary (i.e. the outer wall), the Robin boundary condition, previously introduced in Equation (2.33), was prescribed. Following the work in [28], a simplification

Table 3.4. RCR parameter values at each outlet and pressures for Day 0.

Parameters	DTA	BCA	LCCA	LSA
R_p ($\times 10^4$ dyne $\cdot$ s/cm^5)	1.3	18.5	29.0	86.6
R_d ($\times 10^4$ dyne $\cdot$ s/cm^5)	11.5	166.7	260.6	779.0
C ($\times 10^{-7}$ cm^5/dyne)	6.3	0.4	0.3	0.1
P_0 (mmHg)	73.2			
P_s (mmHg)	115.7			
P_d (mmHg)	83.2			

DTA = descending thoracic aorta, BCA = brachiocephalic artery, LCCA = left common carotid artery, LSA = left subclavian artery; R_p = proximal resistance, R_d = distal resistance C = capacitance, P_0 = distal pressure, P_s = systolic pressure, P_d = diastolic pressure

Table 3.5. RCR parameter values at each outlet and pressures for Day 28.

Parameters	DTA	BCA	LCCA	LSA
R_p ($\times 10^4$ dyne $\cdot$ s/cm^5)	1.3	8.7	22.4	11.2
R_d ($\times 10^4$ dyne $\cdot$ s/cm^5)	11.7	78.0	201.7	100.7
C ($\times 10^{-7}$ cm^5/dyne)	3.8	0.58	0.22	0.45
P_0 (mmHg)	111.4			
P_s (mmHg)	164.5			
P_d (mmHg)	121.4			

DTA = descending thoracic aorta, BCA = brachiocephalic artery, LCCA = left common carotid artery, LSA = left subclavian artery; R_p = proximal resistance, R_d = distal resistance C = capacitance, P_0 = distal pressure, P_s = systolic pressure, P_d = diastolic pressure

was introduced in Equation 2.33, wherein the number of parameters to be tuned were reduced by identically setting the damping coefficient c and the constant pressure p_0 to 0. Furthermore, a heterogeneous value was prescribed for the spring constant k [27]. Specifically, the outer surface of the arterial wall was divided into three regions to model contact with the spine and pulmonary artery regions (see, e.g., red regions in Figure 3.2d) at both the Day 0 and Day 28 time points. Based on observations of wall motion in the 4DUS imaging data, the estimated 2D Green-Lagrange strain of the pulmonary artery at the location under the aortic arch did not decrease (3.1% $\pm$ 1.1 increase) at Day 28 as compared to the thoracic aorta (22.5%$\pm$1.1 decrease), despite expansion of the thoracic aorta from Day 0 to 28 (18.9%

increase in diameter). Therefore, both contact areas were simulated by imposing a high stiffness value ($k = 10^9$ dyne/cm^3) to account for this strong tethering. This value was kept constant across all the FSI simulations at Day 0 and 28. A spatially uniform stiffness value, which was progressively varied across different simulations (see Section 3.3.6), was imposed on the remainder of the outer wall, hereafter referred to as the "outer wall with variable tissue support". (see, e.g., white region in Figure 3.2e). For the solid caps at each flow outlet, a homogeneous Dirichlet boundary condition, $\mathbf{u} = \mathbf{0}$, was imposed. This was found to be consistent with imaging data, which showed the outflow branches at the corresponding locations undergoing minimal displacement. Conversely, the artificial boundary ring at the inlet is influenced by heart motion. This effect was modeled via a Robin boundary condition with the traction prescribed:

$$\boldsymbol{\sigma} \cdot \mathbf{n} = -k(\mathbf{u} \cdot \mathbf{n})\mathbf{n} - c(\dot{\mathbf{u}} \cdot \mathbf{n})\mathbf{n} - p_0\mathbf{n} \quad \text{on} \quad \partial\Omega_{\text{inlet}}, \tag{3.7}$$

where k, c, p_0, and $\mathbf{n}$ are as previously defined for Equation (2.33). In contrast to the boundary condition on the outer wall, given by Equation (2.33), the projection onto the normal direction in Equation (3.7) was used to preclude out-of-plane deformations of the inlet ring, further guaranteed by imposing a large value for the spring constant ($k = 10^{17}$ dyne/cm^3) and setting c and p_0 to 0.

3.3.6 FSI Simulation Parameters

For each time point (Day 0 and Day 28), 3D pulsatile FSI simulations were run for four cardiac cycles. The inlet Reynolds number at peak systole for an intermediate value of tissue support spring parameter ($k = 10^6$ dyne/cm^3) was calculated as

$$\text{Re} = \rho_f v_{\text{peak}} D_{\text{vessel}} / \mu_f, \tag{3.8}$$

where v_{peak} is the centerline velocity at peak systole, and $D_{\text{vessel}} = 2\sqrt{A_{\text{inlet}}/\pi}$ is the effective vessel diameter at the inlet plane, with A_{inlet} being the surface area of the inlet face. This value was estimated to be 358 for the Day 0 time point and 522 for the Day 28 time point. For

the Day 0 case, k values from 10^{-2} to 10^{11} dyne/cm^3 (end points included) were considered for the outer wall with variable tissue support (see Section 3.3.5). An additional simulation was run without any external tissue support — in this case, prescribing a homogeneous Neumann condition ($k = 0$) on the outer wall with variable tissue support (white region in Figure 3.2d). In total, fifteen simulations were performed for Day 0. Each simulation took approximately six hours of CPU time to complete all four cardiac cycles on 120 cores of a single compute node, which consisted of two 64-core AMD Epyc 7662 "Rome" processors (Bell Community Cluster, Rosen Center for Advanced Computing, Purdue University, West Lafayette). After determining optimum tissue support parameter values for the Day 0 time point, a subset of the above tissue support parameter range (10^3 to 10^8 dyne/cm^3) was tested for Day 28. In the results shown below, it was verified that periodicity was achieved after the second cardiac cycle and reported data extracted from the last (fourth) cardiac cycle.

3.4 Results and Discussion

3.4.1 FSI Simulations

A comparison of various flow and structural metrics extracted from the FSI simulations at Days 0 and 28 is presented here. As mentioned in Section 3.3.6, the pulmonary artery and spine tissue support values were fixed while the value prescribed on the remainder of the outer wall is varied. Figure 3.6 shows the pressure contours, wall shear stress (WSS) magnitude contours and wall deformation contours for the largest ($k = 10^{11}$ dyne/cm^3), smallest ($k = 0$) and two intermediate ($k = 10^7$ and 10^8 dyne/cm^3) tissue support values at Day 0. To enable better quantitative comparison, the percentage change (with respect to the least tissue support) in pressure, wall shear stress, and arterial deformation across changing tissue support spring parameter values are listed in Table 3.6. The comparison is made at three separate points (as shown in Figure 3.6a,f and k): Point A, corresponding to the highest spatial peak systolic pressure, Point B, corresponding to the highest spatial peak systolic WSS magnitude and Point C, corresponding to the highest spatial peak deformation magnitude. Point C is located on the ascending aorta, whereas points A and B are located on the aortic arch. Pressure was found to be minimally affected ($< 2\%$ change from lowest to

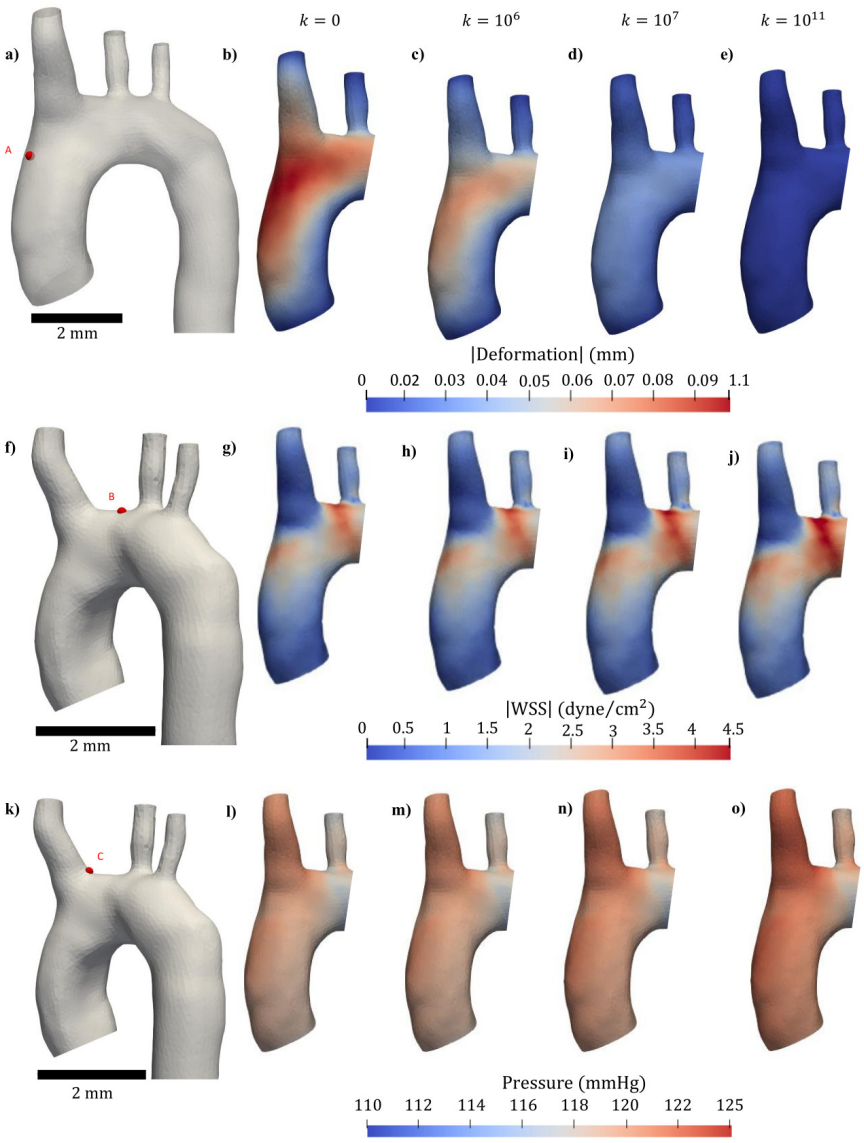

Figure 3.6. Pressure, WSS, and deformation from pulsatile 3D FSI simulations at peak systole for Day 0. In each row, the left-most image shows the location at which the quantity (i.e. pressure, WSS, or deformation) was computed and the right-most image shows the simulation with the highest tissue support value $k = 10^{11}$ dyne/cm^3 on the outer wall with variable tissue support. The three middle columns show simulation results at the lowest tissue support, $k = 0$ and two intermediate k values, $k = 10^6$ dyne/cm^3 and $k = 10^7$ dyne/cm^3. Overall, minimal differences were observed for pressure between models with and without homogeneous external tissue support while WSS and deformation changed appreciably.

highest tissue support value) by changes in the value of k. However, an appreciable increase ($\approx$ 13%) in WSS is observable near the aortic arch from $k = 0$ to $k = 10^{11}$ dyne/cm^3. The largest observable change was naturally found to be in the displacement field, with the largest tissue support case being equivalent to assuming a rigid arterial wall.

Table 3.6. Percentage change in hemodynamic and structural metrics across varying tissue support spring parameter at Day 0. Values of k listed are in dyne/cm^3.

Quantity	Point	$k = 10^6$	$k = 10^7$	$k = 10^{11}$
Deformation magnitude (%)	A	29.63	68.52	99.95
	B	29.03	69.35	99.92
	C	29.09	73.64	99.97
WSS magnitude (%)	A	3.58	4.25	1.12
	B	1.85	7.88	13.85
	C	2.17	3.89	3.98
Pressure (%)	A	0.15	0.73	1.77
	B	0.16	0.74	1.32
	C	0.12	0.62	1.17

WSS = Wall Shear Stress

Large elastic arteries close to the heart undergo non-trivial deformation and translation [27]. Therefore, in order to determine the goodness of fit between the simulation and imaging data, cross-sections at three different locations within the region of interest (ascending aorta) were extracted at peak systole and compared them with corresponding cross-sections from 4DUS imaging data. This comparison was performed for both time points (Day 0 and Day 28). Figure 3.7 shows the comparison for one of the cross-sections at each time point.

For the Day 0 case, it was observed that except for a small range of values of k, the cross-section profiles coincided with either the highest or lowest tissue support curves. Furthermore, the match between the cross-section from segmentations and the cross-sections from simulations varied with location. For example, in the zoomed-in view of the cross-sections, shown in Figure 3.7f, the white curve matches better with the cyan curve ($k = 10^6$ dyne/cm^3) towards the anterior end and the maroon curve ($k = 10^7$ dyne/cm^3) towards the posterior end. This indicated that a qualitative visual comparison would be inadequate

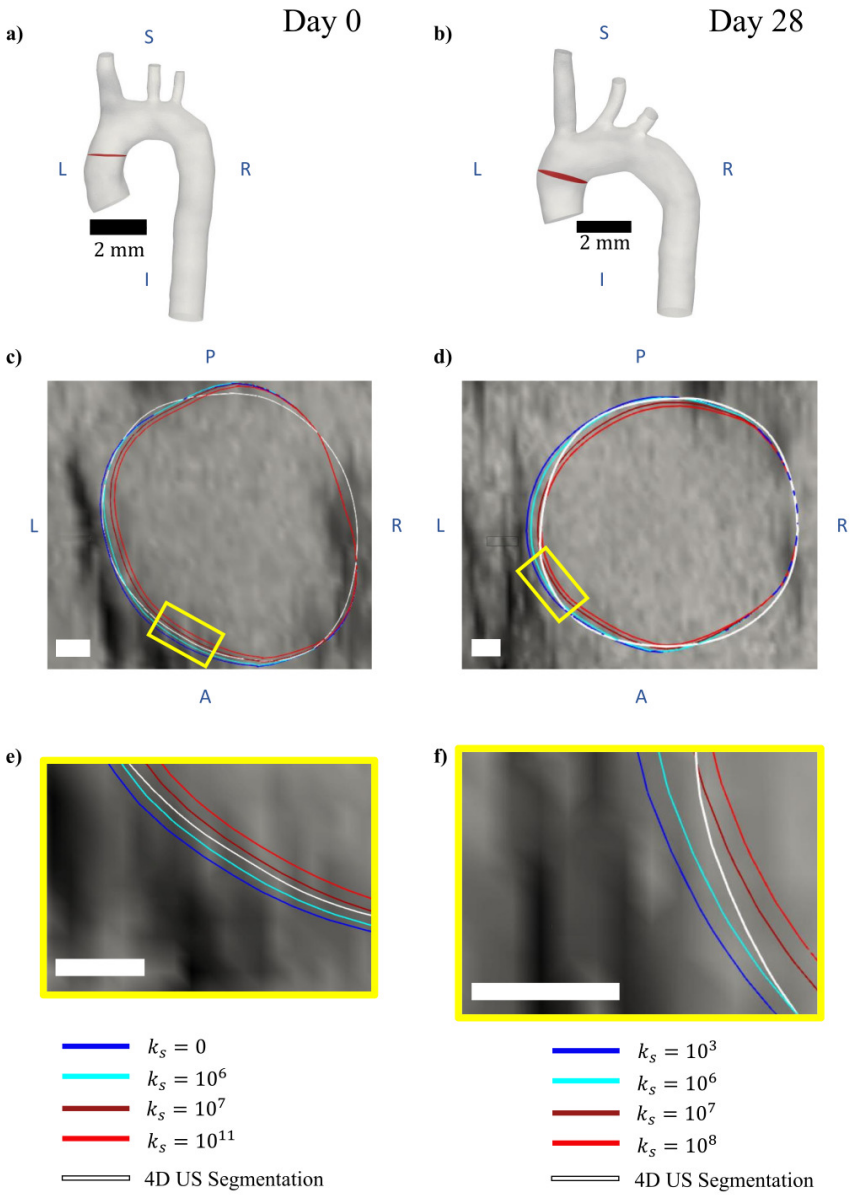

Figure 3.7. Visual comparison of 4D US and FSI simulation data at peak systole. a) and b) show the locations of the cross-sections being considered at Day 0 and Day 28 respectively. c) and d) show the cross-sections (colored rings) obtained for varying values of tissue support parameter k (in dyne/cm^3) overlaid on the 4D US image slice at the corresponding cross-section at peak systole. The corresponding segmentation cross-section is shown by the white ring. e) and f) represent zoomed-in views of regions on the cross-section (represented by the yellow box in c) and d). The white bar in sub-panels c)-f) corresponds to a scale of 0.2 mm.

to determine an optimum value or range of values which provide the best fit for the 4D US data. Therefore, two quantitative metrics were evaluated: the effective diameter and the non-overlapping cross-sectional area at all three cross-sections within the region of the ascending aorta at peak systole. The effective diameter, indicative of arterial expansion, was computed as:

$$d_{\text{effective}} = 2\sqrt{\frac{A_{\text{CS}}}{\pi}}, \tag{3.9}$$

where A_{CS} is the corresponding cross-sectional area. The non-overlapping area A_{NO} between the cross-sections from segmentation and simulations at a given location was computed as:

$$\begin{aligned} A_{\text{NO}} &= A_{\text{seg}\cup\text{sim}} - A_{\text{seg}\cap\text{sim}} \\ &= A_{\text{seg}} + A_{\text{sim}} - 2 \cdot A_{\text{seg}\cap\text{sim}}. \end{aligned} \tag{3.10}$$

Here, A_{seg} is the cross-sectional area obtained from the systolic 4DUS segmentation, A_{sim} is the cross-sectional area at the same location computed from simulations at peak systole for a particular value of tissue support k. Meanwhile, $A_{\text{seg}\cup\text{sim}}$ and $A_{\text{seg}\cap\text{sim}}$ are the areas of the union and intersection of these two cross-sections respectively. Based on the definition, the non-overlapping area is indicative of how closely the simulation results capture not only the arterial expansions/contractions but also vessel translation. Figure 3.8 shows the variation of the effective diameter and non-overlapping area for different values of tissue support k. Data on the other two cross-sectionsis reported in Section 3.4.2.

For the Day 0 time point, the variations in effective diameter and non-overlapping area are observed in a narrow range of k values. This was consistent with observations from Figure 3.7, where cross-section profiles from simulations were found to be coincident with the highest or lowest tissue support curves except for a small, identical range of $k = 10^6 - 10^7$ dyne/cm^3. Based on this data obtained for the Day 0 time point, an optimum range of values of k was chosen to be $k = 10^6 - 10^7$ dyne/cm^3. As seen from plots in Figure 3.8b and c, the effective diameter obtained from segmentations corresponds to this range of k values and the non-overlapping area is also the least amongst all simulated cases with varying tissue support parameter. For the diseased aorta at Day 28, it was observed that the same range of tissue support values from the Day 0 time point $k = 10^6 - 10^7$ dyne/cm^3 was the optimum range (see

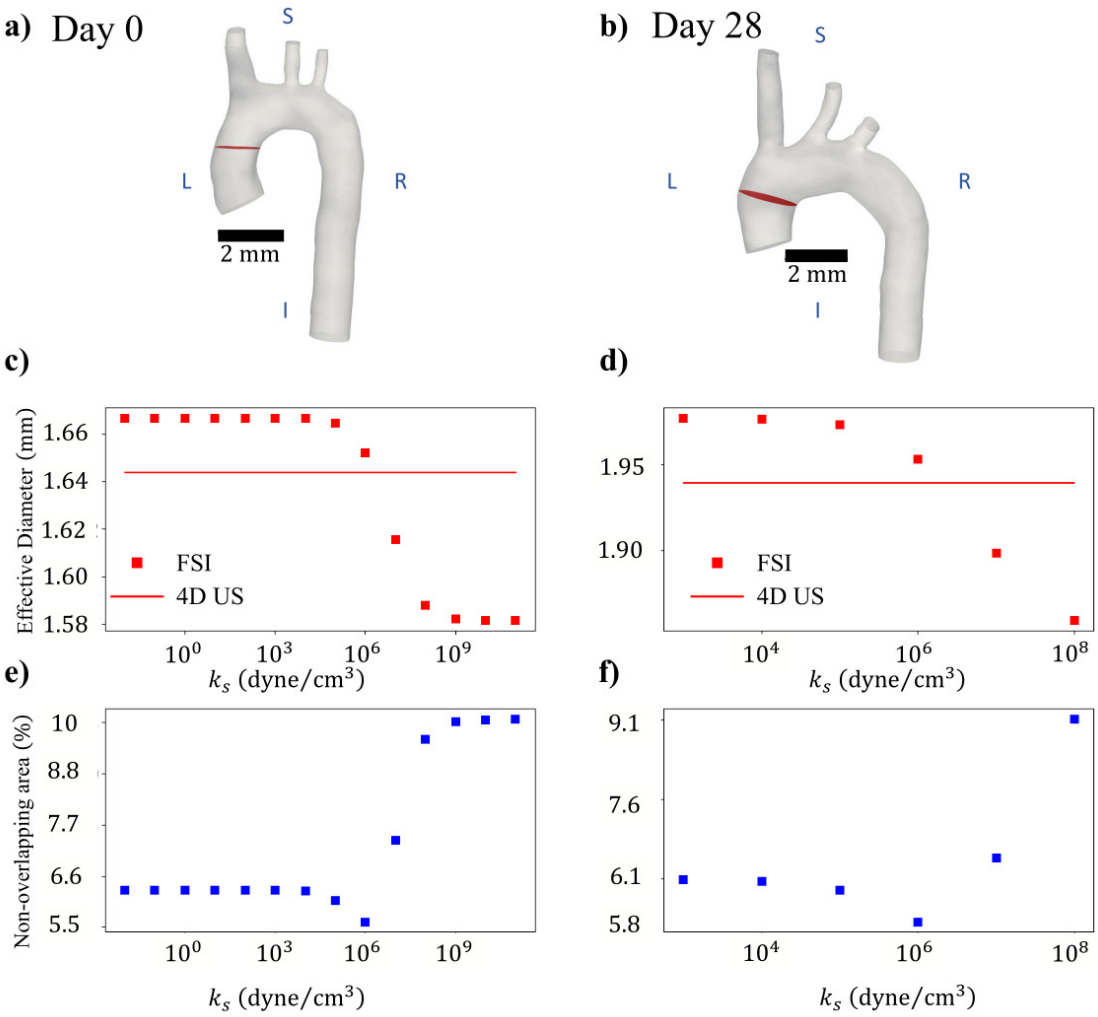

Figure 3.8. Quantitative metrics comparing segmentations from 4DUS and FSI simulations for different values of k at peak systole. a) and b) show the location of the cross-section being considered, which is the same as in Figures 3.7a and b. Red squares in c) and d) show the plot of effective diameter of the cross-section, obtained from FSI simulations (calculated using Equation (3.9)) as a function of tissue support parameter k. The solid red line represents the effective diameter of the same cross-section obtained from segmentations of 4D US imaging data. e) and f) show the variation of non-overlapping area at the cross-section, calculated using Equation (3.10) as a function of the varying tissue support parameter k.

Figure 3.8e and f). This indicates that the tissue support parameter may be kept identical between healthy and diseased states provided that differences in arterial stiffness between the healthy and diseased state have been accounted for. As noted previously, strain in the

ascending thoracic aorta substantially decreased while the pulmonary artery remained the same suggesting that AngII has a larger effect on the higher pressure in systemic circulation.

3.4.2 Comparison of Other Cross-Sections

Plots of effective diameter and non-overlapping area (see Section 3.4.1) at the other two cross-sections for the Day 0 and Day 28 time points (Figures 3.9 and 3.10) are shown below. Overall, these observations are consistent with data obtained for the cross-section reported in Section 3.4.1.

3.4.3 Deformation Profiles Using HGO Model

In order to determine the effect of using a different constitutive model, separate simulations were performed for the Day 0 geometry using the Holzapfel-Gasser-Ogden (HGO) hyperelastic constitutive model [65]. The strain energy density function for this model is:

$$\psi_{\text{HGO}} = p(J-1) + \frac{E}{6}(\tilde{I}_1 - 3) + \frac{k_1}{2k_2}\sum_{i=4,6} \exp\left[k_2(\tilde{I}_i - 1)^2\right] - 1. \tag{3.11}$$

Here, the respective invariants are defined as $\tilde{I}_1 = \text{tr}\,\tilde{\mathbf{C}}$, $\tilde{I}_4 = \tilde{\mathbf{C}} : \mathbf{A}_1$, $\tilde{I}_6 = \tilde{\mathbf{C}} : \mathbf{A}_2$, $\mathbf{A}_1 = a_{01} \bigotimes a_{01}$, $\mathbf{A}_2 = a_{02} \bigotimes a_{02}$ and $\tilde{\mathbf{C}} = J^{-2/3}\mathbf{C}$. The definitions of $\mathbf{C}$, p, J and E are the same as in Equation (2.3a).

As seen from Equation (3.11), in addition to the energy contribution due to an incompressible hyper-elastic ground matrix, the model assumes contribution due to two families of collagen fibers, oriented along directions a_{01} and a_{02}. In this case, the collagen fiber families were assumed to be perpendicular to each other, oriented along the axial and circumferential directions of the vessel i.e. $a_{01} \cdot a_{02} = 0$. Incorporating this simplification into the strain energy density function and using the same procedure as in Section 3.3.2, the Cauchy stress tensor was obtained as a function of the circumferential stretch via a symbolic computations performed with a MATLAB script (see Appendix A). Figure 3.11e shows the fit for the circumferential stress-stretch data from Bellini *et al.* [61]. The associated fit values are: $E = 3 \times 10^6 \text{dyne/cm}^2, k_1 = 1.85 \times 10^3 \text{dyne/cm}^2, k_2 = 0.046$ and $p = 80.24 \times 10^3 \text{dyne/cm}^2$.

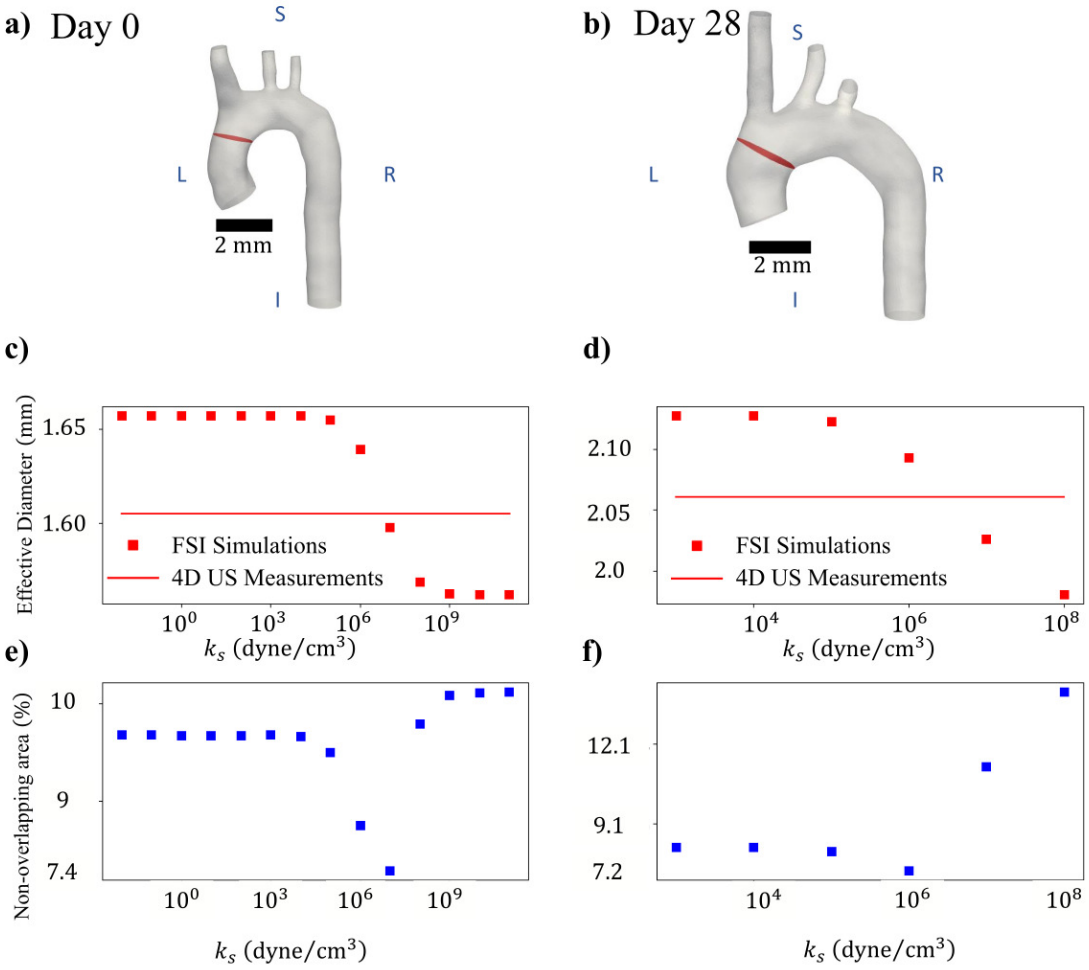

Figure 3.9. Quantitative metrics comparing segmentations from 4DUS and FSI simulations for different values of k at peak systole. a) and b) show the location of the cross-section being considered. Red squares in c) and d) show the plot of effective diameter of the cross-section, obtained from FSI simulations (calculated using Equation (3.9)) as a function of tissue support parameter k. The solid red line represents the effective diameter of the same cross-section obtained from segmentations of 4D US imaging data. e) and f) show the variation of non-overlapping area at the cross-section, calculated using Equation (3.10) as a function of the varying tissue support parameter k.

Subsequently, FSI simulations for the same range of k_s values i.e. ($k_s = 10^{-2}$ to 10^7 dyne/cm^3) were run using the HGO model and above fit parameters. Cross-sections at the three planes considered in Section 3.4.1 and 3.4.2 were then compared for the HGO model and the original neo-Hookean model for identical values of k_s.

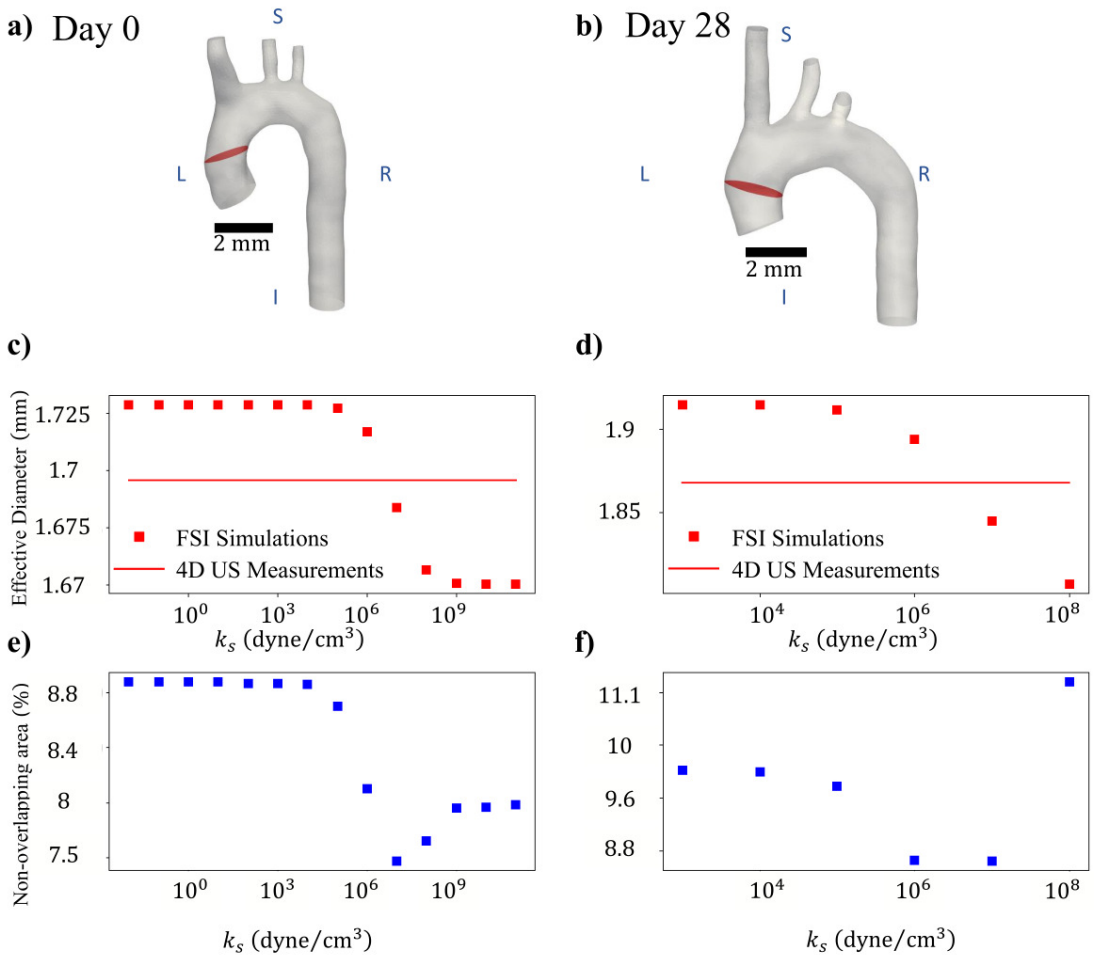

Figure 3.10. Quantitative metrics comparing segmentations from 4DUS and FSI simulations for different values of k at peak systole. a) and b) show the location of the cross-section being considered. Red squares in c) and d) show the plot of effective diameter of the cross-section, obtained from FSI simulations (calculated using Equation (3.9)) as a function of tissue support parameter k. The solid red line represents the effective diameter of the same cross-section obtained from segmentations of 4D US imaging data. e) and f) show the variation of non-overlapping area at the cross-section, calculated using Equation (3.10) as a function of the varying tissue support parameter k.

Figures 3.11b), c) and d) show the comparison for the cross-sectional plane in Figures 3.7 and 3.8. the comparisons for other cross-sectional planes, though not shown for brevity, show similar trends. As seen from the comparisons, there is practically no difference between the deformation profiles obtained using the HGO and neo-Hookean model. However, for some

values of k_s, the HGO model simulations approximately took twice as much time to complete four cardiac cycles as compared to the neo-Hookean model.

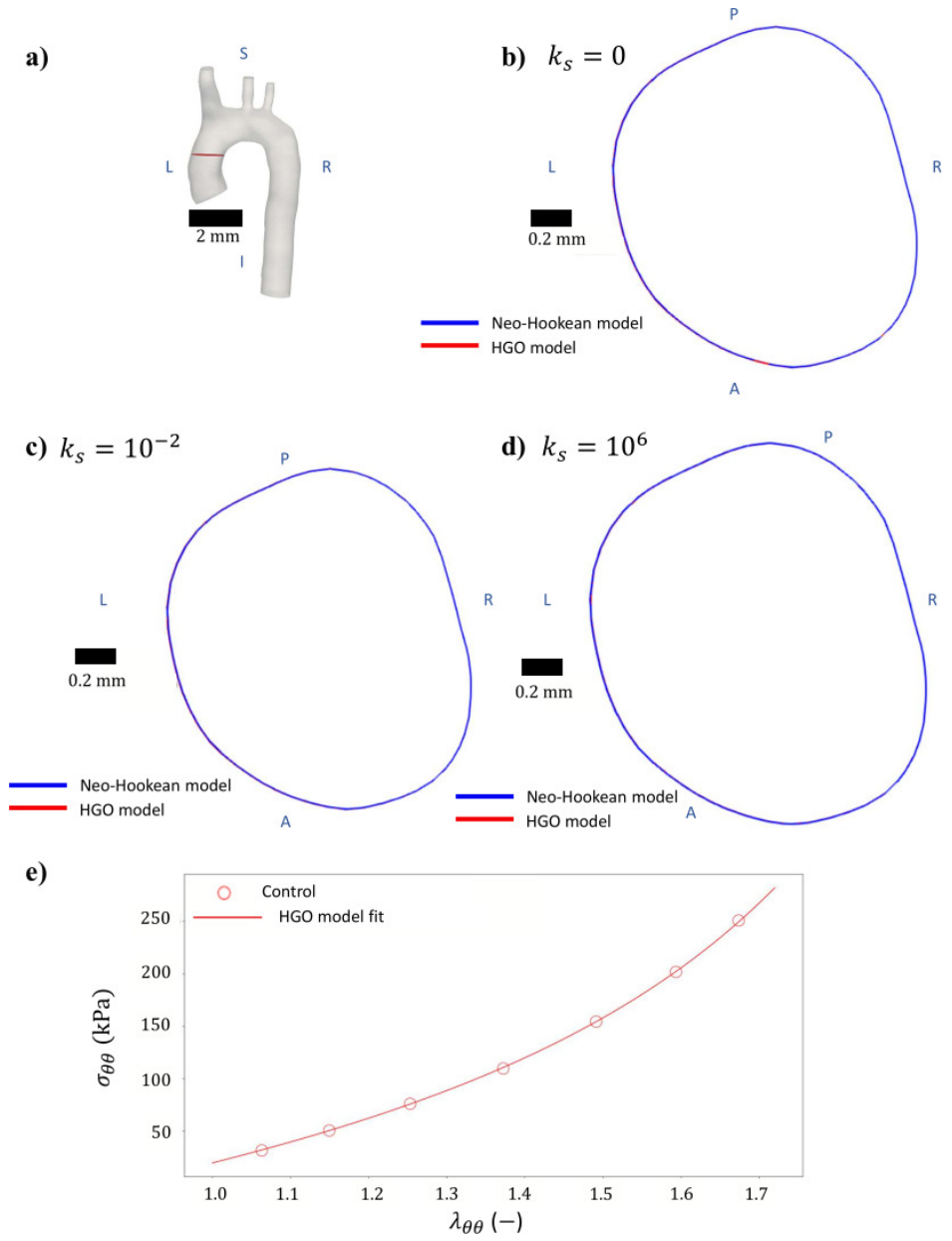

Figure 3.11. Visual comparison of FSI simulation data at peak systole using the neo-Hookean and HGO model for the Day 0. a) shows the locations of the cross-section being considered at Day 0. b), c) and d) show the cross-sections (colored rings) obtained for various values of tissue support parameter k (in dyne/cm^3). e) shows experimental circumferential stress vs. stretch-squared data from Bellini *et al.* [61] along with the best fit curve for the HGO model (Equation (3.11)).

3.4.4 Limitations

The study had several limitations related to both image acquisition and computational assumptions. While 4DUS is an accessible option for studies in mice, the clinical translation is currently limited. Petterson *et al.* [66] have taken a step toward this implementation with a recent study using multi-perspective ultrasound to mechanically characterize the aorta. Until 4DUS becomes more widely available, the presented FSI approach would work with other time-resolved imaging methods such as cardiac-gated computed tomography or magnetic resonance, although these methods typically have much lower temporal resolution.

Additionally, limitations arise when using murine TAA models, as the hemodynamic characteristics are clearly different between mice and humans. Nevertheless, the blood velocities, systemic pressure, and cyclic strain are similar across mammals. Further, the ability to collect multiple time points and tissue for analysis, allowed for comparison of simulation results for Day 0 with the Day 28 simulation using the same external tissue supports. In terms of the simulation approach, the present analysis assumed uniform material properties (values of E and ν) throughout entire arterial wall region being modeled. Furthermore, an isotropic hyperelastic constitutive model was chosen. In reality, arterial wall properties are not only animal-specific, but also highly anisotropic, as shown in this recent work [67]. However, in the absence of any animal specific measurements on mechanical properties of the aortic wall, a simplifying assumption that the arterial wall material properties were isotropic, constant and could be extracted from available literature data was made in the analysis.

In this analysis, the out-of-plane deformations of the aortic root are neglected owing to limitations of svFSI associated with imposing a parabolic flow inlet profile. In reality, some amount of longitudinal displacement is expected due to the motion of the aortic root. As seen from the study by Moireau *et al.* [27], as well as a recent computational study of thoracic aortic aneurysms in human subjects [68], this motion is found to be more important in the healthy state as compared to the diseased state. However, allowing for in-plane deformations enables accounting for some if not the entire motion of the aortic root.

In order to reduce the number of tissue support parameters, the effect of the damping co-efficient was neglected. Except for the spine and pulmonary artery regions, which are rigid

contacts, a spatiotemporally uniform value of k was assumed over the remaining surface of the outer wall. However, as seen in cross-sectional comparisons from Figure 3.7, parts of the curve segmented from 4DUS data matched better using different values of the tissue support parameter k. Moreover, the response of the surrounding tissue is generally expected to be anisotropic, non-linear and dependent on the stage in the cardiac cycle. This is particularly important for vessels close to the heart, that can be affected by motion of the lungs during regular respiration. While accounting for these limitations is out of the scope of the present analysis, the analysis demonstrated the effect of incorporating some tissue support parameters and obtained an optimum range for these tissue support parameters. Accounting for heterogeneity in these values (by accurately considering the various types of contacts and supports) would further improve the fidelity of computational models.

4. SPECIFIC AIM 3: COMPARATIVE BIOMECHANICAL ANALYSIS OF SUBJECTS WITH MULTIPLE CEREBRAL ANEURYSMS

The material presented in this chapter is under review for publication in the *Journal of Biomechanical Engineering* under the title "Comparative Assessment of Biomechanical Parameters in Subjects with Multiple Cerebral Aneurysms using Fluid-Structure Interaction Simulations"
Authors: Tanmay C. Shidhore, Aaron A. Cohen-Gadol, Vitaliy L. Rayz, Ivan C. Christov
Tanmay C. Shidhore performed the image segmentations, geometry pre-processing, setting up and running the fluid-structure interaction simulations and data post processing. Aaron A. Cohen-Gadol graciously shared anonymized medical imaging data acquired by his team. All authors contributed to writing and reviewing the manuscript.

4.1 Background

There has been increased interest in subject-specific computational modeling of blood flow in cerebral aneurysms to augment medical imaging data with high-resolution hemodynamic information that could be used to assess the risk of aneurysm rupture and, eventually, provide clinicians with better rupture risk stratification tools. While quantifying the hemodynamic forces acting on the vessel wall endothelium through flow-only computational fluid dynamics (CFD) simulations can elucidate their effect on aneurysm progression, the assessment of aneurysm stability is incomplete without analyzing the wall deformation and the mechanical stresses within the vessel wall. Most modeling studies do not involve fluid-structure interaction (FSI) simulations, as standard-of-care imaging data lacks resolution to reliably detect subject-specific wall thickness and composition.

Nevertheless, previous computational studies have highlighted the importance of accounting for this flow-vessel wall interaction. Torii *et al.* [19] demonstrated a reduction in maxi-

mum wall shear stress (WSS) in areas of flow impingement in the aneurysm by comparing WSS predictions from rigid-wall simulations against those from FSI simulations. Takizawa *et al.* [69] also compared WSS, oscillatory shear index (OSI), and arterial stress and stretch, computed from three-dimensional (3D) FSI simulations of ten subject-specific geometries, to their rigid wall counterparts at mean arterial pressure conditions. Specifically, Takizawa *et al.* [69] found an overestimation of WSS and qualitative differences in OSI computed from the rigid-wall and FSI simulations. However, the correlations obtained between hemodynamic and biomechanical factors and disease were for single aneurysms across different subjects, where growth and stability could be explained by other clinical risk factors.

Previous studies that accounted for FSIs did not have longitudinal subject data and, moreover, did not analyze subjects with multiple aneurysms. Therefore, in the present study, a key knowledge gap in the literature was addressed by considering subjects with multiple aneurysms with one aneurysm demonstrating growth during subsequent follow up imaging. It was hypothesized that clinical risk factors for aneurysm progression (genetic predisposition, smoking status, family history, etc) would affect all aneurysms in the same subject equally. Therefore, comparing biomechanical parameters between stable and growing aneurysms in the same subject allows for controlling for these subject-specific confounding factors and reveal the influence of local flow and mechanics on aneurysm progression, and eventually rupture.

4.2 Anatomical and Computational Modeling

4.2.1 Subject Data

Under a protocol approved by an Institutional Review Board, retrospective CT angiography images for two subjects, each with two unruptured cerebral aneurysms were obtained from the Indiana University School of Medicine. Images were available at baseline and at one year post baseline (hereafter referred to as 'follow-up'). Subject 1 (hereafter referred to as 'S1') presented with a fusiform aneurysm of the right internal carotid artery, which was stable (labeled 'S1A1') and a fusiform aneurysm of the left middle cerebral artery, which grew in size between baseline and follow-up imaging (labeled as 'S1A2'). Similarly, subject

2 (hereafter referred to as 'S2') presented with two saccular aneurysm, one of the proximal right posterior communicating artery that remained stable (labeled as 'S2A1') and one on the left superior cerebellar artery, which grew (labeled as 'S2A2'). Figure 4.1(a)-(d) shows the solid baseline geometries, along with the superposed transparent follow up model, visually demonstrating the extent of growth. Table 4.1 reports the subject characteristics, along with the percentage of increase in volume for the growing aneurysms between baseline and follow-up studies.

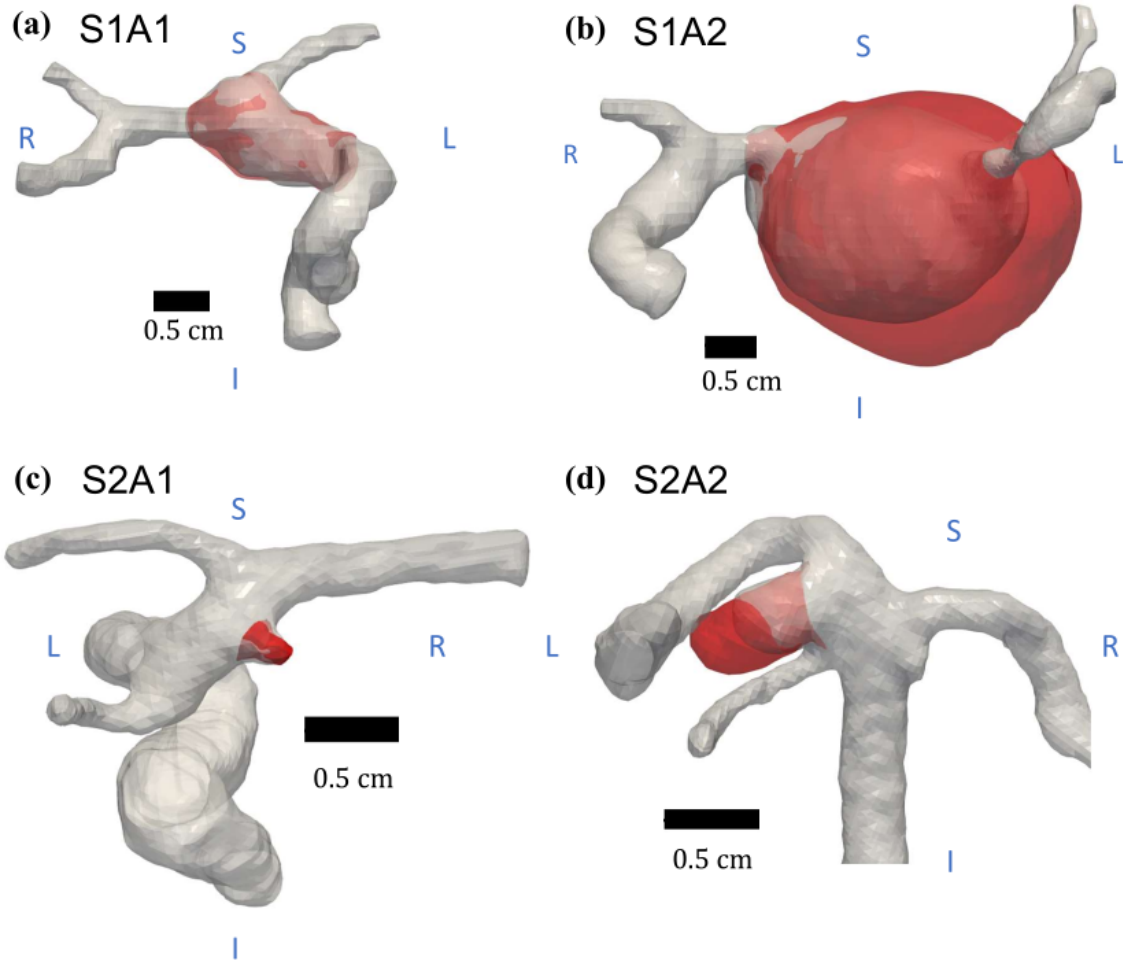

Figure 4.1. (a)-(d): Subject-specific baseline (solid) and follow-up (transparent) geometries of stable and growing aneurysms. Abbreviations used – R: Right, L: Left, S: Superior, I: Inferior.

Table 4.1. Subject and aneurysm characteristics.

Subject	Age, Sex	Growing Aneurysm			Stable Aneurysm	
		Location	Initial diam. (mm)	Volumetric growth (%)	Location	Initial diam. (mm)
S1	62, Male	L MCA	22	65	R ICA	9
S2	67, Female	L SCA	5	10.5	R PCommA	3

Abbreviations used – R: Right, L: Left, MCA: middle cerebral artery inferior bifurcation, ICA: internal carotid artery, PCommA: posterior communicating artery, SCA: superior cerebellar artery.

4.2.2 Computational Geometries

Flow Domain Geometry

The fluid flow geometry for each aneurysm was obtained from CT angiographic images for each aneurysm using the procedure described in Section 2.1.

Wall Thickness Estimation and Solid Domain Geometry

Accounting for variation in arterial wall thickness is crucial to obtaining physiologically realistic FSI simulation results [7], [10]. In particular, Voß *et al.* [8] found differences in wall shear stress distribution between FSI simulations conducted with constant and subject-specific wall thickness values. In the present study, the available CT angiography data lacks resolution to obtain reliable information on the vessel wall. Therefore, a novel workflow to estimate the nonuniform wall thickness, accounting for the effect of heterogeneous distribution of hemodynamic forces on the vessel wall was implemented. The nonuniform baseline arterial wall thickness $t(\mathbf{x})$ was first estimated using the procedure in Section 3.2.3. Here, boundary conditions were prescribed on the sets of curves forming the inlets and outlets of the computational geometry. Specifically, a value corresponding to 10% of the respective effective inlet/outlet diameter was imposed.

Additionally, the formulation proposed by Cebral *et al.* [7] was used to modulate $t(\mathbf{x})$ over the aneurysm using time-averaged wall shear stress data obtained from a rigid-wall pulsatile flow simulation. However, unlike [7], where the modulation was determined based on the

absolute time-averaged wall shear stress, the normalized time-averaged wall-shear stress $\tilde{\tau}^*$ given by

$$\tilde{\tau}^*(\mathbf{x}) = \frac{\tilde{\tau}(\mathbf{x})}{\tilde{\tau}_{\max}} \tag{4.1}$$

was used. Here, $\tilde{\tau}(\mathbf{x})$ is the time-averaged wall shear stress magnitude at a given location $\mathbf{x}$ on the aneurysmal surface and $\tilde{\tau}_{\max}$ is the spatial maximum time-averaged wall shear stress magnitude over the aneurysm, both of which, as mentioned earlier, were obtained via pulsatile rigid-wall flow simulations.

Furthermore, a different (as compared to [7]) modulation function was considered:

$$m(\mathbf{x}) = \begin{cases} 1.5\tilde{\tau}^* - 0.3, & \tilde{\tau}^*(\mathbf{x}) < 0.2, \\ 1.5\tilde{\tau}^* - 1.2, & \tilde{\tau}^*(\mathbf{x}) > 0.8, \\ 0, & \text{otherwise.} \end{cases} \tag{4.2}$$

Based on this definition of $m(\mathbf{x})$, it can be seen that regions of low and high wall shear stress (i.e. for which $\tilde{\tau}^* < 0.2$ and $\tilde{\tau}^* > 0.8$) are thickened or thinned up to a maximum of 30% of the baseline value [7]. Meanwhile, regions of moderate wall shear stress (i.e. for which $0.8 \geq \tilde{\tau}^* \geq 0.2$) are left unchanged. The final wall thickness $t_{\text{final}}(\mathbf{x})$ is calculated as:

$$t_{\text{final}}(\mathbf{x}) = \Big[1 - m(\mathbf{x})\Big] t(\mathbf{x}). \tag{4.3}$$

Figure 4.2(b)-(d) shows plots of $m(\mathbf{x})$ along with an example of the above modulation function and the final wall thickness for aneurysm S1A2. It should be emphasized that the actual subject-specific wall thickness of each aneurysm is not given by Equation (4.3). Nevertheless, the proposed methodology ensured that a physiologically realistic wall thickness estimate, accounting for the local effects of aneurysmal wall shear, was used in the subsequent FSI simulations.

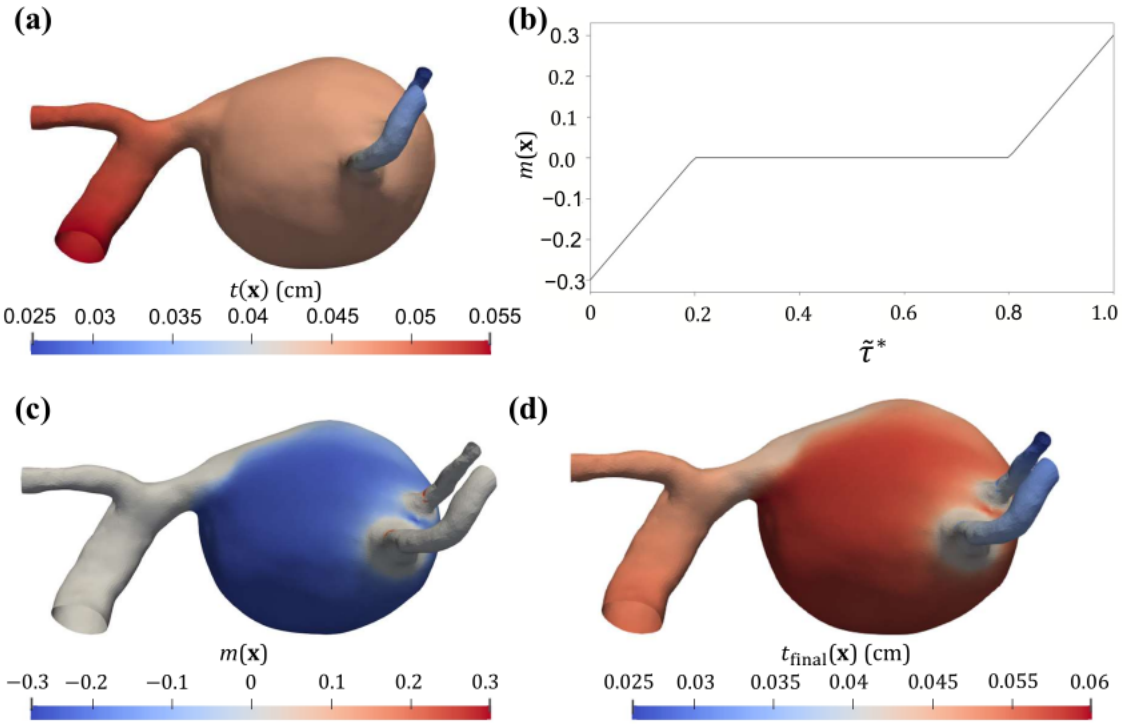

Figure 4.2. Methodology to estimate nonuniform arterial wall thickness from subject-specific aneurysm geometry. (a) Baseline nonuniform wall thickness $t(\mathbf{x})$ estimated using Equation (3.1). (b) Graphical representation of the modulation function $m(\mathbf{x})$ from Equation (4.2) as a function of the normalized time-averaged wall shear stress $\tilde{\tau}^*$ from Equation (4.1). (c) Wall thickness modulation as implemented for aneurysm S1A2 (see Figure 4.1(b)). (d) Final nonuniform wall thickness $t_{\text{final}}(\mathbf{x})$ for aneurysm S1A2 obtained using Equation (4.3).

Mesh Generation

An unstructured mesh with tetrahedral elements was generated using ANSYS® Workbench using the procedure described in Section 2.4. A mesh resolution of 0.03 cm was chosen for the fluid and, therefore, the solid domain. To ensure the accuracy of shear stress computations, the local mesh was refined near the fluid-solid interface in the flow domain up to a constant thickness of 0.03 cm. A grid independence analysis was performed on one of the aneurysm geometries to ensure that the computational results were independent of the core and near-wall mesh refinement resolutions (see Section 4.2.2 for further details).

Grid-Independence Study

To ensure that computational quantities reported, such as pressure, velocity, wall shear stress and those derived thereof, were independent of the grid resolution used in the simulations, a grid sensitivity analysis for the fluid domain's mesh was performed. The types of meshes, properties and refinement levels used are reported in Table 4.2. A two step approach was used to establish grid independence of the simulations. First, a core mesh resolution was determined for which the pressure and velocity averaged over the inlet face, as well as at a point in the interior of the parent vessel (see Figure 4.3(a)), were independent of this core mesh's resolution. Second, varying degrees of mesh refinement were implemented via boundary layers close to the fluid-solid interface, on top of the chosen core mesh resolution from the previous step. This second step ensured that the computed wall shear stress was independent of the near-wall mesh resolution.

Figure 4.3 shows the chosen representative pressure and velocity magnitude plotted over a single cardiac cycle. From these plots, it can be observed that the pressure and velocity values computed on the mesh with $\Delta x = 0.03$ cm lie within a 5% of the values computed on the most refined mesh ($\Delta x = 0.025$ cm). Therefore, a core mesh resolution of $\Delta x = 0.03$ cm was chosen as the optimal core mesh resolution for simulations.

Table 4.2. Details of meshes used for the grid-independence study.

Δx_{core} (cm)	N_{BL}	N_{elements}	N_{nodes}	Max. CFL
0.04		169,370	32,743	0.59
0.03	0	396,208	73,797	0.6
	3	400,225	74,673	4.7
	4	400,565	74,820	4.48
	5	401,517	75,076	4.61
0.025		681,305	124,604	0.88

Based on the plots in Figure 4.3, it was observed that the pressure and velocity magnitude values computed on both the coarse and medium meshes (i.e. those with $\Delta x = 0.04$ cm and $\Delta x = 0.03$ cm) lie within a 5% margin of the values computed on the fine grid. However,

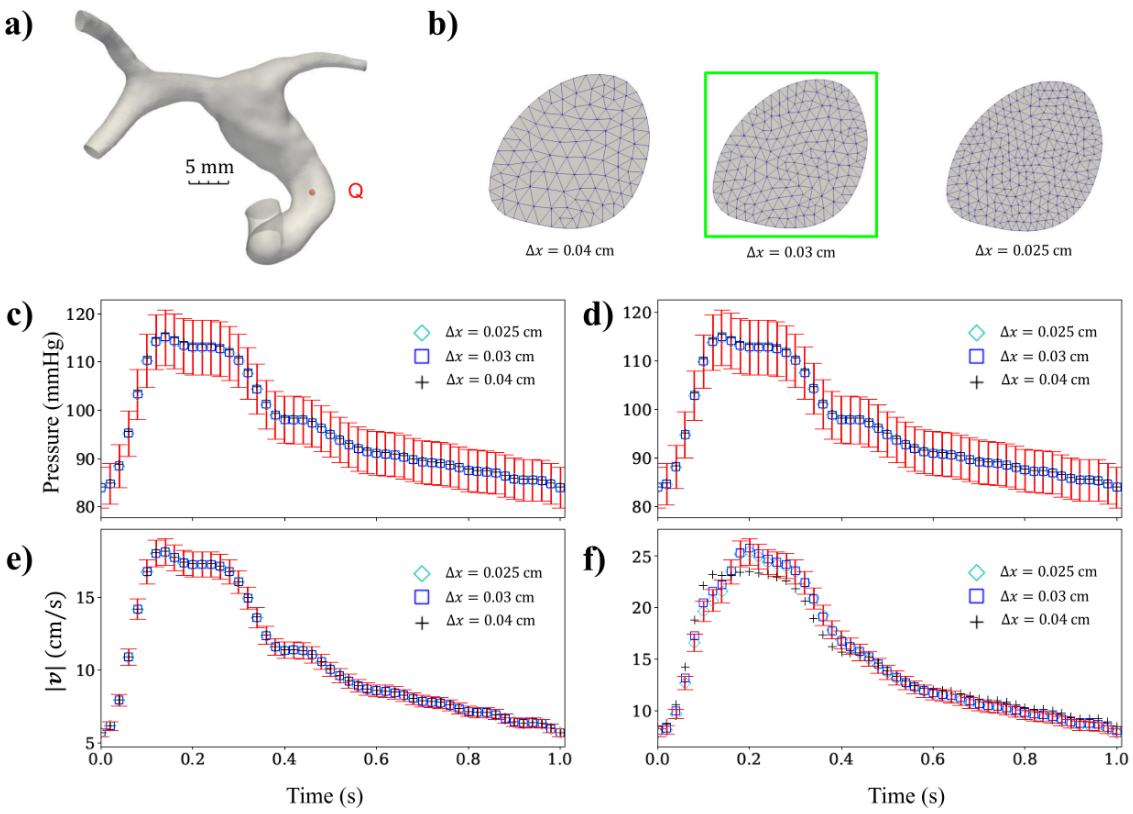

Figure 4.3. Pressure and velocity data over a cardiac cycle at the inlet plane (panels (c) and (e)) and at a point (panels (d) and (f)) in the interior of the feeding vessel (shown in (a)) for different mesh resolutions (shown in (b)). The error bars of each plot point show a deviation of 5% from the corresponding value on the finest mesh ($\Delta x = 0.025$ cm). Abbreviations used – $|\mathbf{v}|$: Velocity magnitude

in Figure 4.3f, the velocity magnitude for the coarse grid ($\Delta x = 0.04$ cm) lies beyond this tolerance margin. Therefore, $\Delta x = 0.03$ cm was determined to be the core mesh resolution of choice.

Next, Figure 4.4 shows the x, y, and z components of the WSS (wall shear stress) computed at a point on the surface of the ascending aorta. Here, the core mesh resolution was identical in all cases ($\Delta x = 0.03$ cm). However, close to the fluid-solid interface, different number of layers of mesh refinement (0, 3, 4, and 5) were considered (see Figure 4.3(a)). From Figure 4.4(b)-(d), a nontrivial difference ($> 5\%$) was observed between the surface shear stress values computed on meshes with and without mesh refinement. Furthermore, meshes with different levels of mesh refinement ($N_{\mathrm{BL}} = 3, 4$, and 5) yield shear stress values

within the above tolerance limit with minor differences in the computational time. Therefore, a mesh refinement level of $N_{\mathrm{BL}} = 4$,was chosen to balance the need for increased resolution with the corresponding computational cost.

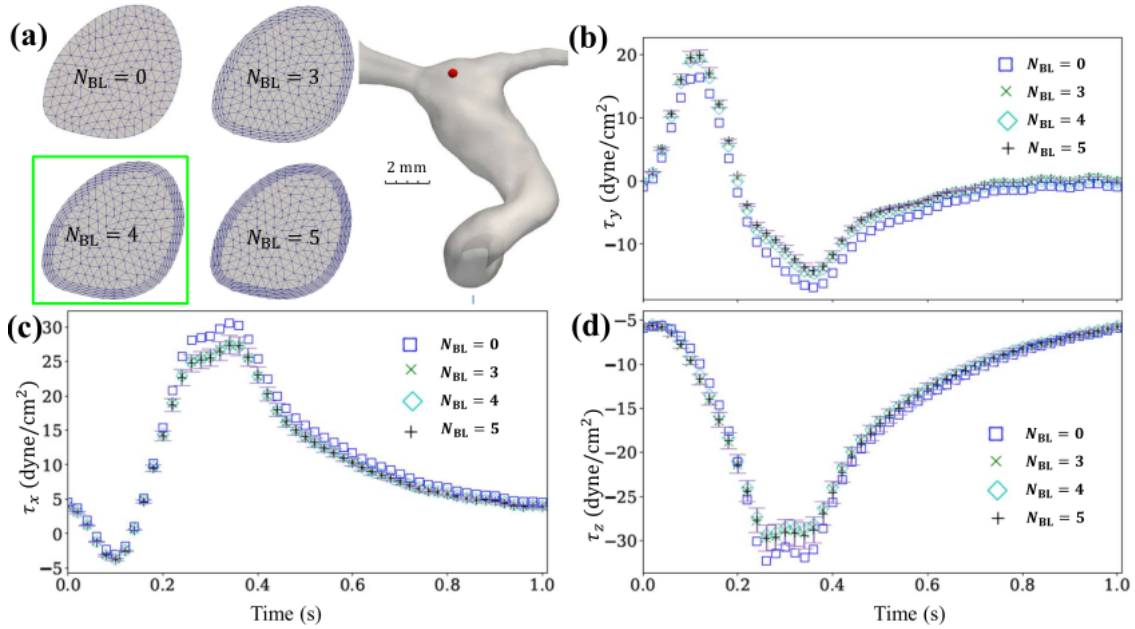

Figure 4.4. Components (shown in panels (b), (c) and (d)) of the WSS τ over a cardiac cycle at a point on the aneurysmal surface (shown by a dot in the model geometry in (a)), for different number of boundary layers each. N_{BL} represents the number of layers of boundary layer elements. Here, $N_{\mathrm{BL}} = 0$ represents a mesh without boundary layer refinement. The error bars on each plot point show a deviation of 5% from the corresponding value on the mesh with the largest number of boundary layer refinements (i.e. $N_{\mathrm{BL}} = 5$).

A constant time step of $\Delta t = 10^{-4}$ s was used for all cases. Table 4.2 reports an estimate of the maximum cell-based Courant number computed for each of the meshes used, over a single cardiac cycle. The cell-based Courant number is defined as: $\mathrm{CFL} = |\mathbf{v}|\Delta t/\Delta x$, where $|\mathbf{v}|$ is the velocity magnitude at the cell center, Δt is the time step size, and Δx is a length scale computed for each cell as $\Delta x = \mathcal{V}^{1/3}$, where $\mathcal{V}$ is the cell volume.

It was observed that only a few elements ($< 1\%$ of the total number of elements) that were close to the outlet faces exceeded the threshold of having a maximum CFL > 1. This observation, together with the fact that the time-integration scheme implemented in svFSI

is implicit [24], allowed for using the same time step size of $\Delta t = 10^{-4}$ sec for the subsequent FSI simulations as well.

4.3 Governing Equations and Numerical Framework

Three-dimensional numerical simulations were performed using the svFSI solver, as described in Section 2.3.

4.3.1 Fluid Domain

Blood was assumed to be a Newtonian fluid. This modeling assumption is commonly used in the medium-sized arteries, such as those in the Circle of Willis [70]. Furthermore, the flow of blood was modelled as an incompressible flow. Identical blood density and viscosity values ($\rho_f = 1.06$ g/cm^3, $\mu_f = 4$ cP) were used for all subjects' simulations. These values were taken from previous literature [28].

4.3.2 Structural Domain

As mentioned in Section 2.3.1, the arterial wall was modelled as nearly incompressible hyperelastic material with material properties $E = 10^7$ dyne/cm^2 and $\nu = 0.49$. These values were obtained from previous literature [19].

4.3.3 Tissue Pre-Stress

Arterial pre-stress was computed as described in Section 2.3.6. In this study, the flow traction data was obtained for each aneurysm geometry via separate pulsatile rigid-walled flow simulations. Using these simulations as an input, the pre-stress tensor $\mathbf{S}_0$ (see Equation (2.35)) was estimated for all aneurysmal geometries and prescribed as an initial stress state in subsequent FSI simulations. Here, $\mathbf{S}_0$ is defined such that it is in equilibrium with the incoming blood flow's tractions at cardiac-cycle averaged conditions.

4.3.4 Boundary Conditions

Fluid Domain Boundary Conditions

A pulsatile flow profile acquired from MR (magnetic resonance) measurements in the middle cerebral artery of a healthy volunteer was prescribed at the inlet, as shown in Figure 4.5(a). However, to account for differences in the feeding artery in each aneurysmal geometry, this flow profile was scaled such that the centerline velocity at peak systole matched previously reported population-averaged PC-MRI (phase contrast magnetic resonance imaging) measurements [71]. As in Section 3.3.4, the Womersley number (see Equation (2.30)), was estimated based on the radius of the parent/feeding vessel R and the cardiac frequency f (beats per second). As the Wo values for all aneurysm geometries were found to be between 2 and 4, a parabolic (Poiseuille) flow profile was implemented at the inlet cross-section.

To model the effect of the downstream vasculature, a three-element RCR (or, 'Windkessel') boundary condition was imposed at each of the outlets [62].

The process for tuning the distal pressure, total resistance, and capacitance was the same as reported in Section 3.3.4. In the present case, RCR parameters were tuned such that both diastolic, P_d, and pulse, $P_s - P_d$, pressures were within 10% of the corresponding normal values (i.e. 80 mmHg and 40 mmHg, respectively). Rigid-wall pulsatile flow simulations were run for six cardiac cycles, and the results from the fourth cardiac cycle were used in the fine-tuning process. The resistance across each individual outlet was distributed using the allometric scaling law used for cerebral vessels [35]. That is, instead of using a coefficient of $m = 3$, the value $m = 2.4$ was used in Equation (3.5). For each outlet branch, the ratio of the distal to proximal resistance was assumed to be 1:9 [28]. Tables 4.3 and 4.4 list the RCR parameters used for each aneurysm.

Structural Domain Boundary Conditions

As mentioned in Section 2.3.5, a homogeneous Dirichlet boundary condition, $\mathbf{u} = \mathbf{0}$, was imposed at the solid caps at each flow outlet and inlet and the effect of surrounding tissue

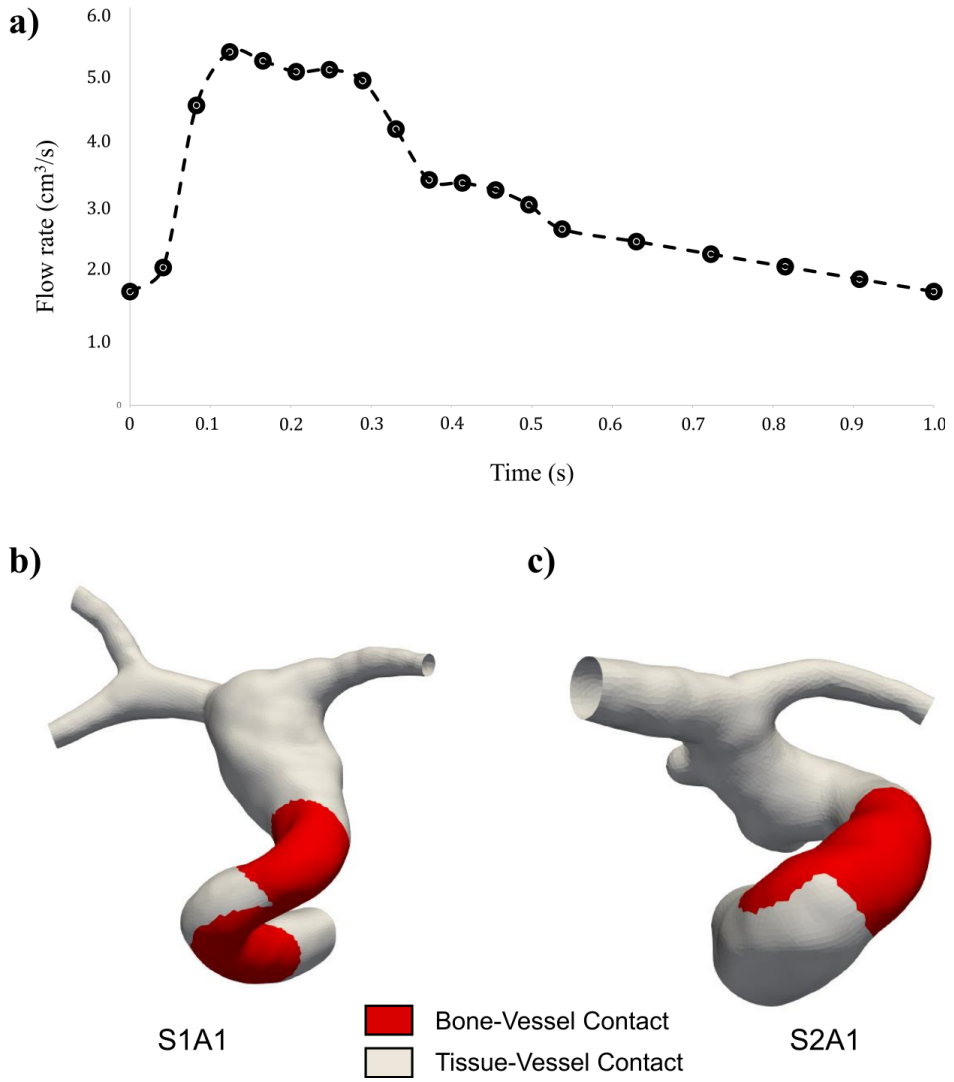

Figure 4.5. (a) Inlet pulsatile flow flow rate (in $\mathrm{cm}^3/\,\mathrm{sec}$) obtained from MR measurements in the middle cerebral artery of a healthy volunteer. Depending on the inlet vessel for each aneurysm, the flow rate values were scaled to match population-averaged centerline velocities at peak systole data from [71]. (b) and (c) Partitions on the outer vessel wall for aneurysms S1A1 and S2A1 (see Figures 4.1(a) and (c)) used to impose nonuniform spring constant values, depending on the nature of contact for the traction condition in Equation (2.33).

Table 4.3. RCR parameter values at each outlet for S1.

Aneurysm	Outlet	R_p ($\times 10^3$ dyne sec /cm^5)	R_d ($\times 10^4$ dyne sec /cm^5)	C ($\times 10^{-7}$ cm^5/dyne)	P_0 (mmHg)
S1A1	R MCA inferior	5.19	4.67	1.53	70
	R MCA superior	5.48	4.93	1.45	
	R ACA	12.6	11.4	0.63	
S1A2	L MCA inferior	3.32	2.99	11.6	70
	L MCA superior	9.27	8.34	4.14	
	L ACA	2.42	2.18	15.9	

Abbreviations used – R: Right, L: Left, MCA inferior: middle cerebral artery inferior bifurcation, MCA superior: middle cerebral artery superior bifurcation, ACA: anterior cerebral artery, R_p: proximal resistance, R_d: distal resistance C: capacitance, P_0: distal pressure.

Table 4.4. RCR parameter values at each outlet for S2.

Aneurysm	Outlet	R_p ($\times 10^3$ dyne sec /cm^5)	R_d ($\times 10^4$ dyne sec /cm^5)	C ($\times 10^{-7}$ cm^5/dyne)	P_0 (mmHg)
S2A1	R MCA	1.82	1.64	43.6	70
	R ACA	7.32	6.59	10.9	
	R PCommA	10.2	91.5	7.83	
S2A2	R PCA	6.47	5.83	12.5	70
	L PCA	6.71	60.4	12	
	L SCA	24.7	24.9	2.92	

Abbreviations used – R: Right, L: Left, MCA: middle cerebral artery inferior bifurcation, ACA: anterior cerebral artery, PCommA: posterior communicating artery, SCA: superior cerebellar artery, PCA: Posterior cerebral artery, R_p: proximal resistance, R_d: distal resistance C: capacitance, P_0 = distal pressure.

was accounted for by using the Robin (spring-dashpot) boundary condition (see Equation (2.33)).

Following the simplification made in Section 3.3.5, c and p_0 are set to 0 identically to account for only linear elastic effects. However, a spatially nonuniform spring constant k was prescribed, depending on the type of contact (i.e. bone/tissue) as shown in Figure 4.5(b) and (c). To maintain consistency, k values were kept identical for the same type of contact across both subjects. Contact between vessel and bones, which is expected to exhibit smaller deformations, was modeled by prescribing a large value ($k = 10^9$ dyne/cm^3).

For the other regions of the vessel, the tissue support parameter(s) must be calibrated by matching wall deformation data from simulations to *in vivo* imaging. Here, since the available data was in the form of static images with no information on vessel wall displacements, a scaling analysis was performed (see Section 4.3.4) to obtain the tissue support parameter

values for the human aneurysm subjects based on optimum tissue support estimates from Chapter 2. Based on the order-of-magnitude scaling analysis, a value of $k = 10^6$ dyne/cm^3 was chosen and used for simulations, the results for which are shown in Section 4.4. It should be noted that the chosen value of k was not only found to be within range of previously used values for k in literature [27], [28] but also resulted in peak systolic deformations closest to physiologically realistic aneueysmal wall deformation values, based on the expert opinion of clinical collaborators.

Scaling Analysis for Tissue Support Parameters

As discussed by Moireau *et al.* [27], the parameters k, c and p_0 in Equation (2.33) must be tuned such that simulation wall displacements match corresponding *in-vivo* measurements. However, standard-of-care imaging data such as CTA or MRI typically lacks information on wall motion. Furthermore, any *ex-vivo* experimental tissue characterization is difficult and in most cases, impossible. Therefore, a methodology was proposed to obtain an order-of-magnitude estimate of tissue support parameters, specifically the spring constant parameter k for human aneurysm models based on wall motion measurements from animal studies. It should be noted that the model used in Equation (2.33) does not directly account for the location or type of tissue but relies solely on the magnitudes of k, c and p_0 to distinguish between different types of contacts. Therefore, a scaling analysis, using the simplest mathematical model that describes flow through a blood vessel (i.e. steady flow through a cylindrical shell), should allow for development of a relationship between the order-of-magnitude of k values across different animals and different regions of the vasculature.

In the present case, data from previous work on estimating tissue support parameters for murine models of thoracic aortic aneurysms reported in Chapter 2 was used. The mathematical model considered was analogous to [72], where a cylindrical shell with thickness t, undeformed radius R, length ℓ, Young's modulus E and Poisson ratio ν was considered. The cylinder was assumed to be thin (i.e. $t/R \ll 1$) and long (i.e. $R/\ell \ll 1$) and clamped at both ends. Due to the cylinder being thin, no distinction was made between the inner and outer radii [72]. There is a steady flow of a Newtonian fluid, which results in a pressure p acting on

the inner wall of the cylinder. The outer wall is assumed to be supported by a Kelvin-Voigt material, whose response is described by Equation (2.33). To maintain consistency with the tissue support model used in the analysis, an elastic response was assumed i.e. p_0 and c were set to 0, resulting in the traction being proportional to the deformation u, which in this case, was purely radial.

Following [72], for locations far away from the clamped ends, the hoop stress $\sigma_{\theta\theta}$ and axial stress σ_{zz} could be written as follows:

$$\sigma_{\theta\theta} = \frac{(p - ku)r}{t}, \tag{4.4a}$$

$$\sigma_{zz} = \frac{pr}{2t}. \tag{4.4b}$$

Here, r is the deformed radial coordinate. Assuming an incompressible ($\nu = 1/2$), neo-Hookean constitutive model for the solid, the deformation gradient in cylindrical coordinates could be shown to be:

$$\mathbf{F} = \begin{bmatrix} \frac{R}{r} & 0 & 0 \\ 0 & \frac{r}{R} & 0 \\ 0 & 0 & 1 \end{bmatrix}. \tag{4.5}$$

and the hoop and axial stresses are related as

$$\sigma_{\theta\theta} - \sigma_{zz} = \frac{E}{3}\left(\frac{r^2}{R^2} - 1\right). \tag{4.6}$$

Substituting for $\sigma_{\theta\theta}$ and σ_{zz} from Equations (4.4) into the last equation, one can solve for the spring constant k:

$$k = \frac{t}{R}\left[\frac{p}{2t\epsilon} - \frac{E}{3R} + \frac{E}{3R\epsilon(\epsilon + 1)}\right]. \tag{4.7}$$

where $\epsilon = u/R$ is the ratio of the deformation to the undeformed radius.

Equation (4.7) may be used to relate the tissue support parameter for murine and human aneurysm models as follows:

$$\frac{k_{\mathrm{h}}}{k_{\mathrm{m}}} = \frac{\dfrac{p_{\mathrm{h}}}{2t_{\mathrm{h}}\epsilon_{\mathrm{h}}} - \dfrac{E_{\mathrm{h}}}{3R_{\mathrm{h}}} + \dfrac{E_{\mathrm{h}}}{3R_{\mathrm{h}}\epsilon_{\mathrm{h}}(\epsilon_{\mathrm{h}}+1)}}{\dfrac{p_{\mathrm{m}}}{2t_{\mathrm{m}}\epsilon_{\mathrm{m}}} - \dfrac{E_{\mathrm{m}}}{3R_{\mathrm{m}}} + \dfrac{E_{\mathrm{m}}}{3R_{\mathrm{m}}\epsilon_{\mathrm{m}}(\epsilon_{\mathrm{m}}+1)}}, \tag{4.8}$$

where subscripts "m" and "h" denote the corresponding parameters for murine and human models respectively. The corresponding calculations are shown in Table 4.5.

Table 4.5. Scaling analysis for tissue support spring parameter.

Model	P_{systole} (mmHg)	t (mm)	R (mm)	E ($\times 10^6$ dyne/cm^2)	u (mm)	$k_{\mathrm{h}}/k_{\mathrm{m}}$
Diseased murine aorta	164.5	0.148	0.76	3.3	0.14	4
Human cerebral aneurysm	120	0.5	2.5	10	0.1	

The extreme deformation case (i.e. at peak systole) was considered, where the maximum deformation for the diseased murine aorta was found to be of the order of 0.1 mm. For the human aneurysm model, the representative diameter and thickness were considered to be of the order of 5 mm and 0.5 mm, which is typical for the internal carotid artery and a thickness value roughly 10% of the average diameter [59] respectively. Based on the expert opinion of clinical collaborators, a value of 0.1 mm was prescribed as typical deflections of aneurysmal vessels. From estimates reported in Chapter 2, an optimum tissue support parameter range of $k_{\mathrm{m}} = 10^6 - 10^7$ dyne/cm^3 was obtained for both health and diseased states of the murine aorta. Therefore, in the present analysis, the lower limit of the above range i.e. $k_m = 10^6$ dyne/cm^3 was chosen, which yielded an estimate of $k_h = 10^6$ dyne/cm^3 for the human cerebral aneurysm cases. It should be noted that the above tissue support parameter value is not the subject-specific support provided *in vivo* by the surrounding tissue. In the absence of any means to estimate subject-specific tissue support parameter values, this methodology allows for obtaining the order of magnitude of the spring constant k that results in physiologically realistic models of aneurysmal deformation.

4.3.5 Initial Conditions

The solutions for the flow and structural domain were initialized as per Section 2.3.6.

4.4 Results and Discussion

FSI simulations were run for four cardiac cycles and periodicity was found to be achieved after the 2$^{\text{nd}}$ cardiac cycle. The results from the last cardiac cycle have been reported below. Panels (a)-(d) in Figures 4.6 and 4.7 show the pressure and velocity at peak systole for the stable and growing aneurysms in each subject, respectively. The corresponding Reynolds number at the inlet at peak systole are reported in Table 4.6.

4.4.1 Hemodynamic Metrics

Previous hemodynamic modeling studies have focused on wall shear stress or more specifically abnormalities in wall shear stress magnitude and changes in wall shear stress direction over the cardiac cycle (given by the oscillatory shear index) as indirect measures of assessing vascular degradation and remodeling. Therefore, in this study, the normalized time-averaged wall shear stress (referred to as TAWSS*) and the oscillatory shear index (OSI) data for each aneurysm was obtained. The oscillatory shear index (OSI) is defined as

$$\text{OSI} = \frac{1}{2}\left(1 - \frac{\left|\frac{1}{T}\int_0^T \boldsymbol{\tau}_w(\mathbf{x},t)\,dt\right|}{\frac{1}{T}\int_0^T \left|\boldsymbol{\tau}_w(\mathbf{x},t)\right|\,dt}\right), \tag{4.9}$$

where $\boldsymbol{\tau}_w(\mathbf{x},t)$ is the wall shear stress vector at a given location $\mathbf{x}$ along the wall at time instant t of the cardiac cycle. OSI is indicative of the directionality of wall shear stress. OSI values close to 0 imply that the wall shear stress vector does not change direction over the cardiac cycle, whereas values close to 0.5 indicate reversal (180° flip) in the direction of the wall shear stress vector on a time-averaged basis. Previous studies suggested a correlation between regions of high OSI, indicative of high oscillatory shear force on the aneurysmal wall, and aneurysm progression [73]. Panels (e) and (f) of Figures 4.6 and 4.7 show contours of OSI plotted on the surface of each aneurysm. As seen from the figures, in both subjects, the stable

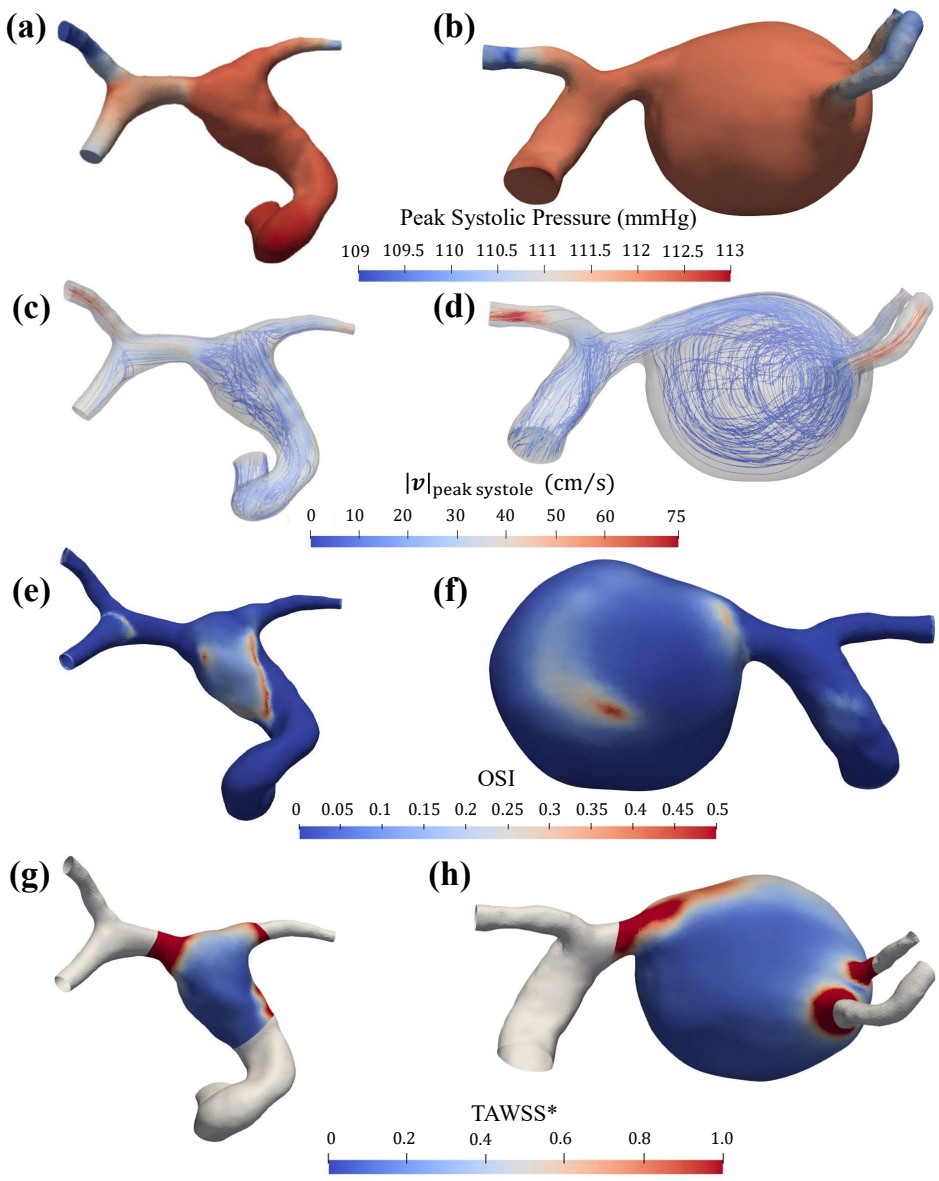

Figure 4.6. Hemodynamic metrics for subject S1. Each row shows a single metric: i.e. contours for pressure at peak systole, flow streamlines at peak systole, contours of oscillatory shear index (OSI) and normalized time-averaged wall shear stress magnitude. OSI was calculated using Equation (4.9). The time-averaged wall shear stress magnitude was normalized by the magnitude of spatiotemporal average of the wall shear stress over the feeding/parent vessel in each aneurysm, as per Equation (4.10). Panels (a), (c) (e) and (g) correspond to aneurysm S1A1, while panels (b), (d), (f) and (h) correspond to aneurysm S1A2. Abbreviations used – $|\mathbf{v}|$: Velocity magnitude, OSI: Oscillatory Shear Index, TAWSS*: Normalized time-averaged wall shear stress magnitude.

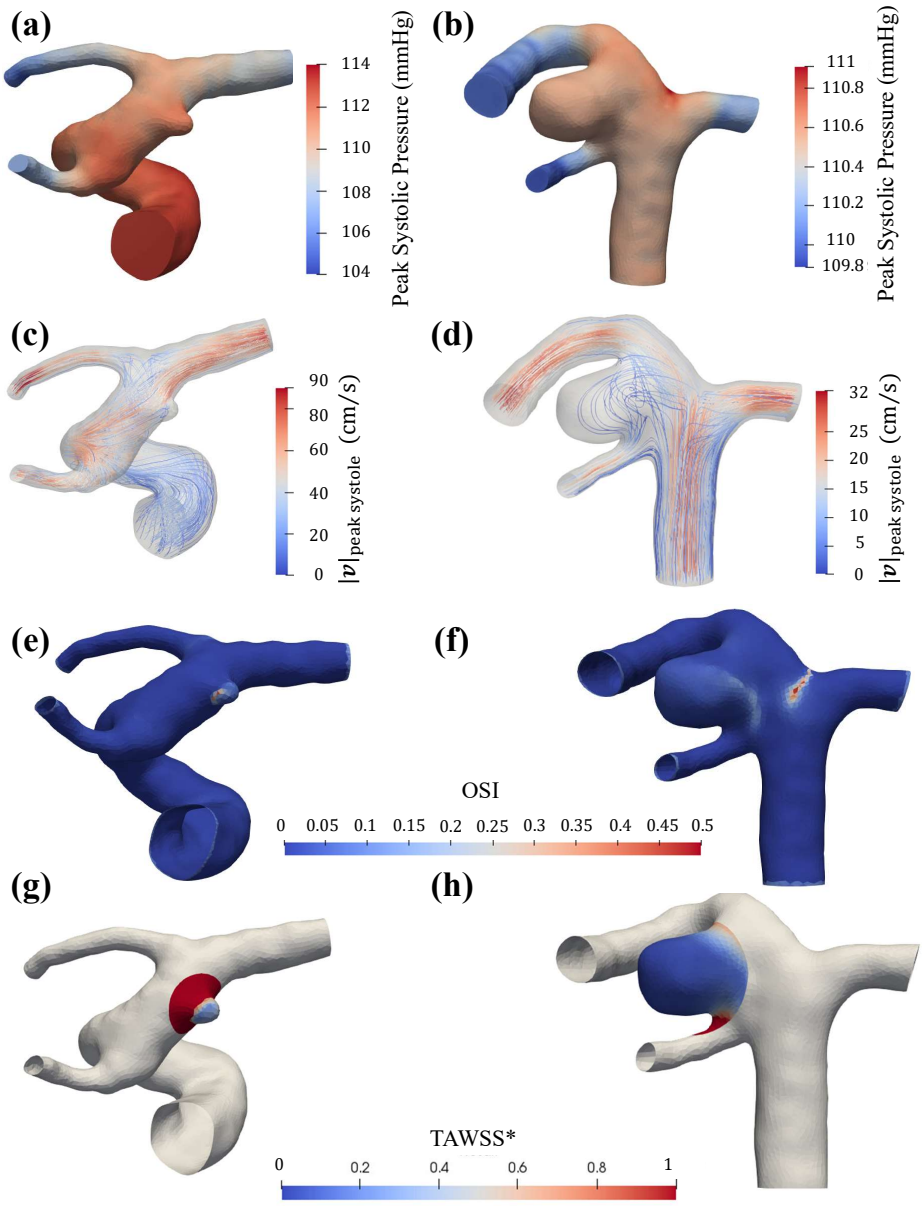

Figure 4.7. Hemodynamic metrics for subject S2. Each row shows a single metric: i.e. contours for pressure at peak systole, flow streamlines at peak systole, contours of oscillatory shear index (OSI) and normalized time-averaged wall shear stress magnitude. OSI was calculated using Equation (4.9). The time-averaged wall shear stress magnitude was normalized by the magnitude of spatiotemporal average of the wall shear stress over the feeding/parent vessel in each aneurysm, as per Equation (4.10). Panels (a), (c) (e) and (g) correspond to aneurysm S2A1, while panels (b), (d), (f) and (h) correspond to aneurysm S2A2. Abbreviations used – $|\mathbf{v}|$: Velocity magnitude, OSI: Oscillatory Shear Index. Note that the ranges of velocity and pressure values change across panels (a)-(d), as made clear by the individual color bars in each panel, TAWSS*: Normalized time-averaged wall shear stress magnitude.

and growing aneurysms demonstrated regions of high OSI (≈ 0.5). However, no association between high OSI and aneurysm's growth was found. Furthermore, there appeared to be no significant pattern of specific regions exposed to high OSI in the aneurysm geometries being considered.

Next, in panels (g) and (h) of Figures 4.6 and 4.7, the contours of magnitude of normalized time-averaged wall shear stress, TAWSS*, for both subjects are shown. The normalized time-averaged wall shear stress magnitude is defined as

$$\text{TAWSS}^*(\mathbf{x}) = \frac{\tilde{\tau}(\mathbf{x})}{\tilde{\tau}_{\text{parent}}}, \tag{4.10}$$

where $\tilde{\tau}(\mathbf{x})$ is the time-averaged wall shear stress magnitude at a location $\mathbf{x}$ on the aneurysm, and $\tilde{\tau}_{parent}$ is the wall shear stress on the parent/feeding artery averaged over its surface as well as over a single cardiac cycle. In previous studies, abnormally high and low wall shear stresses have been shown to illicit inflammatory responses resulting in aneurysm initiation and growth. As reported by Meng *et al.* [11], low wall shear stress is predominantly responsible for aneurysmal growth via matrix metalloprotease (MMP) induced degradation of the extracellular matrix (ECM). Consequently, the areas characterized by abnormally low time-averaged wall shear stress (TAWSS$^* < 0.1$) were compared between the stable and growing aneurysms [74].

Table 4.6 lists the percentage of area under low TAWSS* as compared to the total surface area of the aneurysm. It can be observed that abnormally low shear regions are present in both stable and growing aneurysms. However, within the same subject, the area under low TAWSS* is larger (almost by a factor of 2 in S1 and more in S2) in the growing aneurysm, as compared to the stable aneurysm. This observation, which is consistent with observations from previous studies [75], [76], suggests that the proportion of area under low wall shear (relative to the total aneurysmal surface area) contributes to aneurysm growth or stability, rather than the mere presence of an area exposed to low wall shear. Physiologically, aneurysm growth is driven by the imbalance between arterial wall repair and wall degradation caused by aberrant hemodynamics [11], [77]. Therefore, t is hypothesized that the larger proportion of area under low TAWSS* on the aneurysm lead to larger regions of the aneurysmal wall

being subjected to cell degradation and apoptosis, tipping the balance towards aneurysm growth.

Table 4.6. Reynolds number at peak systole and percentage of area under abnormal biomechanical loads for each aneurysm.

Aneurysm	Re	Area under low shear*	Area under low shear and low OStI*
S1A1	329	18.3	–
S1A2	250	34.9	23.3
S2A1	490	3.1	3.3
S2A2	292	58.8	32.8

*As a percentage of total surface area of the aneurysm.

Note that the inlet Reynolds numbers at peak systole given in Table 4.6 are calculated according to Equation (3.8).

4.4.2 Structural Metrics

One of the contributions of this FSI-simulation-based analysis was the ability to compute metrics within the arterial wall in addition to the hemodynamic parameters. Here, two such biomechanical metrics are considered: the wall deformation and the oscillatory stress index, referred to as OStI.

Previous work has shown the impact of arterial wall deformation on aneurysm progression and eventual rupture. Vanrosomme *et al.* [78] hypothesized that increased distensibility of aneurysms is associated with increased risk of rupture due to loss of mural cells. Other studies (e.g. Liu *et al.* [79] and the references therein) indicated that cyclic mechanical stretch leads to mural cell degradation, thus driving aneurysm growth. Therefore, the deformation patterns of stable and growing aneurysms were investigated. Panels (a) and (b) of Figures 4.8 and 4.9 show the deformation at peak systole for each aneurysm. The corresponding spatial distribution are shown in panel (f) of Figures 4.8 and 4.9, as a split violin plot.

For both subjects, the median peak deformation, was found to be approximately 1.5 times higher in the growing aneurysms as compared to the corresponding stable aneurysms. Furthermore, while the largest deformations on the stable and growing aneurysms were

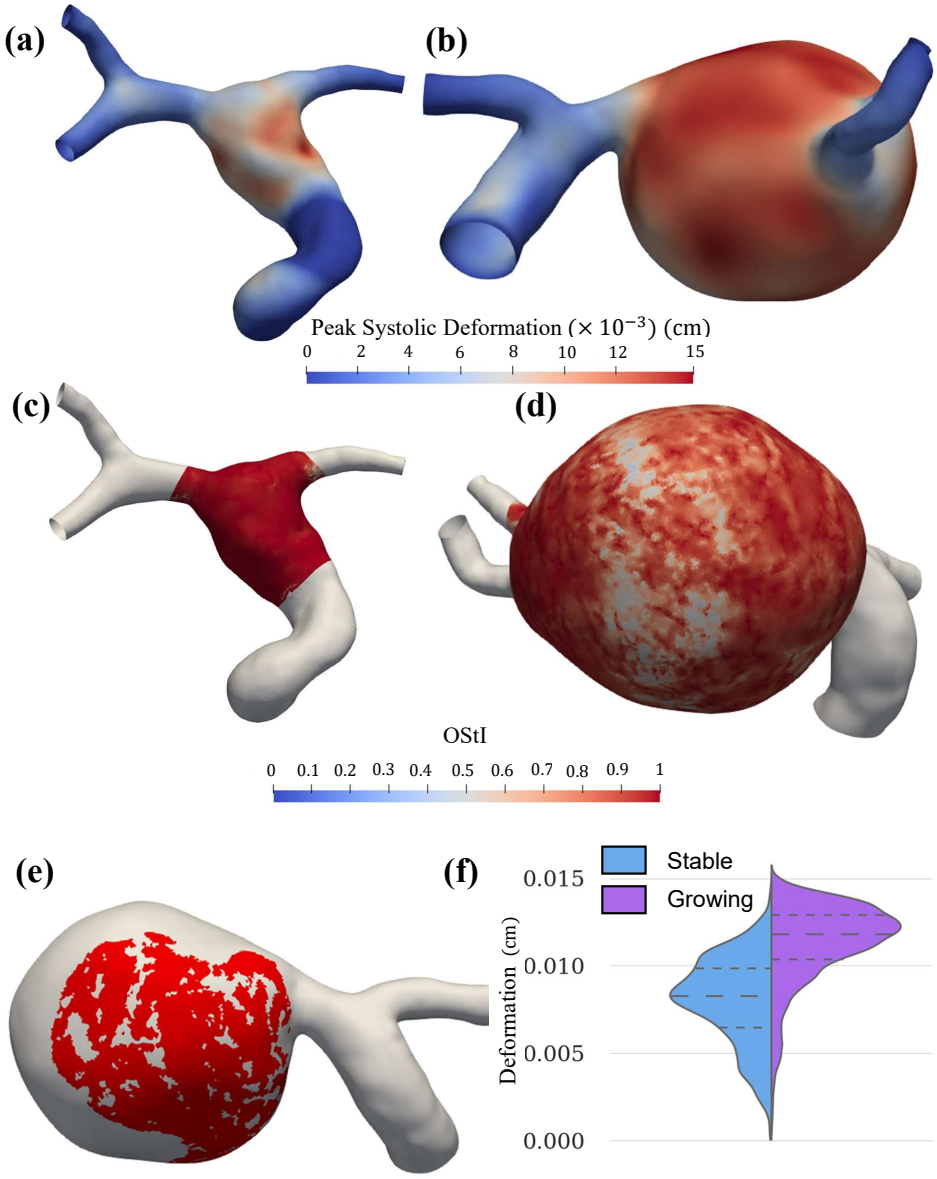

Figure 4.8. Biomechanical parameters for subject S1. (a) and (b) Deformation at peak systole for aneurysms S1A1 and S1A2, respectively. (c) and (d) Oscillatory stress index in aneurysms S1A1 and S1A2, respectively, calculated using Equations (4.11) and (4.12). (e) Region of overlapping low TAWSS* (< 0.1) and low OStI < 0.96) in the aneurysm S1A2. (f) Split violin plot of distribution of peak systolic deformations (see panels (a) and (b) in the same figure) over the aneurysmal surface. The data for S1A1 is shown in the left-hand side plot, whereas the data for subject S1A2 is shown in the right-hand side plot. Dashed lines (lowest to highest) show the 25-50-75% quartiles. Abbreviations used – TAWSS*: Time-averaged wall shear stress normalized by the parent/feeding vessel spatiotemporal wall shear stress average, OStI: Oscillatory Stress Index.

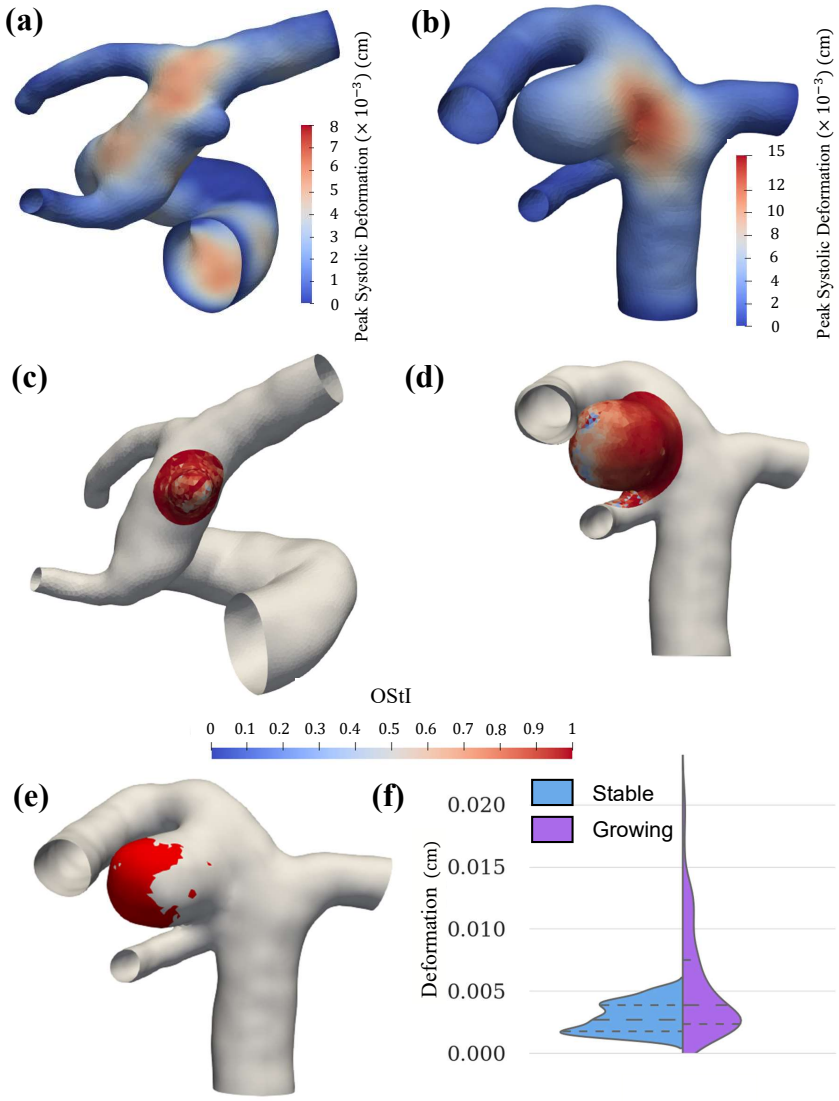

Figure 4.9. Biomechanical parameters for subject S2. (a) and (b) Deformation at peak systole for aneurysms S2A1 and S2A2, respectively. (c) and (d) Oscillatory stress index in aneurysms S2A1 and S2A2, respectively, calculated using Equations (4.11) and (4.12). (e) Region of overlapping low TAWSS* (< 0.1) and low OStI < 0.96) in the aneurysm S2A2. (f) Split violin plot of distribution of peak systolic deformations (see panels (a) and (b) in the same figure) over the aneurysmal surface. The data for S2A1 is shown in the left-hand side plot, whereas the data for subject S2A2 is shown in the right-hand side plot. Dashed lines (lowest to highest) show the 25-50-75% quartiles. Abbreviations used – TAWSS*: Time-averaged wall shear stress normalized by the parent/feeding vessel spatiotemporal wall shear stress average, OStI: Oscillatory Stress Index. Note that the ranges of velocity and pressure values change across panels (a) and (b), as made clear by the individual color bars in each panel.

not significantly different for S1, they differed by almost a factor of three for S2. These findings suggested that, as compared to the reference state at diastole, growing aneurysms underwent larger deformations within the cardiac cycle and were therefore more prone to mural cell degradation as compared to their stable counterparts.

The oscillatory stress index (OStI) at each location was defined as the time-averaged change in orientation of the maximum absolute principal stress over the cardiac cycle with respect to the orientation at diastole as reference. Mathematically, this definition can be expressed as

$$\mathrm{OStI}(\mathbf{x}) = \frac{1}{T}\int_0^T \cos(\theta(\mathbf{x},t))\,dt, \tag{4.11}$$

where T is the temporal period of the cardiac cycle, diastole is assumed to be at $t = 0$, and

$$\cos(\theta(\mathbf{x},t)) = \frac{|\mathbf{PD}(\mathbf{x},t)\cdot\mathbf{PD}(\mathbf{x},0)|}{|\mathbf{PD}(\mathbf{x},t)|\cdot|\mathbf{PD}(\mathbf{x},0)|} \tag{4.12}$$

is the angle between the orientation of the maximum absolute principal stress $\mathbf{PD}(\mathbf{x},t)$ at a given location $\mathbf{x}$ at time t and the orientation of the maximum absolute principal stress at diastole $\mathbf{PD}(\mathbf{x},0)$ (i.e. $\mathbf{PD}$ at the same location $\mathbf{x}$ and $t = 0$). The maximum absolute principal stress at any given location $\mathbf{x}$ and time point t is the largest absolute eigenvalue of the local stress tensor. Subsequently, the orientation of this maximum absolute principal stress is the orientation of the associated eigenvector.

Based on the definition of OStI, lower values indicate that the direction of the maximum absolute principal stress fluctuates through the cardiac cycle and higher values (close to one) indicate that the maximum absolute principal stress orientation remains unchanged. The methodology used to compute the principal stresses and the corresponding directions is similar to that used in [80]. The stress tensor on the outer surface of the arterial wall is expressed in terms of the local coordinate system comprised of two local orthogonal surface tangent vectors (given by $\mathbf{t}_1$ and $\mathbf{t}_2$) and the local normal $\mathbf{n}$. The corresponding rotation tensor $\mathbf{R}$ can be written as: $[\mathbf{t}_1\ \mathbf{t}_2\ \mathbf{n}]$. Subsequently, the traction condition on the outer wall is enforced strongly by modifying the last row and column of the rotated stress tensor. However, unlike the simulations in [80], for which a zero traction condition was imposed, a value of

$-k\boldsymbol{\delta}$ was prescribed, where k is the tissue support parameter and $\boldsymbol{\delta}$ is the deformation. In the local coordinates, the normal vector can simply be written as $\mathbf{n} = [0\ 0\ 1]^{\mathrm{T}}$. Therefore, imposing $\boldsymbol{\sigma} \cdot \mathbf{n} = -k\boldsymbol{\delta}$ is equivalent to setting the elements in the last row (and column) of the rotated stress tensor equal to $-k$ times the corresponding component of the deformation expressed in the local coordinate system. The deformation expressed in the local coordinate system, denoted $\tilde{\boldsymbol{\delta}}$, and the deformation in the global coordinate system, denoted $\boldsymbol{\delta}$, are related as $\tilde{\boldsymbol{\delta}} = \mathbf{R}^{\mathrm{T}}\boldsymbol{\delta}$.

Panels (c) and (d) of Figures 4.8 and 4.9 show the contour plots of OStI for the stable and growing aneurysms in both subjects. Collagen is the main constituent within the extra-cellular matrix (ECM) of the arterial wall that maintains structural integrity through dynamic cross-linking of fibres over the cardiac cycle in response to tensile stresses elicited by blood pressure [11], [81]. Consequently, collagen fibres in regions of low OStI values are exposed to oscillating tensile stresses requiring repeated realignment and re-orientation of fibres over the cardiac cycle [65]. It was hypothesized that this type of 'structural insult' was the principal driver of collagen remodeling. In combination with a compromised ECM due to MMP-induced degradation caused by low wall shear, the result was a degraded and remodeled collagen fiber network. This would reduce the capability of the arterial wall to sustain arterial stress under normal loading conditions, driving aneurysmal wall remodeling and growth.

Subsequently, regions of overlapping low wall shear stress (i.e. where $\mathrm{TAWSS}^{*} < 0.1$) and regions of low OStI (i.e. where $\mathrm{OStI} < 0.96$) were extracted and the proportion of these regions between the stable and growing aneurysms in the same subject was compared. The chosen threshold for OStI corresponded to $\cos(15°)$, which was the limit of the small angle approximation. The corresponding overlapping area (in red) is shown in panel (e) of Figures 4.8 and 4.9. It was observed that while such regions occupy a sizeable proportion in the growing aneurysms, they are almost either entirely absent or negligibly small ($< 5\%$) in stable aneurysms (see Table 4.6). This observation indicates that oscillatory arterial wall stresses, combined with regions of low wall shear stresses, may be potential biomarkers for aneurysm progression.

4.4.3 Limitations

The main limitations of the present analysis lie in the modeling assumptions made for the arterial wall and boundary conditions for the FSI simulations. Since the models were based on retrospective imaging data, obtaining subject-specific flow and pressure measurements for these aneurysms was not possible. Therefore, flow boundary conditions used in the analysis, i.e. the RCR outflow boundary conditions and inlet flow waveforms, were not subject specific. However, as explained in Section 4.4, the flow and structural metrics obtained from simulations correspond to physiologically realistic conditions in these subject. Therefore, the relative comparisons between stable and growing aneurysms in the same subject were meaningful.

The arterial wall thickness model, even though physiologically realistic, was also not subject-specific. This limitation arose due to lack of vessel wall information in standard-of-care imaging, including CTA, MRA and X-ray angiography data. Additionally, the assumption that the arterial wall could be modeled as an isotropic neo-Hookean material was a simplification of the physiological wall response. Moreover, the elasticity model used did not account for changes in material properties due to the aneurysmal disease.

Blood vessels in the brain are in contact with various tissues, which, in general, have a nonlinear and anisotropic spatiotemporal response. While the analysis accounted for heterogeneity in tissue support, depending on nature of contact, the svFSI platform currently lacks the capability to model nonlinear or time-dependent support behaviour due to the surrounding tissue. With regard to the spring-dashpot boundary condition used, the analysis neglected viscous damping due to presence of CSF (cerebrospinal fluid) in the subarachnoid spaces.

Lastly, in this study, only two subjects were considered, owing to the rarity of subjects with multiple, unruptured and untreated aneurysms who, in addition to possessing both growing and stable aneurysms, have undergone longitudinal imaging studies. Thus, the present analysis sets the groundwork for future studies on biomechanical risk factors in aneurysmal disease in order to help clinicians with the risk stratification of cerebral aneurysms.

5. SUMMARY

In this thesis, a computational analysis of cerebral aneurysms, accounting for blood flow-vessel wall interactions, was performed with a view towards understanding the impact of biomechanical parameters on aneurysm growth and eventual rupture. Specific aims were formulated towards this goal, the accomplishments of which, are summarized below.

5.1 Specific Aim 1

In Chapter 2, a novel methodology wass developed to obtain physiologically realistic computational FSI models of aneurysms from standard-of-care imaging data (i.e. data that is available most commonly in clinical settings). A workflow to estimate nonuniform vessel wall thickness, in particular the impact of hemodynamic forces on aneurysmal wall thickness was proposed. A unique meshing strategy to obtain conformal computational meshes for the fluid and solid domain (of non-uniform wall thickness), with mesh refinement close to the fluid-solid interface, was also devised. This advancement, in particular, is expected to overcome the limitations of the current meshing workflow within the SimVascular simulation environment and enhance fidelity of wall shear stress computations in future cardiovascular FSI analyses performed using the svFSI solver.

5.2 Specific Aim 2

In Chapter 3, leveraging 4DUS imaging data, a novel methodology was proposed to obtain animal-specific heterogeneous tissue support parameter values that can be used to model the effect of surrounding tissue on the outer vessel wall. An optimum range of the tissue support parameter spring stiffness, $k = 10^6 - 10^7$ dyne/cm^3, was determined for the FSI model. For both non-diseased and hypertensive expanded aortas, these values ensured that arterial wall deformations predicted by simulations were in good agreement with *in vivo* 4DUS measurements at peak systole. Accomplishing this specific aim yielded a methodology, as well as initial parameter estimates using idealized murine models, for incorporating heterogeneous

tissue support in FSI simulations of aneurysms biomechanics. This methodology improves the current state of the art for simulating physiologically realistic vessel wall deformation.

5.3 Specific Aim 3

In Chapter 4, coupled blood flow and vessel wall motion and deformation was modeled in two subjects with multiple cerebral aneurysms. Using standard-of-care patient imaging data, physiologically realistic computational models were developed, which accounted for both the nonuniform aneurysmal wall thickness and the effect of surrounding tissue support on the outer wall's motion and deformation. A scaling analysis was performed to determine the appropriate order-of-magnitude of tissue support parameters for the cerebral aneurysm models, based on estimates for diseased murine aortae from Chapter 2. Hemodynamic and structural metrics were computed and compared between stable and growing aneurysms in the same subject. Specifically, the time averaged wall shear stress, the oscillatory shear index, and peak systolic deformation were considered.

Additionally, a novel metric, the oscillatory stress index, indicative of the fluctuations in the orientation of the largest arterial principal stress, was defined and computed. Significant differences were observed between stable and growing aneurysms in the same subject in the area under low shear, peak systolic deformation, and the area under combined low shear and low oscillatory stress index. The proportion of aneurysmal area exposed to both low shear and oscillating arterial stresses was large ($\approx$ 23 to 33%) in the growing aneurysms, compared to the corresponding stable aneurysms, for which such areas were either nonexistent or less than 5% of the total area. Based on these results, it can be hypothesized that the presence of significant regions under this abnormal combined loading, which signifies a large degree of degradation and remodeling of collagen in the arterial wall, may be predictors of aneurysmal growth. The proposed computational framework, and the associated biomechanical factors, provide a proof-of-concept for a novel approach of quantitative assessment of risk of growth in aneurysms.

6. FUTURE WORK

In future studies, image-based computational models of cerebral aneurysm can be developed with a view toward augmenting clinical decision making. To this end, the computational methodology developed in Chapter 1, and consequently, the analyses in Chapters 2 and 3, can be extended to include subject/animal-specific flow and structural boundary conditions. On the one hand, advanced imaging modalities such as 4D flow MRI could be used to obtain noninvasive estimates of inflow waveforms, as well as subject/animal-specific flow splits between individual outlet vessels [82]. Outflow RCR parameters could also be tuned to match individual diastolic and pulse pressure values as opposed to population averaged values. This approach would ensure that biomechanical parameters obtained through these computational models are more individualistic.

On the other hand, subject-specific wall thickness distributions could be incorporated by utilizing data from advanced imaging modalities such as black-blood MRI or amplified MRI [83], [84]. Subject-specific wall thickness distributions will lead to a more accurate estimation of arterial stresses and deformations. While the nearly incompressible neo-Hookean model is a popular and computationally inexpensive model for the behaviour of the vessel wall, constitutive models of additional complexity (such as the Holzapfel-Gasser-Ogden (HGO) model [65]) could be used to account for the vessel wall's anisotropic and inhomogeneous composition. As seen from the comparisons in Section 3.4.3, however, there were no discernible differences in vessel wall deformation (between the neo-Hookean and HGO models) for the purposes of tuning tissue support parameters. However, the HGO model and its extensions would allow for incorporating the effect of different families of collagen fibers. Furthermore, with availability of relevant histological data, the analysis presented herein could be extended along those lines, potentially improving estimation of the stress distribution within the arterial wall.

In the analysis presented in Chapter 2, the effect of incorporating some heterogeneity in tissue support parameters was demonstrated, and an optimum range of tissue support parameters was found. However, accounting for further heterogeneity in these values, in

particular, the various types of contacts, as well as spatiotemporal nonlinearity, would further improve the fidelity of computational models.

Assessment of statistical significance/power of reported biomarkers is needed for translation of this approach into the clinical setting. Such assessments will not only require a larger cohort of subjects/animals, but also further testing the efficacy of the proposed methodology to estimate tissue support parameters for murine models of thoracic aortic aneurysms and eventually human cerebral aneurysm sujects (Chapters 3 and 4) .

Lastly, the present work could be extended to analyze cerebral aneurysms with daughter sacs or blebs. Presence of blebs or daughter sacs on intracranial aneurysms is a risk factor for aneurysm rupture. Even though bleb formation is associated with focal weakening of the wall, the exact effect of blebs on aneurysm rupture is not well understood [85]. Most previous studies of bleb aneurysms accounting for FSI have assumed uniform material properties over the aneurysm and the bleb region [6], [8], [29]. However, as reported in [86], blebs can be atherosclerotic or thin walled, possessing material properties distinct from their parent aneurysm. The methodology developed in Chapter 2 can easily be extended to incorporate distinct material properties of the bleb. Therefore, future work could be done to investigate the consequences of nonuniformity in wall thickness and material properties on enhanced rupture risk of these bleb aneurysms.

REFERENCES

[1] G. J. E. Rinkel, M. Djibuti, A. Algra, and J. van Gijn, "Prevalence and Risk of Rupture of Intracranial Aneurysms," *Stroke*, vol. 29, no. 1, pp. 251–256, 1998, DOI: 10.1161/01.STR.29.1.251.

[2] W. I. Schievink, "Intracranial Aneurysms," *New England Journal of Medicine*, vol. 336, no. 1, pp. 28–40, 1997, DOI: 10.1056/NEJM199701023360106.

[3] A. Updegrove, N. M. Wilson, J. Merkow, H. Lan, A. L. Marsden, and S. C. Shadden, "SimVascular: An Open Source Pipeline for Cardiovascular Simulation," eng, *Annals of Biomedical Engineering*, vol. 45, no. 3, pp. 525–541, 2017, DOI: 10.1007/s10439-016-1762-8.

[4] H. Lan, A. Updegrove, N. M. Wilson, G. D. Maher, S. C. Shadden, and A. L. Marsden, "A Re-Engineered Software Interface and Workflow for the Open-Source SimVascular Cardiovascular Modeling Package," *Journal of Biomechanical Engineering*, vol. 140, no. 2, p. 24 501, 2018, DOI: 10.1115/1.4038751.

[5] P. A. Yushkevich, J. Piven, H. C. Hazlett, R. G. Smith, S. Ho, J. C. Gee, and G. Gerig, "User-guided 3D active contour segmentation of anatomical structures: Significantly improved efficiency and reliability," *NeuroImage*, vol. 31, no. 3, pp. 1116–1128, 2006, DOI: 10.1016/j.neuroimage.2006.01.015.

[6] C. J. Lee, Y. Zhang, H. Takao, Y. Murayama, and Y. Qian, "A fluid-structure interaction study using patient-specific ruptured and unruptured aneurysm: The effect of aneurysm morphology, hypertension and elasticity," *Journal of Biomechanics*, vol. 46, no. 14, pp. 2402–2410, 2013, DOI: 10.1016/j.jbiomech.2013.07.016.

[7] J. R. Cebral, M. Vazquez, D. M. Sforza, G. Houzeaux, S. Tateshima, E. Scrivano, C. Bleise, P. Lylyk, and C. M. Putman, "Analysis of hemodynamics and wall mechanics at sites of cerebral aneurysm rupture," *Journal of NeuroInterventional Surgery*, vol. 7, no. 7, pp. 530–536, 2015, DOI: 10.1136/neurintsurg-2014-011247.

[8] S. Voß, S. Glaßer, T. Hoffmann, O. Beuing, S. Weigand, K. Jachau, B. Preim, D. Thévenin, G. Janiga, and P. Berg, "Fluid-Structure Simulations of a Ruptured Intracranial Aneurysm: Constant versus Patient-Specific Wall Thickness," *Computational and Mathematical Methods in Medicine*, vol. 2016, 2016, DOI: 10.1155/2016/9854539.

[9] Y. Bazilevs, K. Takizawa, and T. E. Tezduyar, *Computational Fluid-Structure Interaction*. Chichester, UK: John Wiley & Sons, Ltd, 2013, pp. 95–154, DOI: 10.1002/9781118483565.

[10] R. Blankena, R. Kleinloog, B. H. Verweij, P. van Ooij, B. ten Haken, P. R. Luijten, G. J. E. Rinkel, and J. J. M. Zwanenburg, "Thinner Regions of Intracranial Aneurysm Wall Correlate with Regions of Higher Wall Shear Stress: A 7T MRI Study," *American Journal of Neuroradiology*, vol. 37, no. 7, pp. 1310–1317, 2016, DOI: 10.3174/ajnr.A4734.

[11] H. Meng, V. M. Tutino, J. Xiang, and A. Siddiqui, "High WSS or low WSS? Complex interactions of hemodynamics with intracranial aneurysm initiation, growth, and rupture: toward a unifying hypothesis.," *AJNR. American journal of neuroradiology*, vol. 35, no. 7, pp. 1254–62, 2014, DOI: 10.3174/ajnr.A3558.

[12] U. Ayachit, *ParaView Guide, A Parallel Visualization Application*. 2007, p. 366.

[13] P. Cignoni, M. Callieri, M. Corsini, M. Dellepiane, F. Ganovelli, and G. Ranzuglia, "MeshLab: an Open-Source Mesh Processing Tool," in *Eurographics Italian Chapter Conference*, V. Scarano, R. D. Chiara, and U. Erra, Eds., The Eurographics Association, 2008, DOI: 10.2312/LocalChapterEvents/ItalChap/ItalianChapConf2008/129-136.

[14] C. Zhu, V. Vedula, D. Parker, N. Wilson, S. Shadden, and A. Marsden, "svFSI: A Multiphysics Package for Integrated Cardiac Modeling," *Journal of Open Source Software*, vol. submitted, 2022, [Online]. Available: https://github.com/SimVascular/svFSI/blob/9a3ff6fb2747d208f536ea9598dce327a8f28535/paper.pdf.

[15] Y. Bazilevs, V. M. Calo, T. J. Hughes, and Y. Zhang, "Isogeometric fluid-structure interaction: Theory, algorithms, and computations," *Computational Mechanics*, vol. 43, no. 1, pp. 3–37, 2008, DOI: 10.1007/s00466-008-0315-x.

[16] M. Esmaily-Moghadam, Y. Bazilevs, and A. L. Marsden, "A new preconditioning technique for implicitly coupled multidomain simulations with applications to hemodynamics," *Computational Mechanics*, vol. 52, no. 5, pp. 1141–1152, 2013, DOI: 10.1007/s00466-013-0868-1.

[17] C. A. Taylor, T. J. R. Hughes, and C. K. Zarins, "Finite element modeling of blood flow in arteries," *Computer Methods in Applied Mechanics and Engineering*, vol. 158, no. 1-2, pp. 155–196, 1998, DOI: 10.1016/S0045-7825(98)80008-X.

[18] J. C. Simo and T. J. R. Hughes, "Computational inelasticity," *Computers & Mathematics with Applications*, vol. 37, no. 6, p. 134, 1999, DOI: 10.1016/S0898-1221(99)90277-8.

[19] R. Torii, M. Oshima, T. Kobayashi, K. Takagi, and T. E. Tezduyar, "Fluid-structure interaction modeling of blood flow and cerebral aneurysm: Significance of artery and aneurysm shapes," *Computer Methods in Applied Mechanics and Engineering*, vol. 198, no. 45-46, pp. 3613–3621, 2009, DOI: 10.1016/j.cma.2008.08.020.

[20] A. A. Johnson and T. E. Tezduyar, "Mesh update strategies in parallel finite element computations of flow problems with moving boundaries and interfaces," *Computer Methods in Applied Mechanics and Engineering*, vol. 119, no. 1-2, pp. 73–94, 1994, DOI: 10.1016/0045-7825(94)00077-8.

[21] I. Babuška, "The finite element method with Lagrangian multipliers," *Numerische Mathematik*, vol. 20, no. 3, pp. 179–192, 1973, DOI: 10.1007/BF01436561.

[22] Y. Bazilevs, V. M. Calo, J. A. Cottrell, T. J. R. Hughes, A. Reali, and G. Scovazzi, "Variational multiscale residual-based turbulence modeling for large eddy simulation of incompressible flows," *Computer Methods in Applied Mechanics and Engineering*, vol. 197, no. 1-4, pp. 173–201, 2007, DOI: 10.1016/j.cma.2007.07.016.

[23] A. Masud and R. Calderer, "A variational multiscale stabilized formulation for the incompressible Navier–Stokes equations," *Computational Mechanics*, vol. 44, no. 2, pp. 145–160, 2009, DOI: 10.1007/s00466-008-0362-3.

[24] J. Chung and G. M. Hulbert, "A Time Integration Algorithm for Structural Dynamics With Improved Numerical Dissipation: The Generalized-α Method," *Journal of Applied Mechanics*, vol. 60, no. 2, pp. 371–375, 1993, DOI: 10.1115/1.2900803.

[25] J. S. Tran, *svFSI Equation Formulation Documentation*.

[26] M. Esmaily Moghadam, I. E. Vignon-Clementel, R. Figliola, and A. L. Marsden, "A modular numerical method for implicit 0D/3D coupling in cardiovascular finite element simulations," *Journal of Computational Physics*, vol. 244, pp. 63–79, 2013, DOI: 10.1016/j.jcp.2012.07.035.

[27] P. Moireau, N. Xiao, M. Astorino, C. A. Figueroa, D. Chapelle, C. A. Taylor, and J.-F. Gerbeau, "External tissue support and fluid–structure simulation in blood flows," *Biomechanics and Modeling in Mechanobiology*, vol. 11, no. 1-2, pp. 1–18, 2012, DOI: 10.1007/s10237-011-0289-z.

[28] K. Bäumler, V. Vedula, A. M. Sailer, J. Seo, P. Chiu, G. Mistelbauer, F. P. Chan, M. P. Fischbein, A. L. Marsden, and D. Fleischmann, "Fluid–structure interaction simulations of patient-specific aortic dissection," *Biomechanics and Modeling in Mechanobiology*, no. 0123456789, 2020, DOI: 10.1007/s10237-020-01294-8.

[29] Y. Bazilevs, M.-C. Hsu, Y. Zhang, W. Wang, T. Kvamsdal, S. Hentschel, and J. G. Isaksen, "Computational vascular fluid–structure interaction: methodology and application to cerebral aneurysms," *Biomechanics and Modeling in Mechanobiology*, vol. 9, no. 4, pp. 481–498, 2010, DOI: 10.1007/s10237-010-0189-7.

[30] T. E. Tezduyar, K. Takizawa, T. Brummer, and P. R. Chen, "Space-time fluid-structure interaction modeling of patient-specific cerebral aneurysms," *International Journal for Numerical Methods in Biomedical Engineering*, vol. 27, no. 11, pp. 1665–1710, 2011, DOI: 10.1002/cnm.1433.

[31] T. E. Tezduyar, S. Sathe, M. Schwaab, and B. S. Conklin, "Arterial fluid mechanics modeling with the stabilized space – time fluid – structure interaction technique," *International Journal for Numerical Methods in Fluids*, pp. 601–629, 2008, DOI: 10.1002/fld.1633.

[32] K. Takizawa and T. E. Tezduyar, "Fluid–Structure Interaction Modeling of Patient-Specific Cerebral Aneurysms," in *Visualization and Simulation of Complex Flows in Biomedical Engineering*, ser. Lecture Notes in Computational Vision and Biomechanics, vol. 12, Dordrecht: Springer Science+Business Media, 2014, pp. 25–45, DOI: 10.1007/978-94-007-7769-9_2.

[33] K. Takizawa, C. Moorman, S. Wright, J. Purdue, T. McPhail, P. R. Chen, J. Warren, and T. E. Tezduyar, "Patient-specific arterial fluid-structure interaction modeling of cerebral aneurysms," *International Journal for Numerical Methods in Fluids*, vol. 65, no. 1-3, pp. 308–323, 2011, DOI: 10.1002/fld.2360.

[34] M.-C. Hsu and Y. Bazilevs, "Blood vessel tissue prestress modeling for vascular fluid–structure interaction simulation," *Finite Elements in Analysis and Design*, vol. 47, no. 6, pp. 593–599, 2011, DOI: 10.1016/j.finel.2010.12.015.

[35] K. A. S. Boster, T. C. Shidhore, A. A. Cohen-Gadol, I. C. Christov, and V. L. Rayz, "Challenges in Modeling Hemodynamics in Cerebral Aneurysms Related to Arteriovenous Malformations," *Cardiovascular Engineering and Technology*, 2022, DOI: 10.1007/s13239-022-00609-3.

[36] H. Si, "TetGen, a Delaunay-Based Quality Tetrahedral Mesh Generator," *ACM Transactions on Mathematical Software*, vol. 41, no. 2, pp. 1–36, 2015, DOI: 10.1145/2629697.

[37] *FEconv Finite Element mesh Converter*, [Online]. Available: https://github.com/victorsndvg/FEconv.

[38] G. Van Rossum and F. L. Drake Jr, *Python reference manual*. Centrum voor Wiskunde en Informatica Amsterdam, 1995.

[39] C. A. Figueroa, C. A. Taylor, A. J. Chiou, V. Yeh, and C. K. Zarins, "Magnitude and Direction of Pulsatile Displacement Forces Acting on Thoracic Aortic Endografts," *Journal of Endovascular Therapy*, vol. 16, no. 3, pp. 350–358, 2009, DOI: 10.1583/09-2738.1.

[40] J. H. Bracamonte, J. S. Wilson, and J. S. Soares, "Assessing Patient-Specific Mechanical Properties of Aortic Wall and Peri-Aortic Structures From In Vivo DENSE Magnetic Resonance Imaging Using an Inverse Finite Element Method and Elastic Foundation Boundary Conditions," *Journal of Biomechanical Engineering*, vol. 142, no. 12, p. 121 011, 2020, DOI: 10.1115/1.4047721.

[41] K. Takizawa, Y. Bazilevs, T. E. Tezduyar, C. C. Long, A. L. Marsden, and K. Schjodt, "ST and ALE-VMS methods for patient-specific cardiovascular fluid mechanics modeling," *Mathematical Models and Methods in Applied Sciences*, vol. 24, no. 12, pp. 2437–2486, 2014, DOI: 10.1142/S0218202514500250.

[42] N. Freidoonimehr, R. Chin, A. Zander, and M. Arjomandi, "A Review on the Effect of Temporal Geometric Variations of the Coronary Arteries on the Wall Shear Stress and Pressure Drop," *Journal of Biomechanical Engineering*, vol. 144, no. 1, p. 010 801, 2022, DOI: 10.1115/1.4051923.

[43] J. A. Elefteriades, A. Sang, G. Kuzmik, and M. Hornick, "Guilt by association: paradigm for detecting a silent killer (thoracic aortic aneurysm)," *Open Heart*, vol. 2, no. 1, e000169, 2015, DOI: 10.1136/openhrt-2014-000169.

[44] R. Campobasso, F. Condemi, M. Viallon, P. Croisille, S. Campisi, and S. Avril, "Evaluation of Peak Wall Stress in an Ascending Thoracic Aortic Aneurysm Using FSI Simulations: Effects of Aortic Stiffness and Peripheral Resistance," *Cardiovascular Engineering and Technology*, vol. 9, no. 4, pp. 707–722, 2018, DOI: 10.1007/s13239-018-00385-z.

[45] R. Pons, A. Guala, J. F. Rodríguez-Palomares, J. C. Cajas, L. Dux-Santoy, G. Teixidó-Tura, J. J. Molins, M. Vázquez, A. Evangelista, and J. Martorell, "Fluid–structure interaction simulations outperform computational fluid dynamics in the description of thoracic aorta haemodynamics and in the differentiation of progressive dilation in Marfan syndrome patients," *Royal Society Open Science*, vol. 7, no. 2, p. 191 752, 2020, DOI: 10.1098/rsos.191752.

[46] A. M. Booher and K. A. Eagle, "Diagnosis and management issues in thoracic aortic aneurysm," *American Heart Journal*, vol. 162, no. 1, 38–46.e1, 2011, DOI: 10.1016/j.ahj.2011.04.010.

[47] Z. Wang, N. Flores, M. Lum, A. D. Wisneski, Y. Xuan, J. Inman, M. D. Hope, D. A. Saloner, J. M. Guccione, L. Ge, and E. E. Tseng, "Wall stress analyses in patients with 5 cm versus <5 cm ascending thoracic aortic aneurysm," *The Journal of Thoracic and Cardiovascular Surgery*, vol. 162, no. 5, pp. 1452–1459, 2021, DOI: 10.1016/j.jtcvs.2020.02.046.

[48] H. L. Cebull, V. L. Rayz, and C. J. Goergen, "Recent Advances in Biomechanical Characterization of Thoracic Aortic Aneurysms," *Frontiers in Cardiovascular Medicine*, vol. 7, p. 75, 2020, DOI: 10.3389/fcvm.2020.00075.

[49] A. Karimi and D. M. Milewicz, "Structure of the Elastin-Contractile Units in the Thoracic Aorta and How Genes That Cause Thoracic Aortic Aneurysms and Dissections Disrupt This Structure," *Canadian Journal of Cardiology*, vol. 32, no. 1, pp. 26–34, 2016, DOI: 10.1016/j.cjca.2015.11.004.

[50] C. E. Korenczuk, R. Y. Dhume, K. K. Liao, and V. H. Barocas, "Ex Vivo Mechanical Tests and Multiscale Computational Modeling Highlight the Importance of Intramural Shear Stress in Ascending Thoracic Aortic Aneurysms," *Journal of Biomechanical Engineering*, vol. 141, no. 12, p. 121 010, 2019, DOI: 10.1115/1.4045270.

[51] P. Reymond, P. Crosetto, S. Deparis, A. Quarteroni, and N. Stergiopulos, "Physiological simulation of blood flow in the aorta: Comparison of hemodynamic indices as predicted by 3-D FSI, 3-D rigid wall and 1-D models," *Medical Engineering & Physics*, vol. 35, no. 6, pp. 784–791, 2013, DOI: 10.1016/j.medengphy.2012.08.009.

[52] M. Markl, M. T. Draney, M. D. Hope, J. M. Levin, F. P. Chan, M. T. Alley, N. J. Pelc, and R. J. Herfkens, "Time-Resolved 3-Dimensional Velocity Mapping in the Thoracic Aorta," *Journal of Computer Assisted Tomography*, vol. 28, no. 4, pp. 459–468, 2004, DOI: 10.1097/00004728-200407000-00005.

[53] A. Daugherty, D. L. Rateri, I. F. Charo, A. P. Owens, D. A. Howatt, and L. A. Cassis, "Angiotensin II infusion promotes ascending aortic aneurysms: Attenuation by CCR2 deficiency in apoE-/- mice," *Clinical Science*, vol. 118, no. 11, pp. 681–689, 2010, DOI: 10.1042/CS20090372.

[54] A. Daugherty, M. W. Manning, and L. A. Cassis, "Angiotensin II promotes atherosclerotic lesions and aneurysms in apolipoprotein E–deficient mice," *Journal of Clinical Investigation*, vol. 105, no. 11, pp. 1605–1612, 2000, DOI: 10.1172/JCI7818.

[55] A. Acuna, A. G. Berman, F. W. Damen, B. A. Meyers, A. R. Adelsperger, K. C. Bayer, M. C. Brindise, B. Bungart, A. M. Kiel, R. A. Morrison, J. C. Muskat, K. M. Wasilczuk, Y. Wen, J. Zhang, P. Zito, and C. J. Goergen, "Computational Fluid Dynamics of Vascular Disease in Animal Models," *Journal of Biomechanical Engineering*, vol. 140, no. 8, p. 080 801, 2018, DOI: 10.1115/1.4039678.

[56] A. R. Adelsperger, E. H. Phillips, H. S. Ibriga, B. A. Craig, L. A. Green, M. P. Murphy, and C. J. Goergen, "Development and growth trends in angiotensin II-induced murine dissecting abdominal aortic aneurysms," *Physiological Reports*, vol. 6, no. 8, e13668, 2018, DOI: 10.14814/phy2.13668.

[57] E. H. Phillips, P. Di Achille, M. R. Bersi, J. D. Humphrey, and C. J. Goergen, "Multi-Modality Imaging Enables Detailed Hemodynamic Simulations in Dissecting Aneurysms in Mice," *IEEE Transactions on Medical Imaging*, vol. 36, no. 6, pp. 1297–1305, 2017, DOI: 10.1109/TMI.2017.2664799.

[58] F. W. Damen, A. G. Berman, A. H. Soepriatna, J. M. Ellis, S. D. Buttars, K. L. Aasa, and C. J. Goergen, "High-Frequency 4-Dimensional Ultrasound (4DUS): A Reliable Method for Assessing Murine Cardiac Function," *Tomography*, vol. 3, no. 4, pp. 180–187, 2017, DOI: 10.18383/j.tom.2017.00016.

[59] Y. Bazilevs, M.-C. Hsu, D. J. Benson, S. Sankaran, and A. L. Marsden, "Computational fluid–structure interaction: methods and application to a total cavopulmonary connection," *Computational Mechanics*, vol. 45, no. 1, pp. 77–89, 2009, DOI: 10.1007/s00466-009-0419-y.

[60] E. Soudah, E. Y. K. Ng, T. H. Loong, M. Bordone, U. Pua, and S. Narayanan, "CFD modelling of abdominal aortic aneurysm on hemodynamic loads using a realistic geometry with CT," *Computational and Mathematical Methods in Medicine*, vol. 2013, pp. 1–9, 2013, DOI: 10.1155/2013/472564.

[61] C. Bellini, M. R. Bersi, A. W. Caulk, J. Ferruzzi, D. M. Milewicz, F. Ramirez, D. B. Rifkin, G. Tellides, H. Yanagisawa, and J. D. Humphrey, "Comparison of 10 murine models reveals a distinct biomechanical phenotype in thoracic aortic aneurysms," *Journal of the Royal Society Interface*, vol. 14, no. 130, 2017, DOI: 10.1098/rsif.2016.1036.

[62] I. E. Vignon-Clementel, C. A. Figueroa, K. E. Jansen, and C. A. Taylor, "Outflow boundary conditions for 3D simulations of non-periodic blood flow and pressure fields in deformable arteries," *Computer Methods in Biomechanics and Biomedical Engineering*, vol. 13, no. 5, pp. 625–640, 2010, DOI: 10.1080/10255840903413565, arXiv: 1012.0736.

[63] N. Xiao, J. Alastruey, and C. Alberto Figueroa, "A systematic comparison between 1-D and 3-D hemodynamics in compliant arterial models," *International Journal for Numerical Methods in Biomedical Engineering*, vol. 30, no. 2, pp. 204–231, 2014, DOI: 10.1002/cnm.2598.

[64] M. S. Olufsen, "Structured tree outflow condition for blood flow in larger systemic arteries," *American Journal of Physiology - Heart and Circulatory Physiology*, vol. 276, no. 1, H257–H268, 1999, DOI: 10.1152/ajpheart.1999.276.1.h257.

[65] I. Hariton, G. DeBotton, T. C. Gasser, and G. A. Holzapfel, "Stress-driven collagen fiber remodeling in arterial walls," *Biomechanics and Modeling in Mechanobiology*, vol. 6, no. 3, pp. 163–175, 2007, DOI: 10.1007/s10237-006-0049-7.

[66] N. Petterson, M. Sjoerdsma, M. van Sambeek, F. van de Vosse, and R. Lopata, "Mechanical characterization of abdominal aortas using multi-perspective ultrasound imaging," *Journal of the Mechanical Behavior of Biomedical Materials*, vol. 119, p. 104 509, 2021, DOI: 10.1016/j.jmbbm.2021.104509.

[67] E. Durbak, S. Tarraf, C. Gillespie, E. Germano, F. Cikach, E. Blackstone, K. Emerton, R. Colbrunn, C. Bellini, and E. E. Roselli, "Ex-vivo Biaxial Load Testing Analysis of Aortic Biomechanics Demonstrates Variation in Elastic Energy Distribution Across the Aortic Zone Zero," *The Journal of Thoracic and Cardiovascular Surgery*, 2021, DOI: 10.1016/j.jtcvs.2021.09.071.

[68] R. Valente, A. Mourato, M. Brito, J. Xavier, A. Tomás, and S. Avril, "Fluid–Structure Interaction Modeling of Ascending Thoracic Aortic Aneurysms in SimVascular," *Biomechanics*, vol. 2, no. 2, pp. 189–204, 2022, DOI: 10.3390/biomechanics2020016.

[69] K. Takizawa, T. Brummer, T. E. Tezduyar, and P. R. Chen, "A comparative study based on patient-specific fluid-structure interaction modeling of cerebral aneurysms," *Journal of Applied Mechanics*, vol. 79, no. 1, p. 010 908, 2012, DOI: 10.1115/1.4005071.

[70] R. Torii, M. Oshima, T. Kobayashi, K. Takagi, and T. E. Tezduyar, "Numerical investigation of the effect of hypertensive blood pressure on cerebral aneurysm—Dependence of the effect on the aneurysm shape," *International Journal for Numerical Methods in Fluids*, vol. 54, no. 6-8, pp. 995–1009, 2007, DOI: 10.1002/fld.1497.

[71] M. E. Macdonald and R. Frayne, "Phase contrast MR imaging measurements of blood flow in healthy human cerebral vessel segments," *Physiological Measurement*, vol. 36, no. 7, pp. 1517–1527, 2015, DOI: 10.1088/0967-3334/36/7/1517.

[72] V. Anand and I. C. Christov, "On the Deformation of a Hyperelastic Tube Due to Steady Viscous Flow Within," in *Dynamical Processes in Generalized Continua and Structures*, ser. Springer Series on Advanced Structured Materials, H. Altenbach, A. Belyaev, V. A. Eremeyev, A. Krivtsov, and A. V. Porubov, Eds., vol. 103, Cham, Switzerland: Springer Nature, 2019, ch. 2, pp. 17–35, DOI: 10.1007/978-3-030-11665-1_2.

[73] J. Xiang, V. M. Tutino, K. V. Snyder, and H. Meng, "CFD: Computational fluid dynamics or confounding factor dissemination? the role of hemodynamics in intracranial aneurysm rupture risk assessment," *American Journal of Neuroradiology*, vol. 35, no. 10, pp. 1849–1857, 2014, DOI: 10.3174/ajnr.A3710.

[74] J. L. Thenier-Villa, A. Riveiro Rodríguez, R. M. Martínez-Rolán, M. Gelabert-González, P. M. González-Vargas, R. A. Galarraga Campoverde, J. Díaz Molina, A. De La Lama Zaragoza, P. Martínez-Cueto, J. Pou, and C. Conde Alonso, "Hemodynamic Changes in the Treatment of Multiple Intracranial Aneurysms: A Computational Fluid Dynamics Study," *World Neurosurgery*, vol. 118, e631–e638, 2018, DOI: 10.1016/j.wneu.2018.07.009.

[75] L. Boussel, V. Rayz, C. McCulloch, A. Martin, G. Acevedo-Bolton, M. Lawton, R. Higashida, W. S. Smith, W. L. Young, and D. Saloner, "Aneurysm growth occurs at region of low wall shear stress: Patient-specific correlation of hemodynamics and growth in a longitudinal study," *Stroke*, vol. 39, no. 11, pp. 2997–3002, 2008, DOI: 10.1161/STROKEAHA.108.521617.

[76] M. Shojima, "Magnitude and Role of Wall Shear Stress on Cerebral Aneurysm: Computational Fluid Dynamic Study of 20 Middle Cerebral Artery Aneurysms," *Stroke*, vol. 35, pp. 2500–2505, 2004, DOI: 10.1161/01.STR.0000144648.89172.0f.

[77] J. Frösen, J. Cebral, A. M. Robertson, and T. Aoki, "Flow-induced, inflammation-mediated arterial wall remodeling in the formation and progression of intracranial aneurysms," *Neurosurgical Focus*, vol. 47, no. 1, E21, 2019, DOI: 10.3171/2019.5.focus19234.

[78] A. Vanrossomme, O. Eker, J.-P. Thiran, G. Courbebaisse, and K. Zouaoui Boudjeltia, "Intracranial Aneurysms: Wall Motion Analysis for Prediction of Rupture," *American Journal of Neuroradiology*, vol. 36, no. 10, pp. 1796–1802, 2015, DOI: 10.3174/ajnr.A4310.

[79] P. Liu, Y. Song, Y. Zhou, Y. Liu, T. Qiu, Q. An, J. Song, P. Li, Y. Shi, S. Li, K. Quan, G.-Y. Yang, and W. Zhu, "Cyclic Mechanical Stretch Induced Smooth Muscle Cell Changes in Cerebral Aneurysm Progress by Reducing Collagen Type IV and Collagen Type VI Levels," *Cellular Physiology and Biochemistry*, vol. 45, no. 3, pp. 1051–1060, 2018, DOI: 10.1159/000487347.

[80] Y. Bazilevs, M.-C. Hsu, Y. Zhang, W. Wang, X. Liang, T. Kvamsdal, R. Brekken, and J. G. Isaksen, "A fully-coupled fluid-structure interaction simulation of cerebral aneurysms," *Computational Mechanics*, vol. 46, no. 1, pp. 3–16, 2010, DOI: 10.1007/s00466-009-0421-4.

[81] G. Holzapfel, "Collagen in Arterial Walls: Biomechanical Aspects," in *Collagen: Structure and Mechanics*, P. Fratzl, Ed., Boston, MA: Springer, 2016, pp. 285–324, DOI: 10.1007/978-0-387-73906-9_11.

[82] R. Pewowaruk and A. Roldán-Alzate, "4D Flow MRI Estimation of Boundary Conditions for Patient Specific Cardiovascular Simulation," *Annals of Biomedical Engineering*, vol. 47, no. 8, pp. 1786–1798, 2019, DOI: 10.1007/s10439-019-02285-2.

[83] M. Henningsson, S. Malik, R. Botnar, D. Castellanos, T. Hussain, and T. Leiner, "Black-Blood Contrast in Cardiovascular MRI," *Journal of Magnetic Resonance Imaging*, vol. 55, no. 1, pp. 61–80, 2022, DOI: 10.1002/jmri.27399.

[84] I. Terem, W. W. Ni, M. Goubran, M. S. Rahimi, G. Zaharchuk, K. W. Yeom, M. E. Moseley, M. Kurt, and S. J. Holdsworth, "Revealing sub-voxel motions of brain tissue using phase-based amplified MRI (aMRI)," *Magnetic Resonance in Medicine*, vol. 80, no. 6, pp. 2549–2559, 2018, DOI: 10.1002/mrm.27236.

[85] S. F. Salimi Ashkezari, F. J. Detmer, F. Mut, B. J. Chung, A. K. Yu, C. J. Stapleton, A. P. See, S. Amin-Hanjani, F. T. Charbel, B. Rezai Jahromi, M. Niemelä, J. Frösen, J. Zhou, S. Maiti, A. M. Robertson, and J. R. Cebral, "Blebs in intracranial aneurysms: prevalence and general characteristics," *Journal of NeuroInterventional Surgery*, pp. 2020–16 274, 2020, DOI: 10.1136/neurintsurg-2020-016274.

[86] S. F. Salimi Ashkezari, F. Mut, B. J. Chung, A. K. Yu, C. J. Stapleton, A. P. See, S. Amin-Hanjani, F. T. Charbel, B. Rezai Jahromi, M. Niemelä, J. Frösen, S. Maiti, A. M. Robertson, and J. R. Cebral, "Hemodynamics in aneurysm blebs with different wall characteristics," *Journal of NeuroInterventional Surgery*, pp. 1–5, 2020, DOI: 10.1136/neurintsurg-2020-016601.

A. MATLAB Script Used to Compute Stress for the HGO Model

The following script was used to compute the Cauchy stress tensor under the HGO constitutive model (recall Equation (3.11)) for biaxial loading.

```
% Author: Tyler C. Diorio
% Modified by: Tanmay C. Shidhore
% Last Update: 04/12/2022

% Deformation Gradient
%syms F [3,3]
syms f [3,1]
F = sym(diag(f))
I = sym(eye(3));
% Deformation Gradient, transposed
F_T=transpose(F);

%Jacobian of the Deformation Gradient
J=det(F);
% Right and left Cauchy Green Deformation Tensors
C=F_T*F;
b = F*F_T;

% Green-Lagrange Strain tensor
E = (1/2)*(C-I)
%Invariants of the Right-Cauchy Green Deformation Tensor
I_1_C=trace(C);
I_2_C=0.5*(trace(C)^2-trace((C)^2));
I_3_C=det(C);

%ISOCHORIC (DEVIATORY) QUANTITIES [_bar]:
% Unimodular (distortional) part of the Deformation Gradient
F_bar=(J^(-1/3))*F;
% Unimodular (distortional) part of the Deformation Gradient, transposed
F_bar_T=transpose(F_bar);
% Isochoric Right and left Cauchy Green Deformation Tensors
```

```
C_bar=F_bar_T*F_bar
b_bar = F_bar*F_bar_T;
%Invariants of the isochoric Right-Cauchy Green Deformation Tensor
I_bar_1_C_bar=trace(C_bar);
I_bar_2_C_bar=0.5*(trace(C_bar)^2-trace((C_bar)^2));
I_bar_3_C_bar=det(C_bar);
%% Constitutive Laws:

% Modeling the Holzapfel-Gasser-Ogden model, as in
% doi:10.1023/A:1010835316564
% The only difference is that the constants k_1 and k_2 are assumed to be
% different for each of the invariants in the anisotropic contribution.
% The overall model also contains a volumetric component, which, for an
% incompressible material, reduces to a term pI. This can be added at a
% later stage.

% Material parameters
syms a b c p
% Fiber orientations
a01 = [0 0 1];
a02 = [0 0 -1];
% Define tensor A_i, i=1,2 as the dyadic of a0i with itself
A1 = a01*transpose(a01);
A2 = a02*transpose(a02);

% Evaluating the invariants I_4 and I_6. Note that the double contraction
% A:B is nothing but trace(A*B)

I4 = trace(C_bar*A1);
I6 = trace(C_bar*A2);

% Compute volumetric part of strain energy density function
W_vol = (c/2)*(I_bar_1_C_bar - 3);

%kappa.value = 0;
%if kappa.value==0
```

```
    % Compute anisotropic contributions from I4 and I6
W_aniso_4 = (a/(2*b))*(exp(b*(I4-1)^2) - 1);
W_aniso_6 = (a/(2*b))*(exp(b*(I6-1)^2) - 1);
%elseif kappa.value==1/3
%    W_aniso_4 = (a4/(2*b4))*(exp(b4*((I_bar_1_C_bar/3)-1)^2) - 1);
%    W_aniso_6 = (a6/(2*b6))*(exp(b6*((I_bar_1_C_bar/3)-1)^2) - 1);
%else
%    disp('You have not entered a valid kappa value (0 or 1/3).')
%end

% Total W
W = W_vol + W_aniso_4 + W_aniso_6
%% Stress Computations


% PK1 stress
P1_1 = diff(W,f1);
%P1_2 = diff(W,F1_2);
%P1_3 = diff(W,F1_3);
%P2_1 = diff(W,F2_1);
P2_2 = diff(W,f2);
%P2_3 = diff(W,F2_3);
%P3_1 = diff(W,F3_1);
%P3_2 = diff(W,F3_2);
P3_3 = diff(W,f3);
%P = [P1_1 P1_2 P1_3; P2_1 P2_2 P2_3; P3_1 P3_2 P3_3];
P = diag([P1_1 P2_2 P3_3])
% Cauchy Stress
sigma = p*I + (1/J)*P*F_T
sigma_simp1 = subs(sigma,f1,1/(f2*f3))
```

B. Python Code for Extracting Faces

The python code below is used to extract boundary faces from the combined surface `.vtp` mesh file. The code assumes that the `.vtp` file is named as '`mesh-complete.exterior.vtp`' and that a folder of the name 'mesh-surfaces' exists in the same directory as the python script file. The code can be executed within the Python programming environment within SimVascular with the command given below:

```
$ <path_to_SimVascular_executable> --python -- <python_code_name>
```

```
import os
from shutil import copyfile
import sv
#import sv_vis as vis
import sys
import vtk

solid_name = 'outer_shell'
solid_file_name = 'mesh-complete.exterior.vtp'
mesh_dir = './mesh-surfaces/'


# Set the solid modeling kernel.
modeler = sv.modeling.Modeler(sv.modeling.Kernel.POLYDATA)

# Read the closed surface representing a solid model.
#solid = sv.Solid.pySolidModel()
solid = modeler.read(solid_file_name)

# Extract faces.
solid.compute_boundary_faces(45.0)
solid_face_ids = [int(id) for id in solid.get_face_ids()]
print ("Face IDs: " + str(solid_face_ids))
#print (solid_face_ids[0])

for face_id in solid_face_ids:
```

```
    solid_face_name =  mesh_dir + solid_name + "_mesh_face_" + str(face_id
    )
    face = solid.get_face_polydata(int(face_id))
    #face.write(solid_face_name)
    #solid_face_pd = sv.Repository.ExportToVtk(solid_face_name)
    #print("  Face {0:d}  num nodes: {1:d}".format(int(face_id)))
    solid_face_file_name = solid_face_name + ".vtp"
    writer = vtk.vtkXMLPolyDataWriter()
    writer.SetFileName(solid_face_file_name)
    writer.SetInputData(face)
    writer.Update()
    writer.Write()
```

VITA

Education

Purdue University, West Lafayette, IN

Doctor of Philosophy, Mechanical Engineering *Aug 2022*

Master of Science, Mechanical Engineering *May 2018*

Birla Institute of Technology and Science, Pilani, India

M.Sc. (Physics) & B.E. (Mechanical Engineering) Integrated Dual Degree *Jul 2015*

Work Experience

Technology Intern, Halliburton Energy Services Inc., Carrollton, TX *May-Aug 2019*

Teaching Experience

Graduate Teaching Assistant, Purdue University, West Lafayette, IN *Aug 2018-Dec 2021*

Publications resulting from this thesis

- T. C. Shidhore[†], H. L. Cebull[†], M. C. Madden, I. C. Christov, V. L. Rayz and C. J. Goergen, "Estimating external tissue support parameters with fluid-structure interaction models from 4D ultrasound of murine thoracic aortae," *Engineering with Computers*, 2022 (under review). ([†]These authors contributed equally)

- T. C. Shidhore, A. A. Cohen-Gadol, I. C. Christov and V. L. Rayz, "Comparative Assessment of Biomechanical Parameters in Subjects with Multiple Cerebral Aneurysms using Fluid-Structure Interaction Simulations," *Journal of Biomechanical Engineering*, 2022 (under review).

- K. A. S. Boster, T. C. Shidhore, A. A. Cohen-Gadol, I. C. Christov and V. L. Rayz, "Challenges in Modeling Hemodynamics in Cerebral Aneurysms Related to Arteriovenous Malformations", *Cardiovascular Engineering and Technology*, 2022, doi:10.1007/s13239-022-00609.

Conference presentations resulting from this thesis

- T. C. Shidhore*, V. L. Rayz, A. A. Cohen-Gadol and I. C. Christov, "Fluid-Structure Interaction (FSI) Modeling of Hemodynamics and Biomechanics in Patients with Multiple Cerebral Aneurysms", 74^{th} Annual Meeting of the APS Division of Fluid Dynamics, Phoenix, Arizona. (*Presenter)

- T. C. Shidhore, A. A. Cohen-Gadol V. L. Rayz and I. C. Christov*, "Patient-Specific Modeling of Flow and Fluid-Structure Interaction in a Cohort of Patients with Multiple Cerebral Aneurysms", 2021 Brain Aneurysm Foundation Research Symposium, Scottsdale, Arizona. (*Presenter)